

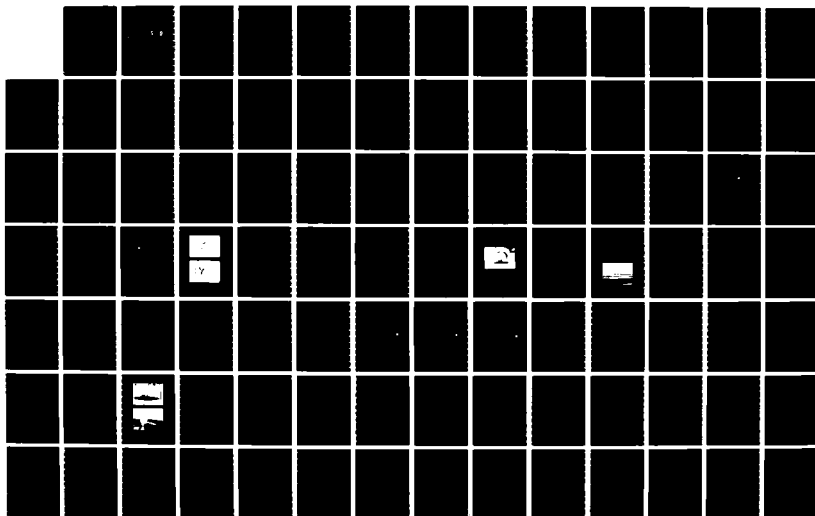
NO-A178 258

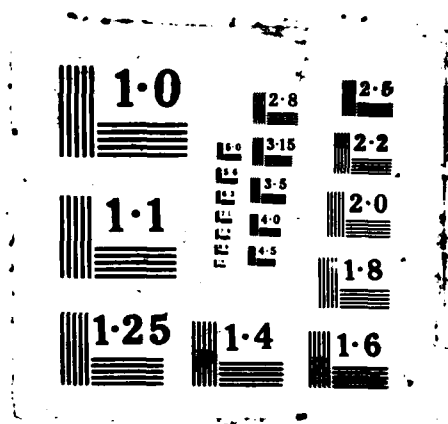
MAGNETOSTATIC SURFACE FIELD MEASUREMENT FACILITY(U) 1/2  
MICHIGAN UNIV ANN ARBOR RADIATION LAB V V LIEPA ET AL.  
DEC 86 AFML-TN-86-29 F29681-82-K-0024

UNCLASSIFIED

F/B 14/2

NL





AD-A178 258

**MAGNETOSTATIC SURFACE FIELD MEASUREMENT  
FACILITY**

V. V. Liepa  
D. L. Sengupta  
T. B. A. Senior

The University of Michigan  
Ann Arbor, Michigan 48109

December 1986

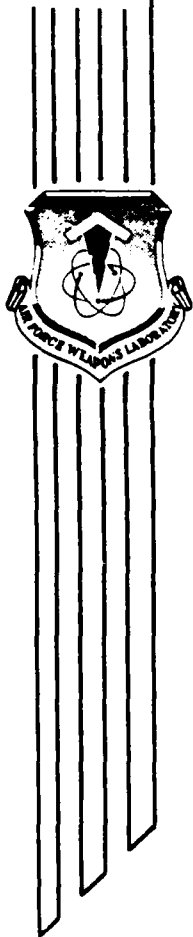
Final Report

DTIC  
ELECTE  
MAR 19 1987  
S D

Approved for public release; distribution unlimited.

AIR FORCE WEAPONS LABORATORY  
Air Force Systems Command  
Kirtland Air Force Base, NM 87117-6008

DTIC FILE COPY



UNCLASSIFIED

SECURITY CLASSIFICATION OF THIS PAGE

## REPORT DOCUMENTATION PAGE

1a. REPORT SECURITY CLASSIFICATION Unclassified		1b. RESTRICTIVE MARKINGS AM 8258	
2a. SECURITY CLASSIFICATION AUTHORITY		3. DISTRIBUTION/AVAILABILITY OF REPORT Approved for public release; distribution unlimited.	
2b. DECLASSIFICATION/DOWNGRADING SCHEDULE		4. PERFORMING ORGANIZATION REPORT NUMBER(S) AFWL-TN-86-29	
5. MONITORING ORGANIZATION REPORT NUMBER(S)		6a. NAME OF PERFORMING ORGANIZATION University of Michigan	
6b. OFFICE SYMBOL (If applicable)		7a. NAME OF MONITORING ORGANIZATION Air Force Weapons Laboratory	
6c. ADDRESS (City, State and ZIP Code) Radiation Laboratory Ann Arbor, MI 48109		7b. ADDRESS (City, State and ZIP Code) Kirtland AFB, New Mexico 87117-6008	
8a. NAME OF FUNDING/SPONSORING ORGANIZATION		8b. OFFICE SYMBOL (If applicable)	
8c. ADDRESS (City, State and ZIP Code)		9. PROCUREMENT INSTRUMENT IDENTIFICATION NUMBER F29601-82-K-0024	
10. SOURCE OF FUNDING NOS.		11. TITLE (Include Security Classification) MAGNETOSTATIC SURFACE FIELD MEASUREMENT FACILITY	
PROGRAM ELEMENT NO. 64711F		PROJECT NO. 3763	
TASK NO. 01		WORK UNIT NO. 31	
12. PERSONAL AUTHOR(S) Liepa, V. V.; Sengupta, D. L.; Senior, T. B. A.		13a. TYPE OF REPORT Final	
13b. TIME COVERED FROM Oct 82 TO Jun 84		14. DATE OF REPORT (Yr., Mo., Day) 1986 December	
15. PAGE COUNT 134		16. SUPPLEMENTARY NOTATION	
17. COSATI CODES		18. SUBJECT TERMS (Continue on reverse if necessary and identify by block number)	
FIELD GROUP SUB. GR.		Magnetic Fields	
14 02		Aircraft	
20 03		Electromagnetic Fields	
		Magnetostatic	
		Electromagnetic Coupling	
19. ABSTRACT (Continue on reverse if necessary and identify by block number) This report presents the analysis, design, and performance characteristics of an RF Helmholtz coil facility. The facility was developed to measure the magnetic response of models up to two feet in size. Test measurements were made on metallic spheres and cylinders, and on a model F-106 aircraft over a 1-25 MHz frequency range corresponding to 20-520 kHz full scale. A large portion of the report is devoted to the relevant theoretical studies that include studies of the magnetostatic response of canonical shapes, both perfectly and imperfectly conducting.			
20. DISTRIBUTION/AVAILABILITY OF ABSTRACT UNCLASSIFIED/UNLIMITED <input checked="" type="checkbox"/> SAME AS RPT. <input type="checkbox"/> DTIC USERS <input type="checkbox"/>		21. ABSTRACT SECURITY CLASSIFICATION Unclassified	
22a. NAME OF RESPONSIBLE INDIVIDUAL William D. Prather		22b. TELEPHONE NUMBER (Include Area Code) (505) 844-3206	
		22c. OFFICE SYMBOL NTAAT	

UNCLASSIFIED

SECURITY CLASSIFICATION OF THIS PAGE

UNCLASSIFIED

SECURITY CLASSIFICATION OF THIS PAGE

## PREFACE

The authors wish to thank the many people who contributed to this program. Messrs. Joe Ferris and Jim Morgan constructed the Aluminum Facility. The students who participated were Peter Bower, who constructed the Plywood Facility, and Bruce Dykaar, who analyzed and tested the coil and driver circuits. Jonathan Go (with other help) performed the field measurements and processed the data for facility evaluations and Tim Peters made the measurements on the F-106 model aircraft.

Special appreciation goes to Dr. Carl Baum of AFWL, who provided many of the ideas that went into the design of the facility. Thanks also go to Wanita Rasey, Dorothea Merrill, and Jan Fisk for typing the report.



Accession For	
NTIS CRA&I	<input checked="" type="checkbox"/>
DTIC TAB	<input type="checkbox"/>
Unannounced	<input type="checkbox"/>
Justification	
By	
Distribution /	
Availability Codes	
Dist	Avail and/or Special
A-1	

## TABLE OF CONTENTS

	<u>Page</u>
1. INTRODUCTION	9
2. THEORETICAL CONSIDERATIONS	11
2.1 Analysis of Fields Produced by dc Excited Helmholtz Coils	11
2.1.1 Introduction	11
2.1.2 Field Produced by a Circular Current	11
2.1.3 Helmholtz Coils	14
2.1.3.1 Fields of the Axis ( $v = 0$ ) of Two Coils	14
2.1.3.2 Fields in the Central Region ( $r \rightarrow 0$ )	16
2.1.3.3 Exact Expressions for the Fields	18
2.1.4 Numerical Computations	19
2.2 Analysis of Field Produced by ac Excited Helmholtz Coils	20
2.3 Other Considerations	27
2.3.1 Quasi-Magnetostatic Behavior	27
2.3.2 Effect of Penetration Depth	33
2.3.3 Excitation	34
3. PHYSICAL DESIGNS	35
3.1 Plywood Facility	36
3.1.1 The Structure	36

	<u>Page</u>
3.1.2 Current Drivers	38
3.1.3 Distribution Transformer	40
3.1.4 Tuning of the Facility	45
3.2 Aluminum Facility	45
4. TESTS AND EVALUATIONS OF FACILITIES	51
4.1 Plywood Facility Field Plots	53
4.2 Aluminum Facility Field Plots	57
4.3 Comparison of the Two Facilities	63
5. SAMPLE MEASUREMENTS	67
5.1 Spheres and Cylinders	67
5.2 Measurements on NASA F-106B Model	68
6. CONCLUSIONS	79
7. REFERENCES	81
APPENDIX A - ADDITIONAL DETAILS FOR SECTION 2.1	83
A.1 Derivation of Eqs. (2.9) and (2.10)	83
A.2 Derivation of Eq. (2.9)	84
A.3 Derivation of Eq. (2.10)	84
A.4 Computer Program	87
APPENDIX B - MAGNETOSTATIC FIELD NEAR A CONDUCTING BODY	89
B.1 Sphere	89
B.2 Prolate Spheroid	91
B.3 Numerical Results	96
B.4 References	103
APPENDIX C - LOW FREQUENCY SURFACE FIELD BEHAVIOR	105
C.1 Acoustically Hard Sphere	106



	<u>Page</u>
C.2 Acoustically Hard Prolate	108
C.3 Perfectly Conducting Sphere	110
C.4 Some Implications	113
C.5 References	115
APPENDIX D	117
D.1 Theoretical Analyses	117
D.2 Results	122
D.3 Listing of the Program	124
APPENDIX E - INDUCTANCE OF A LOOP	129

## LIST OF ILLUSTRATIONS

<u>Figure</u>		<u>Page</u>
3.1	Helmholtz coil geometry with support structure	37
3.2	Excitation diagram for the Plywood Facility	39
3.3	Aluminum housing for the current drivers	41
3.4	Current driver for the Helmholtz coils	42
3.5	Distribution transformer housing for the Plywood Facility	43
3.6	Aluminum Facility shown with a 2:1 prolate spheroid mounted for measurement	47
3.7	Dimensions of the Aluminum Facility	48
3.8	Implementation of the feed gaps	49
4.1	Experimental set-up to measure fields for Plywood and Aluminum Facilities	52
4.2	Horizontal plane results at $z=0, \pm 4$ inches (Plywood Facility)	54
4.3	Horizontal plane results at $z=\pm 6$ inches (Plywood Facility)	55
4.4	Vertical plane results at $\theta=0$ and $\theta=90$ degrees (Plywood Facility)	56
4.5	Horizontal plane results at $z=0, \pm 4$ inches (Aluminum Facility)	58
4.6	Horizontal plane results at $z=\pm 7$ inches (Aluminum Facility)	59
4.7	Vertical plane results at $\theta=90$ degrees, $f=7.875$ MHz (Aluminum Facility)	60
4.8	Vertical plane results at $\theta=90$ degrees, $f=10.0$ MHz (Aluminum Facility)	61
4.9	Vertical plane results at $\theta=90$ degrees, $f=15.0$ MHz (Aluminum Facility)	62

# ILLUSTRATIONS (cont.)

<u>Figure</u>		<u>Page</u>
4.10	Comparison of frequency response of the two facilities	64
5.1	Measured currents on 12 inch long cylinders	69
5.2	F-106 model set up for measurement	71
5.3	Axial surface field on F-106, top incidence, E-parallel to fuselage, STA: F481R	73
5.4	Figure 5.3 expanded to show magnetostatic data	74
5.5	Axial surface field on F-106, top incidence, E-perpendicular to fuselage, STA: WL104B	75
5.6	Figure 5.5 expanded to show magnetostatic data	76
5.7	Circumferential current on F-106, top incidence, E-perpendicular to the fuselage, STA: F481L	77
5.8	Figure 5.7 expanded to show magnetostatic data	78
B.1	$\Gamma_{\text{nor}}$ (---) and percent reduction in $\Gamma_{\text{tan}}$ (—) for a sphere away from the surface	97
B.2	$\Gamma_{\text{tan}}$ on the surface of a prolate spheroid as a function of $x/w$	99
B.3	$\Gamma_{\text{nor}}$ (---) and percent reduction in $\Gamma_{\text{tan}}$ (—) for a 2:1 prolate spheroid as functions of distance away from the surface	101
B.4	$\Gamma_{\text{nor}}$ (---) and percent reduction in $\Gamma_{\text{tan}}$ (—) for a 5:1 prolate spheroid as functions of distance away from the surface	102
D.1	Helmholtz coil and driver equivalent circuit	118
D.2	Secondary distribution circuit (source left)	120
D.3	Secondary distribution circuit (source right)	120
D.4	Resultant circuit	120
D.5	Computed coil current for a 14-foot cable length	125
D.6	Measured coil current for an 18-foot long cable	126
D.7	Measured coil current for an 14.3-foot long cable	127
E.1	Loop geometry	129
E.2	Equivalent circuits	130

## LIST OF TABLES

<u>Table</u>	<u>Page</u>
2.1 Numerical Values for Normalized Field Components	19
3.1 Drive Signal Voltages	44
E.1 Measured Loop Parameters	130

## 1. INTRODUCTION

The present University of Michigan surface field measurement facility [1] covers the frequency range from 100 MHz to 4770 MHz, corresponding to a wavelength of 3 m at the lowest frequency and 6.4 cm at the highest frequency. However, at frequencies below 120 MHz the performance of the chamber and its associated equipment deteriorates rapidly. For accurate measurements it is necessary that the sensor be small compared with the relevant dimensions of the target, and since there is a minimum size of sensor that can be constructed and that has sufficient sensitivity, there is in turn a minimum size target that can be used. In practice, therefore, the target must have overall dimensions greater than (about) 25 cm, implying a resonant wavelength of 0.5 m ( $f = 600$  MHz). The net result is that the present facility enables us to measure down to, at best, a frequency of  $0.2 f_0$ , where  $f_0$  is the lowest resonant frequency of the target. This is not quite low enough to define the low frequency behavior of the target. It is believed that a frequency of  $0.1 f_0$  or, preferably,  $0.05 f_0$  must be attained to specify the low frequency asymptote, and since it is inconceivable that any simple modification of the present facility would enable us to get down to 30 MHz, the construction of a separate facility for measuring the surface fields at one (or more) frequencies  $f \leq 0.05 f_0$  was undertaken.

The main purpose of the new facility is to extend the presently measured curves of surface magnetic field (or current) down to frequencies of 30 MHz or below by specifying the low frequency asymptote in each case. A measurement at a single frequency would suffice and, in

principle at least, the lower the frequency the better. Since the magnetic field is of interest, it is natural to consider a quasi-magnetostatic facility consisting, for example, of a pair of Helmholtz coils, and it is desirable that the facility be able to use models similar (or, indeed, identical) to the ones employed in the present facility.

Theoretical analyses of the fields produced by dc and rf excited Helmholtz coi's are presented in Section 2, and other pertinent studies such as the effect of a non-perfectly conducting or non-magnetic test body are also addressed here. Section 3 describes the design and implementation of the two facilities that were evaluated--one of plywood construction and the other all metal. Field maps and the frequency response, are presented in Section 4 and compared with the design criteria. Section 5 gives sample measurements for a sphere, cylinders and an F-106B model aircraft.

## 2. THEORETICAL CONSIDERATIONS

### 2.1 Analysis of Fields Produced by dc Excited Helmholtz Coils

2.1.1 Introduction. The Helmholtz coil arrangement consists of two circular coaxial coils, each of the same mean radius  $a$ , spaced apart (between the midplanes) by the distance  $a$ , and with conductor (or wire) diameter kept to a suitably small fraction of  $a$  [2]. When the coils are excited by direct currents in additive series, i.e., when each coil carries a similarly-oriented steady current  $I$ , a near-uniform axially directed magnetic field is produced in the central section of the axis of the system [3]. In this Section we develop the exact expressions for the various components of the field produced by the dc-excited Helmholtz coils, and derive some approximate expressions to examine the uniformity of the fields in the central region of the system.

2.1.2 Field Produced by a Circular Current. Let us consider a circular loop of radius  $a$  carrying a steady current  $I$  with the plane of the loop oriented in the  $x$ - $y$  plane such that its center coincides with the origin of a cylindrical coordinate system  $(r, \phi, z)$ . Since the exact expressions for the field components produced by such a system are well-known, we shall simply quote the relevant expressions (see [4,5] for the detailed derivations).

The magnetic vector potential at a field point  $P(r,z)$  is entirely  $\phi$ -directed and is given by

$$A_{\phi} = \frac{\mu I a}{2\pi} \int_0^{\pi} \frac{\cos \alpha \, d\alpha}{(a^2 + r^2 + z^2 - 2ar \cos \alpha)^{1/2}} \quad (2.1)$$

where  $\mu$  is the permeability of the medium and the other quantities are as defined earlier. Equation (2.1) can be expressed in terms of known integrals as

$$A_{\phi} = \frac{\mu I}{\pi \kappa} \left( \frac{a}{r} \right)^{1/2} \left[ \left( 1 - \frac{1}{2} \kappa^2 \right) K - E \right] \quad (2.2)$$

where

$$\kappa^2 = \frac{4ar}{[(a+r)^2 + z^2]} \quad (2.3)$$

and  $K$  and  $E$  are complete elliptic integrals of the first and second kinds, defined as [6]:

$$K = \int_0^{\pi/2} \frac{d\theta}{(1 - \kappa^2 \sin^2 \theta)^{1/2}} \quad (2.4)$$

$$E = \int_0^{\pi/2} (1 - \kappa^2 \sin^2 \theta)^{1/2} d\theta \quad (2.5)$$

Assuming  $\mu$  to be constant, the two field components can now be obtained from

$$\begin{aligned} H_r &= -\frac{1}{\mu} \frac{\partial A_{\phi}}{\partial z} \\ H_z &= \frac{1}{\mu r} \frac{\partial}{\partial r} (r A_{\phi}) \end{aligned} \quad (2.6)$$



Using (2.2) through (2.6) the following two exact expressions are obtained for the field components [3,4]:

$$H_r = \frac{I}{2\pi} \frac{z}{r[(a+r)^2 + z^2]^{1/2}} \left[ -K + \frac{a^2 + r^2 + z^2}{(a-r)^2 + z^2} E \right] \quad (2.7)$$

$$H_z = \frac{I}{2\pi} \frac{1}{[(a+r)^2 + z^2]^{1/2}} \left[ K + \frac{a^2 - r^2 - z^2}{(a-r)^2 + z^2} E \right]. \quad (2.8)$$

It can be shown (see Appendix A) that near the axis (i.e., as  $r \rightarrow 0$ ) the fields may be approximated as

$$H_r = \frac{3Ia^2}{4} \frac{zr}{[(a+r)^2 + z^2]^{5/2}} + O(r^2) \quad (2.9)$$

$$H_z = \frac{Ia^2}{2} \frac{1}{(a^2 + z^2)^{3/2}} \left[ 1 + \frac{3}{4} \frac{a^2 - 4z^2}{(a^2 + z^2)} r^2 + O(r^3) \right]. \quad (2.10)$$

From (2.9) and (2.10) it is found that the fields on the axis ( $r = 0$ ) are

$$\begin{aligned} H_r &\equiv 0, \\ H_z &= \frac{Ia^2}{2} \frac{1}{(a^2 + z^2)^{3/2}} = \frac{Ia^2}{2} f(z) \end{aligned} \quad (2.11)$$

and as shown in Appendix A, these are exact. The first three derivatives with respect to  $z$  of the function  $f(z)$  defined in (2.11) are

$$\begin{aligned} f'(z) &= - \frac{3z}{(a^2 + z^2)^{5/2}} \\ f''(z) &= - \frac{3(a^2 - 4z^2)}{(a^2 + z^2)^{7/2}} \end{aligned} \quad (2.12)$$

$$f'''(z) = - \frac{5z(3a^2 - 4z^2)}{(a^2 + z^2)^{9/2}}$$

Using (2.11) and (2.12) it is seen that with two similar coils located at  $z = \pm a/2$  the first three derivatives of the total field ( $H_z$  in this case) on the axis vanish at  $z = 0$ . This is the basis for the design of Helmholtz coils discussed in the next section.

### 2.1.3 Helmholtz Coils.

2.1.3.1 Fields on the Axis ( $r = 0$ ) of Two Coils. For generality we consider two circular coils, located at  $z = \pm h$  (referred to as coils 1 and 2, respectively), each of radius  $a$  and carrying a steady current  $I$ . Using (2.11) it can be shown that the exact field for  $r = 0$  produced by the system are

$$H_r \equiv 0 \quad (2.13)$$

$$H_z = \frac{Ia^2}{2} \left[ \frac{1}{[a^2 + (z-h)^2]^{3/2}} + \frac{1}{[a^2 + (z+h)^2]^{3/2}} \right]$$

Differentiating  $H_z$  with respect to  $z$ , the first four derivatives at  $z = 0$  are found to be

$$\frac{\partial H_z}{\partial z} = 0$$

$$\frac{\partial^2 H_z}{\partial z^2} = -3Ia^2 \frac{a^2 - 4h^2}{(a^2 + h^2)^{7/2}} \quad (2.14)$$

$$\frac{\partial^3 H_z}{\partial z^3} = 0$$

$$\frac{\partial^4 H_z}{\partial z^4} = - \frac{3Ia^2}{(a^2 + h^2)^{5/2}} \frac{(-15a^4 + 180a^2 h^2 - 120h^4)}{(a^2 + h^2)^3} .$$

It is clear from (2.14) that for  $h = a/2$  the first three derivatives of  $H_z$  vanish at  $z = 0$  and

$$\frac{\partial^4 H_z}{\partial z^4} = -H_0 \frac{144}{125} \cdot \frac{4!}{a^4} \quad \text{at } z = 0 , \quad (2.15)$$

where

$$H_0 = H_z \Big|_{\text{at } z=0} = \frac{8I}{5^{3/2}a} \quad (2.16)$$

is the value of  $H_z$  at the center of the Helmholtz coils. For later use we now write the following Taylor series approximation to  $H_z$  near  $z \approx 0$  obtained by using (2.13) through (2.16):

$$H_z \approx H_0 \left[ 1 - \frac{144}{125} (z/a)^4 \right] , \quad (2.17)$$

for  $-1/2 < z/a < 1/2$ .

Equation (2.17) is convenient for estimating the variation of the field on the axis near the central region of the Helmholtz coils. From now on we shall assume that  $h = a/2$ , i.e., the separation distance between the two coils is equal to  $a$ .

2.1.3.2 Fields in the Central Region ( $r \rightarrow 0$ ). Using (2.9) and (2.10) the fields in the central region of the Helmholtz coils may be approximated as

$$H_r = H_{r_1} + H_{r_2} \quad (2.18)$$

$$H_z = H_{z_1} + H_{z_2} \quad (2.19)$$

with

$$H_{r_{\frac{1}{2}}} = \frac{3Ia^2}{4} \frac{(z \mp a/2)r}{[(a+r)^2 + (z \mp a/2)^2]^{5/2}} \quad (2.20)$$

$$H_{z_{\frac{1}{2}}} = \frac{Ia^2}{2} \frac{1}{[a^2 + (z \mp a/2)^2]^{3/2}} \left[ 1 + \frac{3}{4} \frac{a^2 - 4(z \mp a/2)^2}{[a^2 + (z \mp a/2)^2]^2} r^2 \right], \quad (2.21)$$

where the subscripts 1 and 2 on the left-hand sides of (2.20) and (2.21) correspond to the negative and positive signs, respectively, on the right-hand sides. From (2.18) and (2.21) it can be seen that in the  $z = 0$  plane,

$$H_r \equiv 0 \quad (2.22)$$

$$H_z = H_0,$$

where  $H_0$  is given by (2.16). Equation (2.22) shows that the Helmholtz coils maintain a constant and axially directed field in a plane parallel to the coils and passing through the center.

We are now in a position to obtain some approximate expressions to estimate the uniformity of the central region fields. Examination of (2.18) through (2.22) reveals that exactly at the center and in the plane  $z = 0$ ,  $H_z = H_0$ ,  $H_r = 0$ . On the axis ( $r = 0$ ),  $H_r \equiv 0$  and the variation of  $H_z$  may be estimated by using (2.17) which is rewritten as:

$$H_z = H_0 \left[ 1 - \frac{\Delta H_z}{H_0} \right], \quad (2.23)$$

where

$$\frac{\Delta H_z}{H_0} = 1.152 \left( \frac{z}{a} \right)^4, \quad -\frac{1}{2} < \frac{z}{a} < \frac{1}{2}. \quad (2.24)$$

If desired, the variation of  $H_z$  with  $r$  in this region may be found using (2.21). From (2.18) and (2.20) the radial component of the field is given by

$$\frac{H_r}{H_0} = \frac{3.5^{3/2}}{32} \left[ \frac{\left( \frac{z}{a} - \frac{1}{2} \right)}{\left[ \left( 1 + \frac{r}{a} \right)^2 + \left( \frac{z}{a} - \frac{1}{2} \right)^2 \right]^{5/2}} + \frac{\left( \frac{z}{a} + \frac{1}{2} \right)}{\left[ \left( 1 + \frac{r}{a} \right)^2 + \left( \frac{z}{a} + \frac{1}{2} \right)^2 \right]^{5/2}} \right] \left( \frac{r}{a} \right) \quad (2.25)$$

for

$$\frac{r}{a} < 1 \quad \text{and} \quad -\frac{1}{2} < \frac{z}{a} < \frac{1}{2},$$

and from (2.24) and (2.25) it can be shown that

$$\frac{\Delta H_z}{H_0} \approx 0.5 \times 10^{-2} \quad \text{at } \frac{z}{a} = \pm \frac{1}{4} \text{ and } r = 0$$

and

$$\frac{H_r}{H_0} \approx 1.0 \times 10^{-2} \quad \text{at } \frac{z}{a} = \frac{r}{a} = \frac{1}{4}.$$

More accurate and detailed expressions for the variation of  $H_z$  and  $H_r$  inside the coils can be found using the exact formulas for the fields given in the next section.

2.1.3.3 Exact Expressions for the Fields. Using (2.7) and (2.8) the following exact expressions for the field produced by the Helmholtz coils can be obtained:

$$H_r = \sum_{n=1}^2 H_{r_n} \quad (2.26)$$

$$H_z = \sum_{n=1}^2 H_{z_n}, \quad (2.27)$$

with

$$H_{r_n} = \frac{I}{2\pi} \frac{z_n}{r[(a+r)^2 + z_n^2]^{1/2}} \left[ -K_n + \frac{a^2 + r^2 + z_n^2}{(a-r)^2 + z_n^2} E_n \right], \quad (2.28)$$

$$H_{z_n} = \frac{I}{2\pi} \frac{1}{[(a+r)^2 + z_n^2]^{1/2}} \left[ K_n + \frac{a^2 - r^2 - z_n^2}{(a-r)^2 + z_n^2} E_n \right]. \quad (2.29)$$

where  $z_1 = z - a/2$ ,  $z_2 = z + a/2$ ,

$K_1, K_2$  are the elliptic integrals defined by (2.4) with arguments

$\kappa_1, \kappa_2$  obtained from (2.3) after replacing  $z$  by  $z - a/2$ ,

$z + a/2$ , respectively; and

$E_1, E_2$  are the elliptic integrals defined by (2.5) with arguments

$\kappa_1, \kappa_2$  obtained in a similar manner.

It should be noted that for  $r = 0$ ,  $H_r \equiv 0$  for all  $z$ .

2.1.4 Numerical Computations. Equations (2.26) and (2.27) were programmed to compute the radial and axial components of the fields normalized with respect to the field at the center, i.e.,  $H_r/H_0$  and  $H_z/H_0$ , respectively, as functions of the normalized coordinates  $r/a$  and  $z/a$ , where  $a$  is the radius of each coil. Selected results for  $H_r/H_0$  and  $H_z/H_0$  at  $r/a = 0(0.25)0.75$  and  $z/a = 0(0.25)0.5$  are given in Table 2.1. The computer program is listed in Appendix A.

The computations were carried out for coils separated in distance  $a$  where  $a$  is the radius of the coil. As expected and seen from the Table, the  $H_z$  component is dominant. At the center ( $r/a = 0$ ,  $z/a = 0$ )

Table 2.1  
Numerical Values for Normalized Field Components

$r/a$	$z/a$	$H_r/H_0$	$H_z/H_0$
0.000000	0.0	0.0	1.0000000000
0.000000	0.250000	0.0	0.9958016347
0.000000	0.500000	0.0	0.9458241852
0.250000	0.0	0.0	0.9982148100
0.250000	0.250000	0.0030530311	1.0069158788
0.250000	0.500000	0.0458272520	0.9718178124
0.499999	0.0	0.0	0.9666290499
0.499999	0.250000	-0.0376688067	1.0361427785
0.499999	0.500000	0.0877231827	1.0812025957
0.749999	0.0	0.0	0.7981811608
0.749999	0.250000	-0.2573269654	1.0205464277
0.749999	0.500000	0.1179854157	1.5052027031

it is unity along the z-axis and decreases to 0.945 (five percent) at  $z/a = 0.5$  ( $r/a = 0$ ) and in the horizontal plane through  $z/a = 0$  decreases to 0.967 (four percent) at  $r/a = 0.5$ . Note at  $r/a = 0.5$ ,  $z/a = 0.5$  the field increases to 1.081 which is expected since this point is closer to the conductor (coil) than the other two points. Observing also that at  $r/a = 0.25$ ,  $z/a = 0.25$  the field is 1.007, it is reasonable to conclude that for a spherical volume of  $r/a = 0.5$  located at the center of the coil system the field will be within  $\pm 5$  percent of the center value  $H_0$ .

On the other hand, in a smaller circular region defined by

$$z/a = \pm 0.25 \quad , \quad r/a = 0.25$$

the deviation of the field is less than one percent from that at the center. For the dimensions selected (see Section 3) this corresponds to a cylindrical volume 30 cm in diameter and 30 cm in height. The scale models typically used in our measurements are no larger than this.

## 2.2 Analysis of Fields Produced by ac Excited Helmholtz Coils

The standard Helmholtz coil arrangement consists of two circular coaxial coils of radius  $a$  spaced  $a$  apart. If each coil carries a similarly directed constant current  $I$  then, as shown in Section 2.1.4, there is a cylindrical region

$$-\frac{a}{2} \leq z \leq \frac{a}{2} \quad , \quad 0 \leq r \leq \frac{a}{4}$$

where the radial magnetic field is negligible and the longitudinal magnetic field is constant to within one percent. It is proposed that



this constitutes the test region of our planned low frequency (magnetic) facility. In order to accommodate a model of overall dimensions up to 0.25 m, it is necessary that the radius of the coils be at least 0.5 m, and the proposal is that  $a = 0.61$  m (2 feet).

There are two sources of a frequency-dependent non-uniformity: (i) variations in the amplitude and/or phase of the current  $I$  excited in each coil, and (ii) the effect of the phasor addition of the contribution of even a uniform current on the near (and far) field of a coil. Since (i) is a function of the manner in which the coils are excited, we shall concentrate only on (ii).

Following Section 2.1.2, consider a circular coil of radius  $a$  in the plane  $z = 0$  of a cylindrical polar coordinate system  $(r, \phi, z)$ . If the coil carries a constant (uniform) current  $I$ , the vector potential at an arbitrary field point is  $\vec{A} = A_\phi \hat{\phi}$  with

$$A_\phi = \frac{\mu I a}{2\pi} \int_0^\pi \frac{ik \sqrt{a^2 + r^2 + z^2 - 2ar \cos \alpha} \cos \alpha e}{\sqrt{a^2 + r^2 + z^2 - 2ar \cos \alpha}} d\alpha \quad (2.30)$$

where a time dependence  $\exp(-i\omega t)$  has been assumed and suppressed.

For small  $ka, kr, kz$ , the exponential can be expanded to give

$$A_\phi = \frac{\mu I a}{2\pi} \left\{ \int_0^\pi \frac{\cos \alpha}{\sqrt{a^2 + r^2 + z^2 - 2ar \cos \alpha}} d\alpha + ik \int_0^\pi \cos \alpha d\alpha + \frac{1}{2} (ik)^2 \int_0^\pi \cos \alpha \sqrt{a^2 + r^2 + z^2 - 2ar \cos \alpha} d\alpha + \dots \right\} \quad (2.31)$$

But

$$\begin{aligned} \int_0^\pi \frac{\cos \alpha}{\sqrt{a^2 + r^2 + z^2 - 2ar \cos \alpha}} d\alpha &= \frac{1}{2} \frac{\kappa}{\sqrt{ar}} \int_0^\pi \frac{\cos \alpha}{\sqrt{1 - \kappa^2 \cos^2 \frac{\alpha}{2}}} d\alpha \\ &= \frac{2}{\kappa \sqrt{ar}} \left\{ \left( 1 - \frac{\kappa^2}{2} \right) K - E \right\} \end{aligned} \quad (2.32)$$

where  $\kappa^2$  is given in (2.3) and  $K$  and  $E$  are the complete elliptic integrals of the first and second kinds respectively, defined in (2.4) and (2.5).

Similarly

$$\begin{aligned} \int_0^\pi \cos \alpha \sqrt{a^2 + r^2 + z^2 - 2ar \cos \alpha} d\alpha \\ = -\frac{4}{\kappa} \sqrt{ar} \int_0^{\pi/2} \cos 2\theta \sqrt{1 - \kappa^2 \sin^2 \theta} d\theta \end{aligned} \quad (2.33)$$

and using integration by parts

$$\begin{aligned} \Lambda &= \int_0^{\pi/2} \cos 2\theta \sqrt{1 - \kappa^2 \sin^2 \theta} d\theta \\ &= - \int_0^{\pi/2} \cos^2 \theta \sqrt{1 - \kappa^2 \sin^2 \theta} d\theta + \int_0^{\pi/2} \frac{\cos^2 \theta}{\sqrt{1 - \kappa^2 \sin^2 \theta}} d\theta \\ &= -\frac{1}{2} \Lambda + \left( 1 - \frac{1}{\kappa^2} \right) K - \left( \frac{1}{2} - \frac{1}{\kappa^2} \right) E, \end{aligned} \quad (2.34)$$

implying

$$\Lambda = -\frac{2}{3\kappa^2} \left\{ (1 - \kappa^2)K - \left(1 - \frac{\kappa^2}{2}\right)E \right\} . \quad (2.35)$$

Since, for  $\kappa^2 \ll 1$ ,

$$\begin{aligned} K &= \frac{\pi}{2} \left\{ 1 + \frac{1}{4} \kappa^2 + O(\kappa^4) \right\} \\ E &= \frac{\pi}{2} \left\{ 1 - \frac{1}{4} \kappa^2 + O(\kappa^4) \right\} \end{aligned} \quad (2.36)$$

it follows that  $\Lambda = 0$  when  $\kappa = 0$ , as required.

From (2.33) and (2.35)

$$\int_0^\pi \cos \alpha \sqrt{a^2 + r^2 + z^2 - 2ar \cos \alpha} \, d\alpha = \frac{8}{3\kappa^2} \sqrt{ar} \left\{ (1 - \kappa^2)K - \left(1 - \frac{\kappa^2}{2}\right)E \right\} , \quad (2.37)$$

and since

$$\int_0^\pi \cos \alpha \, d\alpha = 0 ,$$

we have

$$\begin{aligned} A_\phi &= \frac{\mu I}{\pi \kappa} \sqrt{\frac{a}{r}} \left[ \left(1 - \frac{\kappa^2}{2}\right) K - E - \frac{2ar}{3} \left(\frac{k}{\kappa}\right)^2 \left\{ (1 - \kappa^2)K \right. \right. \\ &\quad \left. \left. - \left(1 - \frac{\kappa^2}{2}\right)E \right\} + O(k^3) \right] . \quad (2.38) \end{aligned}$$

The first term, independent of  $k$ , is identical to that in Eq. (2.2).

In terms of  $\bar{A}$  the radiated field is

$$\bar{H} = \frac{1}{\mu} \nabla \times \bar{A} , \quad \bar{E} = ik Z \frac{1}{\mu} \bar{A}$$

where  $Z = 1/Y$  is the free space impedance, implying

$$H_r = -\frac{1}{\mu} \frac{\partial A_\phi}{\partial z} , \quad H_z = \frac{1}{\mu r} \frac{\partial}{\partial r} (r A_\phi) ,$$

$$YE_\phi = ik \frac{1}{\mu} A_\phi , \quad (2.39)$$

with all other components zero. It follows immediately from (2.38) that

$$YE_\phi = ik \frac{I}{2\pi r} \left\{ (a+r)^2 + z^2 \right\}^{1/2} \left[ \frac{a^2 + r^2 + z^2}{(a+r)^2 + z^2} K - E \right. \\ \left. - \frac{k^2}{6} \left\{ ((a-r)^2 + z^2) K - (a^2 + r^2 + z^2) E \right\} + O(k^3) \right] \quad (2.40)$$

and using the expansions (2.36) it can be shown that  $E_\phi = 0$  on the axis  $r = 0$  of the coil.

To determine the magnetic field we first note that

$$\frac{\partial \kappa}{\partial r} = \frac{\kappa}{2r} \frac{a^2 - r^2 + z^2}{(a+r)^2 + z^2} , \quad \frac{\partial \kappa}{\partial z} = -\frac{\kappa^3 z}{4ar} .$$

Also, from [7]

$$\frac{dK}{d\kappa} = -\frac{1}{\kappa} \left( K - \frac{1}{1-\kappa^2} E \right) , \quad \frac{dE}{d\kappa} = -\frac{1}{\kappa} (K - E)$$

implying

$$\frac{d}{d\kappa} \left[ \frac{1}{\kappa} \left\{ \left( 1 - \frac{\kappa^2}{2} \right) K - E \right\} \right] = - \frac{1}{\kappa^2} \left\{ K - \frac{1 - \kappa^2/2}{1 - \kappa^2} E \right\}$$

$$\frac{d}{d\kappa} \left[ \frac{1}{\kappa^3} \left\{ (1 - \kappa^2)K - \left( 1 - \frac{\kappa^2}{2} \right) E \right\} \right] = - \frac{3}{\kappa^4} \left\{ \left( 1 - \frac{\kappa^2}{2} \right) K - E \right\} .$$

After some rather tedious manipulation it now follows that

$$H_r = \frac{I}{2\pi r} \frac{z}{\{(a+r)^2+z^2\}^{1/2}} \left[ -K + \frac{a^2+r^2+z^2}{(a-r)^2+z^2} E - \frac{k^2}{2} \left\{ (a^2+r^2+z^2)K - ((a-r)^2+z^2)E \right\} + O(k^3) \right] \quad (2.41)$$

and

$$H_z = \frac{I}{2\pi} \frac{1}{\{(a+r)^2+z^2\}^{1/2}} \left[ K + \frac{a^2-r^2-z^2}{(a-r)^2+z^2} E + \frac{k^2}{2} \left\{ (a^2-r^2-z^2)K + ((a+r)^2+z^2)E \right\} + O(k^3) \right] \quad (2.42)$$

The leading terms in (2.31) and (2.32) are in agreement with those given in Eqs. (2.7) and (2.8).

For small  $r$  such that  $2ar \ll a^2+z^2$  we have, to the first non-zero term in  $r$ ,

$$YE_\phi = ik \frac{I}{2} \frac{a^2 r}{(a^2+z^2)^{3/2}} \left[ 1 - \frac{k^2}{2} (a^2+z^2) + O(k^3) \right] \quad (2.43)$$

$$H_r = \frac{3I}{2} \frac{a^2 r z}{(a^2+z^2)^{5/2}} \left[ 1 + \frac{k^2}{6} (a^2+z^2) + O(k^3) \right] \quad (2.44)$$

$$H_z = \frac{I}{2} \frac{a^2}{(a^2+z^2)^{3/2}} \left[ 1 + \frac{k^2}{2} (a^2+z^2) + O(k^3) \right] . \quad (2.45)$$

$E_\phi$  and  $H_r$  are both proportional to  $r$  and therefore vanish on the axis, whereas  $H_z$  is non-zero when  $r = 0$ . For  $H_r$  and  $H_z$  the frequency-dependent correction is proportional to  $k^2(a^2+z^2)$ , and in the cylindrical region  $|z| \leq a$  the correction is less than one percent if  $ka < 0.1$ . This condition is satisfied for a coil not exceeding 0.95 m in diameter operated at 10 MHz.

The proposed facility consists of two identical coils spaced  $a$  apart, identically excited. In the resulting test region (of overall length  $a/2$ ) the variation of  $H_z$  along the axis can be obtained from (15). The center of the region corresponds to  $z = a/2$  in (15), and here

$$H_z \Big|_{z=a/2} = \frac{I}{a} 0.3578 [1 + 0.625(ka)^2 + O(k^3)] .$$

Similarly,

$$H_z \Big|_{z=a/4} = \frac{I}{a} 0.4565 [1 + 0.531(ka)^2 + O(k^3)]$$

and

$$H_z \Big|_{z=3a/4} = \frac{I}{a} 0.2560 [1 + 0.781(ka)^2 + O(k^3)] ,$$

the sum of which is

$$\frac{I}{a} 0.7125 [1 + 0.621(ka)^2 + O(k^3)] .$$

This differs by less than one percent from twice the value at  $z = a/2$  (the factor 2 corresponding to the two coils). The uniformity of the field throughout the test region that was derived in Section 2.1 for static fields is therefore maintained if  $ka \leq 0.1$ .

### 2.3 Other Considerations

In using the magnetostatic facility certain problems now arise, three of which are as follows: (i) The desired surface magnetic field is that at a specific point on the target when illuminated by a plane linearly polarized wave incident in a given direction, and this excitation is quite different from that provided by a pair of Helmholtz coils; (ii) at low frequencies the metallized target no longer looks perfectly conducting; and (iii) the low frequency expansion is not uniform in the magnetic properties of the target. A non-magnetic body having  $\mu = \mu_0$  has no effect on a magnetostatic field (the surface magnetic field is that of the incident field alone). The static result for a "perfect conductor" corresponds to the non-physical situation for which  $\mu = 0$ , and with any actual highly conducting material there is a frequency below which the field starts to diverge from that for a perfect conductor. We shall examine these topics in the reverse order.

2.3.1 Quasi-Magnetostatic Behavior. To examine the low frequency behavior of the surface magnetic field, consider the simple problem of a homogeneous sphere of permittivity  $\epsilon$ , permeability  $\mu$  and radius  $a$  illuminated by the plane electromagnetic wave

$$\vec{E}^{inc} = \hat{x} e^{ikz}, \quad \vec{H}^{inc} = \hat{y} e^{ikz}.$$

Note that the time convention ( $e^{-i\omega t}$ ) and the direction of incidence differ from those used in Appendix C, Part 3.

As shown by, for example, Stratton [2], the total magnetic field is

$$Z_0 \bar{H} = - \sum_{n=1}^{\infty} i^n \frac{2n+1}{n(n+1)} \left\{ \bar{m}_{\text{ein}}^{(1)} + b_n \bar{m}_{\text{ein}}^{(3)} + i(\bar{n}_{\text{oin}}^{(1)} + a_n \bar{n}_{\text{oin}}^{(3)}) \right\} \quad (2.46)$$

where

$$a_n = - \frac{\mu_r \Gamma^{(1)}(ka) - \Gamma^{(1)}(k_1 a)}{\mu_r \Gamma^{(3)}(ka) - \Gamma^{(1)}(k_1 a)} \cdot \frac{j_n(ka)}{h_n^{(1)}(ka)} \quad (2.47)$$

and

$$b_n = - \frac{\epsilon_r \Gamma^{(1)}(ka) - \Gamma^{(1)}(k_1 a)}{\epsilon_r \Gamma^{(3)}(ka) - \Gamma^{(1)}(k_1 a)} \cdot \frac{j_n(ka)}{h_n^{(1)}(ka)} \quad (2.48)$$

with  $\epsilon = \epsilon_r \epsilon_0$ ,  $\mu = \mu_r \mu_0$ ,  $k_1 = k \sqrt{\epsilon_r \mu_r}$  and

$$\Gamma^{(1)}(x) = \frac{[x j_n(x)]'}{j_n(x)}, \quad \Gamma^{(3)}(x) = \frac{[x h_n^{(1)}(x)]'}{h_n^{(1)}(x)} \quad (2.49)$$

If  $|ka|$ ,  $|k_1 a| \ll 1$ , the coefficients  $a_n$  and  $b_n$  can be expanded in powers of  $ka$ . In particular,

$$a_1 = \frac{2i}{3} (ka)^3 \frac{\mu_r - 1}{\mu_r + 2} + O[(ka)^5]$$

implying



$$b_1 = \frac{2i}{3} (ka)^3 \frac{\epsilon_r - 1}{\epsilon_r + 2} + O[(ka)^5],$$

and

$$a_2 = \frac{i}{15} (ka)^5 \frac{\mu_r - 1}{2\mu_r + 3} + O[(ka)^7]$$

implying

$$b_2 = \frac{i}{15} (ka)^5 \frac{\epsilon_r - 1}{2\epsilon_r + 3} + O[(ka)^7].$$

The low frequency expansions of the tangential components of the total magnetic field on the surface  $r = a$  of the sphere are then as follows:

$$ZH_\theta = \sin \phi \left\{ \frac{3}{\mu_r + 2} \cos \theta + \frac{ika}{2} \left[ \frac{3\epsilon_r}{\epsilon_r + 2} + \frac{5}{2\mu_r + 3} \cos 2\theta \right] + O[(ka)^2] \right\} \quad (2.50)$$

$$ZH_\phi = \cos \phi \left\{ \frac{3}{\mu_r + 2} + \frac{ika}{2} \cos \theta \left[ -\frac{3\epsilon_r}{\epsilon_r + 2} + \frac{5}{2\mu_r + 3} \right] + O[(ka)^2] \right\}$$

We observe that the static (zeroth order) terms are functions only of the relative permeability and that for a non-magnetic material ( $\mu_r = 1$ )

$$\bar{H} = \bar{H}^{inc}$$

independent of the electrical conductivity. On the other hand, for a perfectly conducting sphere it is known that

$$\begin{aligned}
ZH_{\theta} &= \frac{3}{2} \sin \phi \left\{ \cos \theta + ika \left[ 1 + \frac{5}{9} \cos 2\theta \right] + O[(ka)^2] \right\} \\
ZH_{\phi} &= \frac{3}{2} \cos \phi \left\{ 1 + ika \cos \theta \left[ -1 + \frac{5}{9} \right] + O[(ka)^2] \right\}
\end{aligned} \tag{2.51}$$

which is otherwise obtained by putting  $\epsilon_r = \infty$  and  $\mu_r = 0$  in (2.50). We remark that the assumptions made in the expansions leading to (2.50) may be violated if  $\epsilon_r = \infty$ .

For a conducting material

$$\epsilon_r = \tilde{\epsilon}_r + iZ \frac{\sigma}{k} \tag{2.52}$$

where  $\tilde{\epsilon}_r$  is the (real) relative permittivity and  $\sigma$  is the conductivity. The relevant factor is  $\sigma/k$ , which is infinite for a perfect conductor. Moreover, any material for which  $\sigma \neq 0$  "looks" perfectly conducting in the static limit, and if  $\sigma/k$  is large,

$$k_1 = (1 + i) \sqrt{\frac{1}{2} k Z \mu_r \sigma} \left\{ 1 + O\left(\frac{k}{\sigma}\right) \right\}. \tag{2.53}$$

Consider now the exact expressions (2.47) and (2.48) for the coefficients in the Mie series. We observe that these involve  $k_1$  only via the term  $\tau_1^{(1)}(ka)$ , and for large  $|x|$

$$\tau_1^{(1)}(x) = 1 + x \frac{j_n'(x)}{j_n(x)} = x \tan \left\{ x - (n+1) \frac{\pi}{2} \right\} \left\{ 1 + O(|x|^{-1}) \right\}.$$

For large  $\text{Im } x$  regardless of  $\text{Re } x$ ,

$$\tan \left\{ x - (n+1) \frac{\pi}{2} \right\} \sim i$$

implying

$$r^{(1)}(k_1 a) = ik_1 a \quad (2.54)$$

which tends to infinity as  $k\mu_r\sigma \rightarrow \infty$ . Hence, if  $k\mu_r \neq 0$ , the perfectly conducting limit of (2) is

$$a_n = - \frac{j_n(ka)}{h_n^{(1)}(ka)} \quad (2.55)$$

as used in the derivation of (6). We remark that the same result is obtained by putting  $\mu_r = 0$  in (2).

For the coefficient  $b_n$  the relevant quantity is  $\epsilon_r/\Gamma^{(1)}(k_1 a)$ . If the body is conducting ( $\sigma \neq 0$ ), (7) and (9) imply

$$\frac{\epsilon_r}{\Gamma^{(1)}(k_1 a)} = \frac{e^{-i\pi/4}}{ka} \sqrt{\frac{Z\sigma}{k\mu_r}} \quad (2.56)$$

which becomes infinite as  $\sigma \rightarrow \infty$  (perfect conductivity), and/or  $k \rightarrow 0$  (static), and/or  $\mu_r \rightarrow 0$ . In each case (2.48) reduces to

$$b_n = - \frac{[ka j_n(ka)]'}{[ka h_n^{(1)}(ka)]'} \quad (2.57)$$

which is the known result for perfect conductivity, as used in the derivation of (2.51).

The conclusions of the above analysis are as follows. For a conducting material having  $\sigma \neq 0$ , the low frequency expansion of the electric coefficient  $b_n$  is uniform in  $\sigma$  and the result for perfect conductivity can be obtained by putting  $\epsilon_r = \infty$  in the

expression for arbitrary permittivity. For the magnetic coefficient  $a_n$ , however, the expansion is not uniform, and for given  $\mu_r$ ,  $\sigma \neq 0$  there is a value of  $ka^2 Z\mu_r\sigma$  below which the solution is no longer characteristic of a perfect conductor. The result for perfect conductivity cannot now be obtained from the expression for a general material, implying that, in the present instance, there is a minimum frequency at which the facility can be operated. In particular, a quasi-magnetostatic facility would be inappropriate.

From (2.53) the requirement is that

$$|k_1 a| = (ka^2 Z\mu_r\sigma)^{1/2} \gg 1 ,$$

for example,

$$ka \geq 10^4 (aZ\mu_r\sigma)^{-1} \quad (2.58)$$

If  $\sigma = 10^{-7}$  mhos/m (appropriate for silver),  $\mu_r = 1$  and  $a = 0.125$  m, (2.58) implies.

$$ka \geq 2.1 \times 10^{-5} ,$$

corresponding to a minimum frequency of 8 kHz. A larger body would permit a smaller minimum frequency. If, in addition,

$$ka \leq 0.05$$

implying a maximum frequency of 19 MHz, the first term in the low frequency expansion is sufficient, and that term is the one for a perfect conductor (see 2.51). A larger body would reduce proportionally the maximum allowed frequency.

2.3.2 Effect of Penetration Depth. It is highly desirable that the planned facility be able to employ models which are identical (or similar) to those used in our present facility. These models are, in general, plastic with a thin coating of silver paint to simulate a highly conducting metal. The coating thickness  $t$  is typically 0.1 mm (= 4 mils) and this should be at least twice the penetration depth  $\delta$  in the paint. From (2.53)

$$\delta = \left( \frac{1}{2} k Z \mu_r \sigma \right)^{-1/2}$$

and the requirement therefore is

$$t \geq 2 \left( \frac{1}{2} k Z \mu_r \sigma \right)^{-1/2} ,$$

implying

$$k \geq 8(Z \mu_r \sigma t^2)^{-1} .$$

If  $t = 0.1$  mm,  $\mu_r = 1$  and  $\sigma = 10^7$  mhos/m, the minimum frequency is 10 MHz. This exceeds the minimum frequency demanded in the previous section, and in conjunction with the maximum imposed by the requirement that the first term in the low frequency expansion for a 0.25 m model suffice, narrows the allowed frequency range to

$$10 \leq f(\text{MHz}) \leq 19 .$$

To accommodate a model somewhat larger than 0.25 m in overall dimension (as well as other considerations), it is suggested that the facility be designed to operate as close to 10 MHz as possible.

2.3.3 Excitation. If a perfectly conducting (metallic) body is exposed to an electromagnetic field, the leading (magnetostatic) term in the low frequency expansion for the total magnetic field is determined by the leading term in the low frequency expansion of the incident magnetic vector. In particular, neither the incident electric vector nor the direction of propagation of the incident field has any effect. As an example, in the case of a plane wave incident on a sphere (see Section 2.3.1),

$$H_{\theta}|_{k=0} = \frac{3}{2} H_{\theta}^{\text{inc}}|_{k=0} = \frac{3}{2} \hat{y} \cdot \hat{\theta} \quad , \quad H_{\phi}|_{k=0} = \frac{3}{2} H_{\phi}^{\text{inc}}|_{k=0} = \frac{3}{2} \hat{y} \cdot \hat{\phi} \quad .$$

Of course, for a more general body  $H_{\text{tan}}$  will not be simply proportional to  $H_{\text{tan}}^{\text{inc}}|_{k=0}$ .

The facility that has been proposed consists of two identical Helmholtz coils of radius  $a$  spaced  $a$  apart. Between the coils there is a cylindrical region where the magnetic field is parallel to the axis and almost constant in amplitude, with the electric field circumferential. This is conceived to be the test region where the model is placed, and is in the extreme near field of each coil. As a result the field to which the body is exposed is quite different from a plane wave, but since the magnetic vector is constant in amplitude and direction, it does simulate a plane wave as regards the magnetostatic term. This is all that is required.

### 3. PHYSICAL DESIGNS

As a result of theoretical studies discussed in Section 2 it was decided that the facility would consist of Helmholtz coils approximately 0.5 m in radius spaced one radius apart. At zero frequency this would provide a test region of cylindrical volume consisting of two feet in diameter and two feet in height where the magnetic field is uniform to within  $\pm 5$  per cent. It has also been shown that if the current in the coils is constant in amplitude and phase, the frequency dependent variation of the magnetic field throughout the test region will be less than one per cent if  $f \leq 10$  MHz.

From the considerations of the magnetic field response of typically used models, the requirement on the measurement frequency is just the opposite. A non-ferrous metal does not appear perfectly conducting at low frequencies, and the problem becomes more pronounced for metallized (silver painted plastic) models used in scale model measurements. These topics were discussed in Section 2.3.2 where it was shown that for a 0.1 mm (4 mills) thick silver coating on a plastic model a minimum frequency of about 10 MHz is required to simulate it as a magnetic conductor. On the other hand, a model made of solid silver would allow a minimum frequency of about 8 kHz. Of course, the use of magnetic materials and coatings would lower the minimum frequency to zero but we have not considered it at this time due to the difficulties anticipated in making or obtaining models of such materials. It was therefore decided to construct a facility to operate at 10 MHz but design the feed

system for the coils such that they can be excited over wider frequency range and, then, from the results of evaluation measurements determine the appropriate operating range of frequencies for the facility. The following parameters were specified at the beginning of the program:

- (i) geometry - coaxial Helmholtz coils, single turn, 4 feet in diameter spaced 2 feet apart
- (ii) operating frequency - 10 MHz
- (iii) excitation - at four points on each coil
- (iv) current in each coil - as much as practical, in the range 0.1 to 1.0 A (RMS)
- (v) structure - four 4 x 8-foot plates butted together

With the coils horizontally placed as shown in Fig. 3.1 and using the above guidelines, two facilities with different design philosophy were constructed. One, using plywood support plates and inductive drivers for the excitation of Helmholtz coils, and the other, using aluminum support plates and gap drivers in the coils. Henceforth, the two facilities will be referred to as the Plywood and Aluminum Facilities, respectively, which were constructed and tested also in that order. The two facilities are described in Sections 3.1 and 3.2.

### 3.1 Plywood Facility

#### 3.1.1 The Structure

The facility was constructed by using four 4 x 8-foot 3/4-inch thick plywood sheets butted together as shown in Fig. 3.1 and held together with a frame made out of 2 x 4's. In each sheet a semi-circular hole of radius  $\sqrt{5} = 2.24$  feet was cut to form a spherical volume at the center that also supported the coils and provided access to the working or test



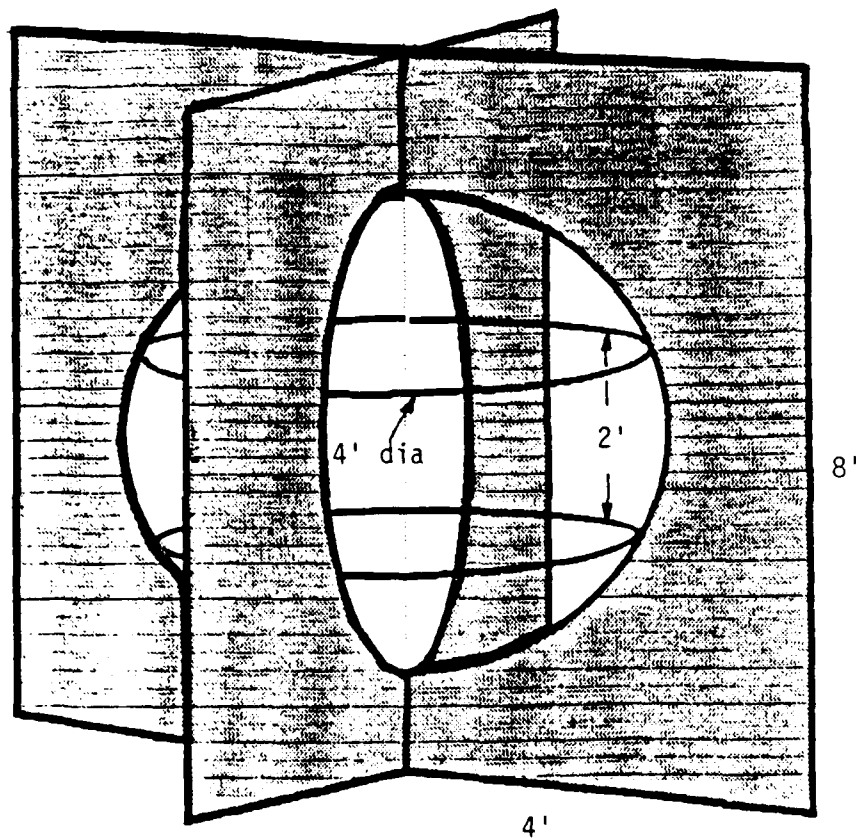


Fig. 3.1: Helmholtz coil geometry with support structure.

region. The Helmholtz coils were made from 0.25 inch (0.0.) copper tubing that came in a 3-foot diameter spool and hence was relatively easy to re-shape into 4-foot diameter loops whose ends were then butted to form a short circuited loop.

The diagram showing the excitation of the facility is given in Fig. 3.2. Originally the idea here was to use four equally spaced current drivers (such as, EG&G CCD01 or CCD02) on each coil, all driven with signals having equal amplitude and phase. A distribution transformer was designed and fabricated to provide the required eight uniform signals. The transformer and other components associated with the facility are described in the next section.

### 3.1.2 Current Drivers

Although the CCD01 or CCD02 current drivers could have worked satisfactorily, we were not able to obtain sufficient numbers of them and, therefore, we designed and built our own drivers.

An important consideration in the design of the drivers is the load (Helmholtz coil) inductance which dictates the current that can be induced in the coil. From computations and later verified by measurement (Appendix E) it was found that the inductance of a single loop is about  $5 \mu\text{H}$ , which at 10 MHz has a reactance of 300 ohms or 75 ohms per each driver since there are four drivers on each coil. If the driver is now considered as a transformer with one turn secondary (a coil of 75 ohm impedance), there will be an impedance mismatch at the primary side when referenced to 50 ohms, because more than one turn is needed in the primary for the excitation of the magnetizing field. The torroidal cores that we chose were T8525 (CMD5005) from Ceramic Magnetics. Based on the criterion that the driver behaves as an ideal transformer it was

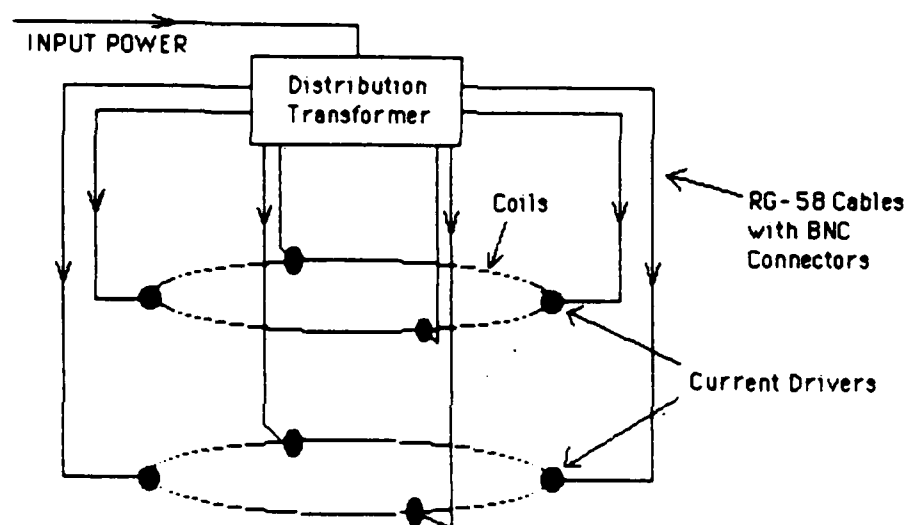


Fig. 3.2: Excitation diagram for the Plywood Facility.

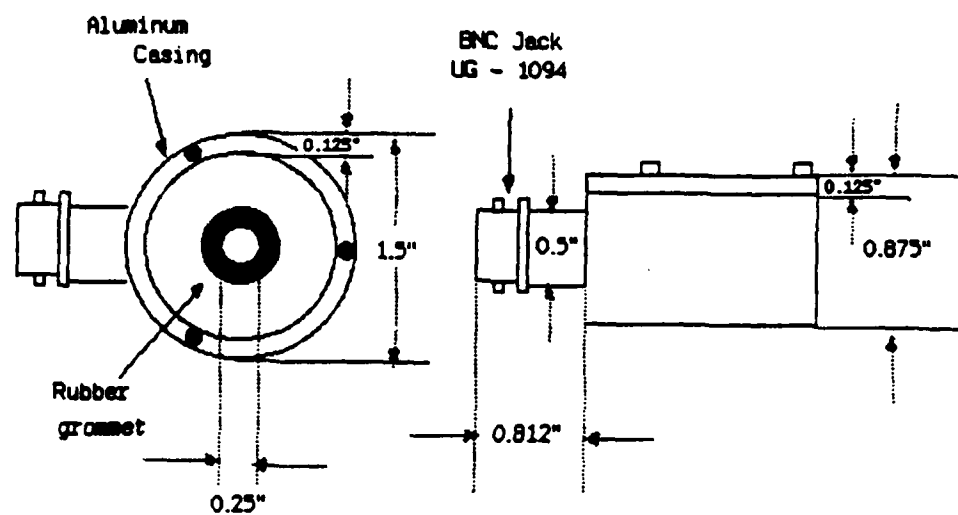
determined that six turns would be required in the primary. Under this condition and with the secondary open, the measured impedance of the six-turn primary was found to be 2000 ohms at 10 MHz. (In retrospect, it now appears that fewer turns in the primary may have provided a better overall performance of the facility, even though the primary impedance might have approached the 50 ohm characteristic impedance of the connecting coaxial lines.)

The driver core with six-turn No. 20 copper wire winding was then mounted in an aluminum housing shown in Fig. 3.3. Holes were drilled in the housing to thread or place the unit on the coil which had to be broken (unshorted) to do so. The BNC connector is for connecting the input line. Figure 3.4 shows photographs of these drivers.

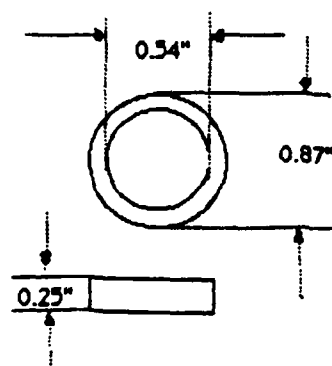
### 3.1.3 Distribution Transformer

The purpose of this device was to provide uniform (equal amplitude and phase) signals to each of the eight driver transformers mounted on the two coils. Again, a torroidal core transformer design was used but this time with 24-turn primary and eight 3-turn secondaries. The core selected was Amidon T-200-2 similar to that used in 1 KW amateur radio transmitter output circuit. Even though the choice of turns ratio was based on considerations to provide uniform signals to each of the eight outputs, it was found that the output voltages were not identical. The open circuit voltage measured at 7.88 MHz with a 10 Meg probe on individual secondary terminals with the other terminals terminated in 100 ohms varied from 16.8 to 17 mV in amplitude and 0 to -2.6 degrees in phase.

Figure 3.5 shows a drawing of the aluminum housing in which the transformer was placed. Each of the eight BNC outputs were connected with matched lengths of RG-58A/U cable to the respective current driver mounted



A) Casing ( housing the toroid )



B) Toroid (CMD 5005 T8525 )

Fig. 3.3: Aluminum housing for the current drivers.



(a) Driver with open cover to show the core and the winding.



(b) Cover closed. Note its size relative to a dime.

Fig. 3.4: Current driver for Helmholtz coils. There is a total of eight of these in the facility.

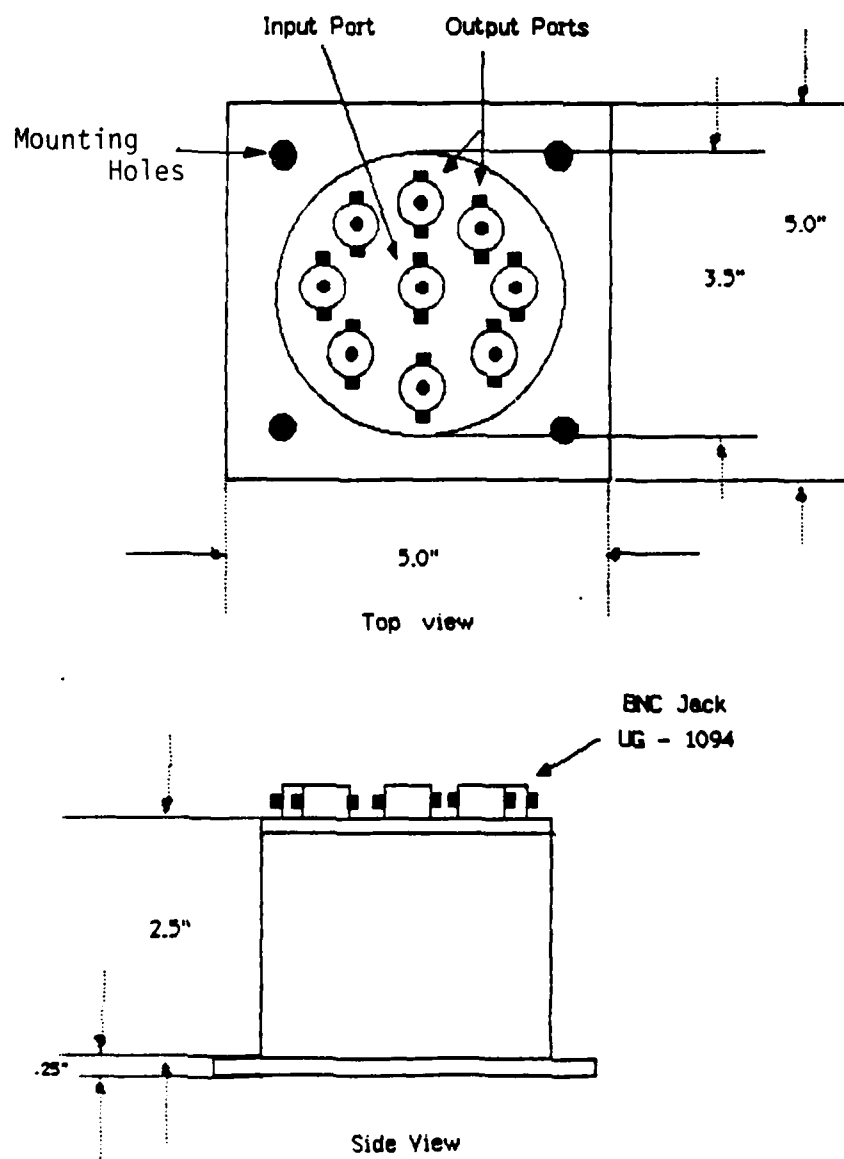


Fig. 3.5: Distribution transformer housing for the Plywood Facility.

on the coils. Voltages were again measured, this time with the 10 Meg probe connected at the output of a given cable with the other seven cables connected to appropriate current drivers. Table 3.1 shows that the amplitude of the signals varies slightly more than the case when measured at the terminals of the distribution transformer, but the phase deviates by as much as 9.6 degrees which should be compared to 2.6 degrees obtained in the previous case.

Table 3.1  
Drive Signal Voltages

Driver No.	Transf Port	Voltage at Transf Terminals		Voltage at Coil Drivers	
		Rel Amp,mv	Rel Phase,Deg	Rel Amp,mv	Rel Phase, Deg
1A	1	18.0	0.0	13.7	0.0
1B	2	16.9	-0.9	13.1	-8.1
2B	3	16.8	-2.2	13.0	-2.3
2A	4	16.9	-2.6	13.5	-8.6
3B	5	16.9	-2.2	13.1	-3.0
3A	6	16.8	-2.0	13.2	+1.0
4B	7	17.1	-2.4	13.8	-0.6
4A	8	17.0	-1.8	13.5	-1.4

The measurements presented in Table 3.1 were made using a 100 mW signal generator set at 7.88 MHz. This frequency was dictated by the optimum operation of the facility in conjunction with a Heathkit 25 watt amateur radio transmitter which we originally anticipated using as the high power source required for making current measurements using 2-3 mm diameter loop probes. However, the Heathkit transmitter was discarded after we acquired a 25 watt (1-500 MHz) power amplifier.



#### 3.1.4 Tuning of the Facility

When we started to examine the current drivers for the Helmholtz coil it became apparent that due to impedance mismatch in the drivers, tuning of the facility would be required to obtain efficient excitation of the coils. We considered and tried tuning the source, the distribution transformer, the drivers, and even the coils by introducing series capacitors in the loops. Most of these approaches turned out to be impractical and we finally decided to use sections of coaxial lines as "quarter-wave matching devices" connected between the distribution transformer and the current drivers. After carrying out some experimental and theoretical (Appendix D) studies the optimized length of these cables was found to be 18 foot. When tuning the facility, either the MGL-6A(A) or the MTL-2A(ER) sensor was used to detect the magnetic fields and since the two sensors provided sufficient signal output even with a couple of milliwatts drive, a single generator (without an amplifier) covering 1-30 MHz range sufficed.

#### 3.2 Aluminum Facility

After it was recognized that the Plywood Facility with transformer drivers will operate only at a single frequency (although it could be retuned by changing cable lengths), we also proceeded with the design and construction of the Aluminum Facility. This facility uses gap excitations of coils instead of coupling transformers and metal plates instead of plywood to ensure more uniform field distribution within. The metal plates also allow routing of coaxial leads along the surface with minimum interaction with the field.

The shape and size of the Aluminum Facility are the same as those of the Plywood Facility, and that is where the similarities end. The

4 x 8-foot plates were made of 1/8-inch thick aluminum, the coils and feed lines were made of 0.141-inch semirigid 50-ohm coax and the connectors used were of the SMA-series type. The distribution transformer (North Hill, Model 0011) had differential outputs +V and -V voltages required to drive the coils.

Figure 3.6 shows a photograph of the facility with a prolate spheroid model inside. Dimensions of the facility are shown in Fig. 3.7. The details of implementation of the four excitation gaps in each loop are shown in Fig. 3.8. Each loop is fed by four coaxial lines originating from the distribution transformer. Four of the lines (two from each coil) are connected to each side at the output of the transformer and to improve the impedance matching, 39 ohm (2 watt) resistors were added in series with each line [8]. The lines were very carefully matched in length to within 0.125 inches by measuring the distance with a Time Domain Reflectometer from the input end that connects at the transformer to the gap in the coil.

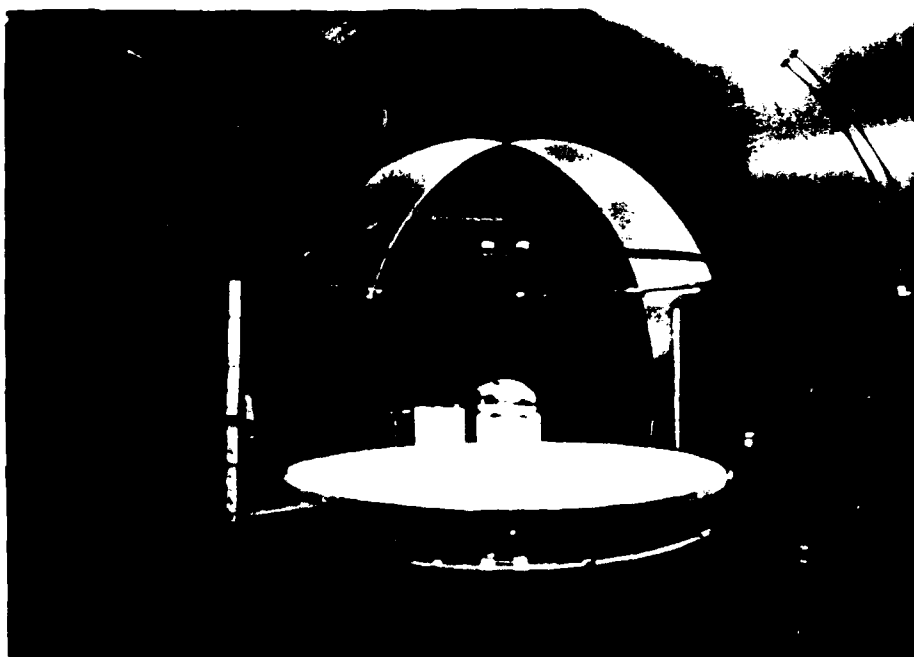


Fig. 3.6: Aluminum Facility shown with a 2:1 prolate spheroid (4.5 by 9.0 inches) mounted for measurement.

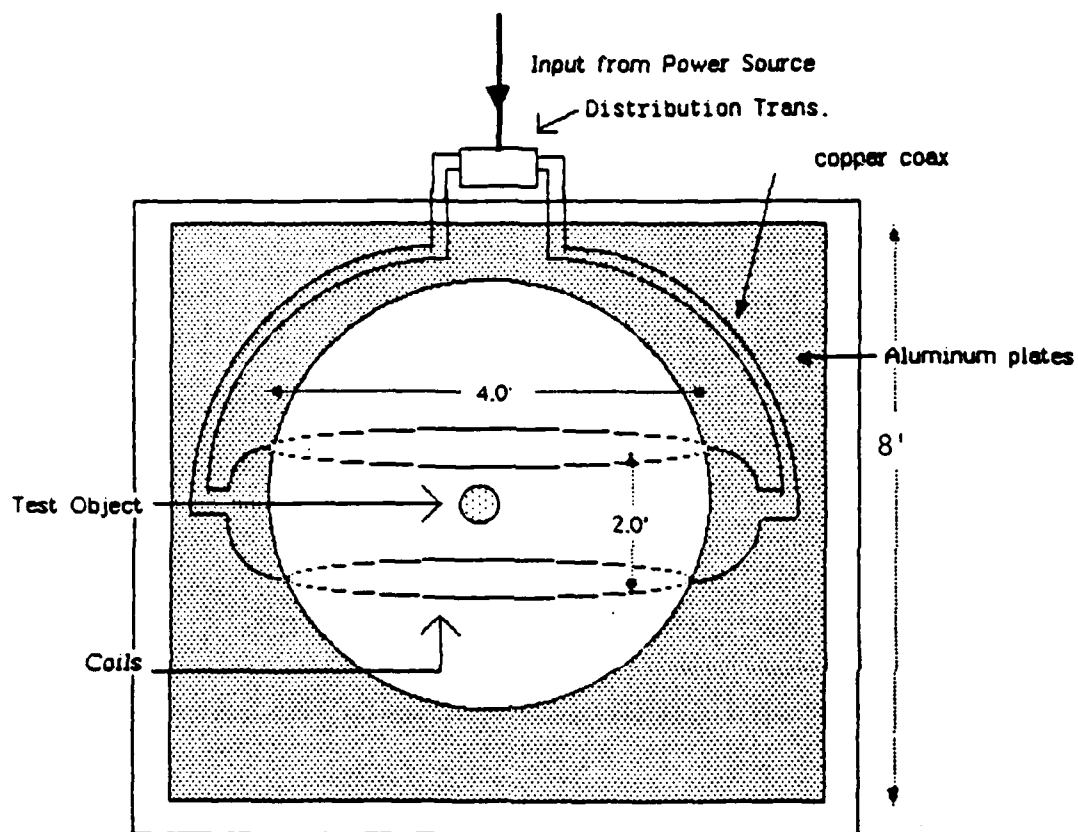
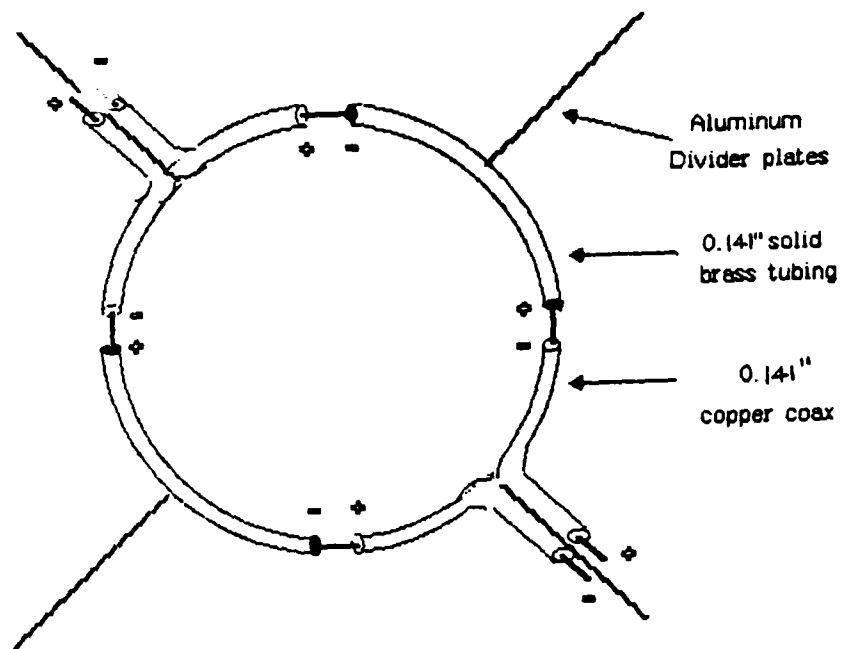


Fig. 3.7: Dimensions of the Aluminum Facility.



(a) Voltage polarity diagram.



(b) Photograph of the feed gap.

Fig. 3.8: Implementation of the feed gaps.

#### 4. TESTS AND EVALUATION OF FACILITIES

After construction of the two facilities, each was evaluated by measuring:

- (a) the magnetic field to determine the field intensity distribution within the coils
- (b) the sensitivity, i.e., the field intensity per given power input
- (c) frequency response.

The measurements were carried out by using the experimental set-up shown in Fig. 4.1. An EG&G MTL-2A(A) B-dot sensor in conjunction with DTL-96D balun was used to measure the magnetic field. Since the sensor has relatively large sensitivity ( $A_{eq} = 0.01 \text{ m}^2$ ), no power amplifier on the driver side nor pre-amplifier on the sensor side was required. A 50-100 mw CW signal generator was used to drive the coils. Part of the signal (from the directional coupler) was fed to the vector voltmeter in Port A to provide the reference signal. The test signal was fed directly from the sensor (or the probe) into Port B. Thus, a given measurement consisted of recording the voltage amplitude at Port B and the phase difference between the voltages at Ports B and A.

The evaluation measurements for both facilities were performed in a similar manner. For field probing the MTL-2A(A) sensor was scanned through a cylindrical volume:  $r = 0, 4, \dots, 24$  inches;  $\phi = 0, 45, \dots, 315$  degrees; and  $z = \pm 20$  inches which resulted in measurements at  $6 \times 8 \times 11 + 11 = 539$  points for each test frequency. During these

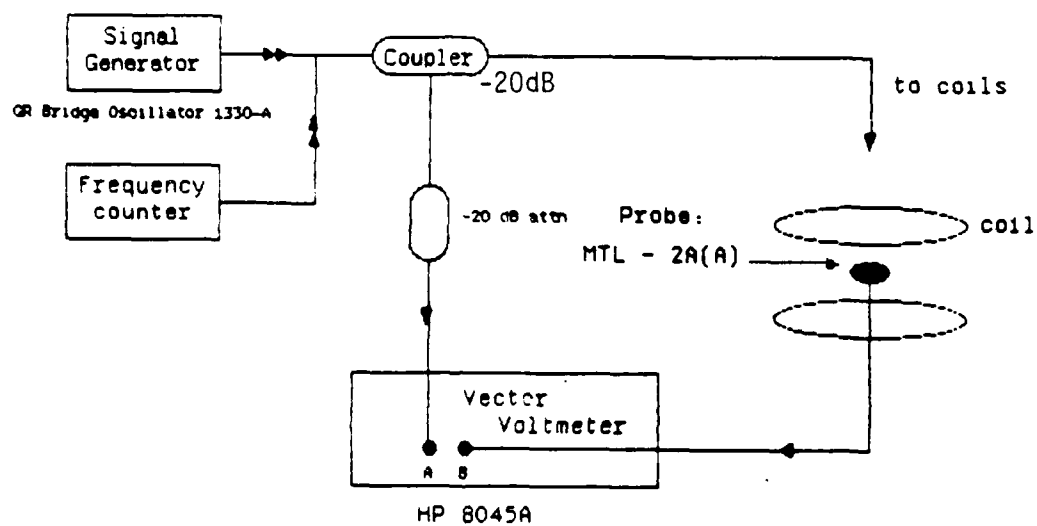


Fig. 4.1: Experimental set-up to measure fields for Plywood and Aluminum Facilities.

measurements appropriate care was taken to position the handle of the sensor and the signal lead in a radially outward direction so as to minimize interaction with the (small) electric fields present in the  $\pm$  directions. Figure 3.6 shows the styrofoam platform whose surface contained the  $r$  and  $\phi$  coordinates so as to facilitate the placement of the sensor. The entire platform was raised appropriately up and down to move the sensor in the  $z$ -directions.

#### 4.1 Plywood Facility Field Plots

Since the Plywood Facility operates efficiently only at a single frequency and had to be retuned by changing the power distribution cable lengths to operate at another frequency, the field measurements were carried out only at 7.875 MHz. As mentioned previously, 539 measurements were made at a given frequency and the data were reduced in terms of contours for  $\pm 5\%$  deviations of the field from its value at the center.

Figure 4.2 shows the results obtained in the horizontal planes  $z = 0$  and  $z = \pm 4$  inches. It can be seen from Fig. 4.2 that the plots are approximately circular, and they become larger as one goes up or down from the center plane, since the measurement position is then approaching closer to the coils. Figure 4.3 shows the results obtained in the horizontal planes  $z = \pm 6$  inches, but here the two circles are not of the same size, and this is due to the fact that the  $\pm 5$  percent boundary values vary rapidly at  $z = \pm 4$  inches which can be seen from Fig. 4.4 that gives the vertical plane results.

The vertical plane results in Fig. 4.4 show the uniformity of the field intensity more explicitly. The curves in Fig. 4.4 indicate that the contours are not continuous: the +5 percent contours are near the conductors while the -5 percent contours are in between the



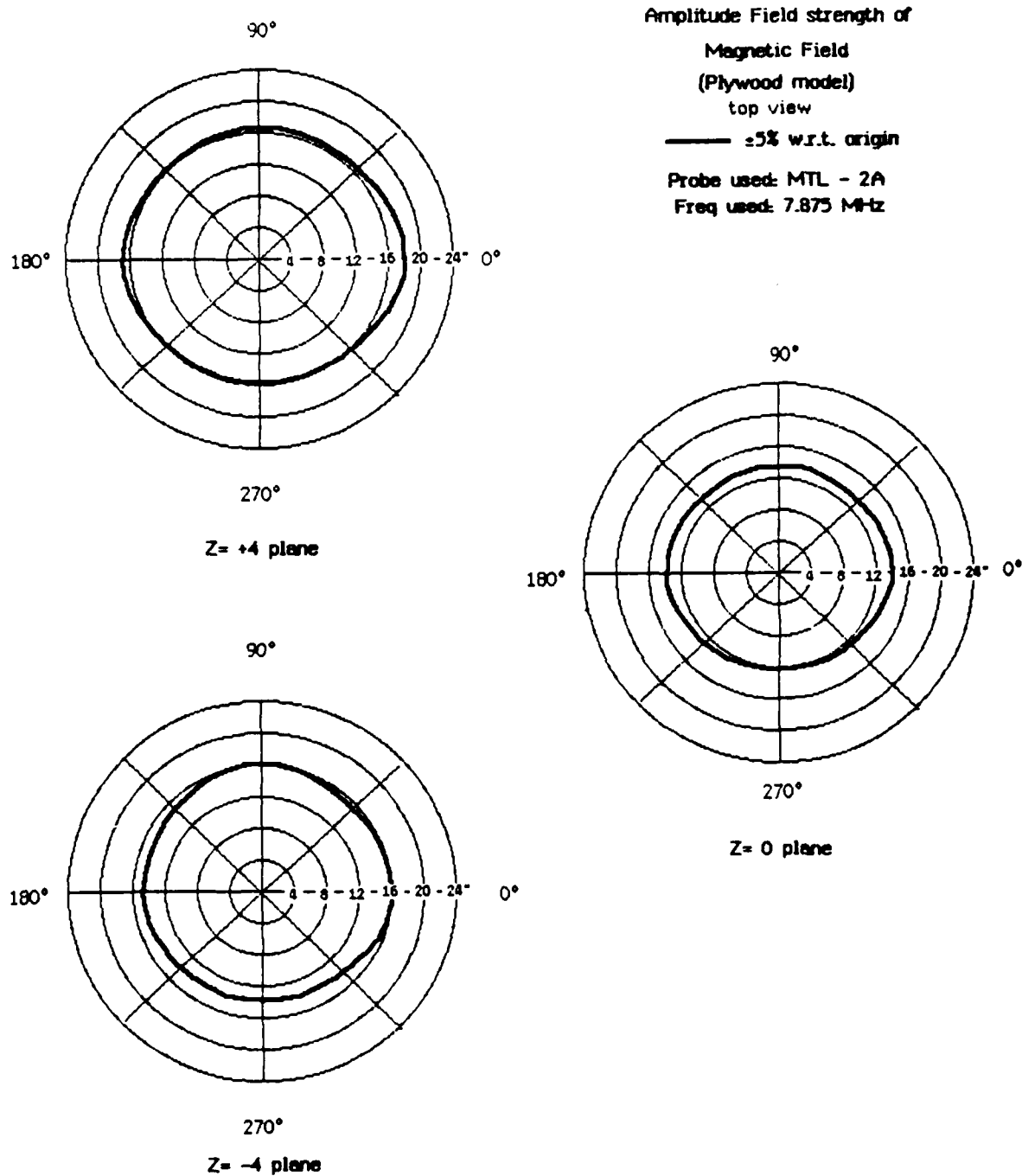


Fig. 4.2: Horizontal plane results at  $z=0, \pm 4$  inches (Plywood Facility).

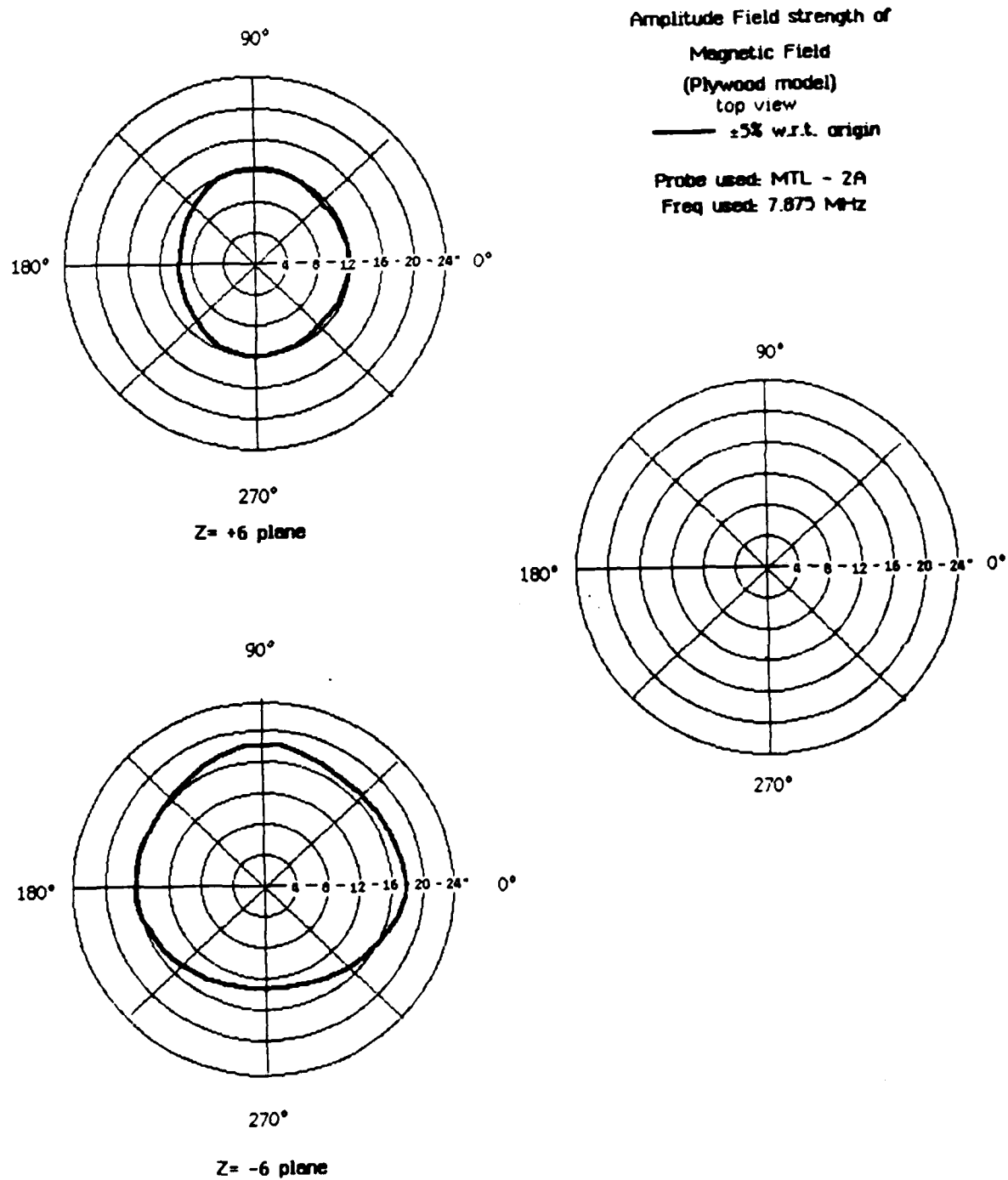


Fig. 4.3: Horizontal plane results at  $z=\pm 6$  inches (Plywood Facility).

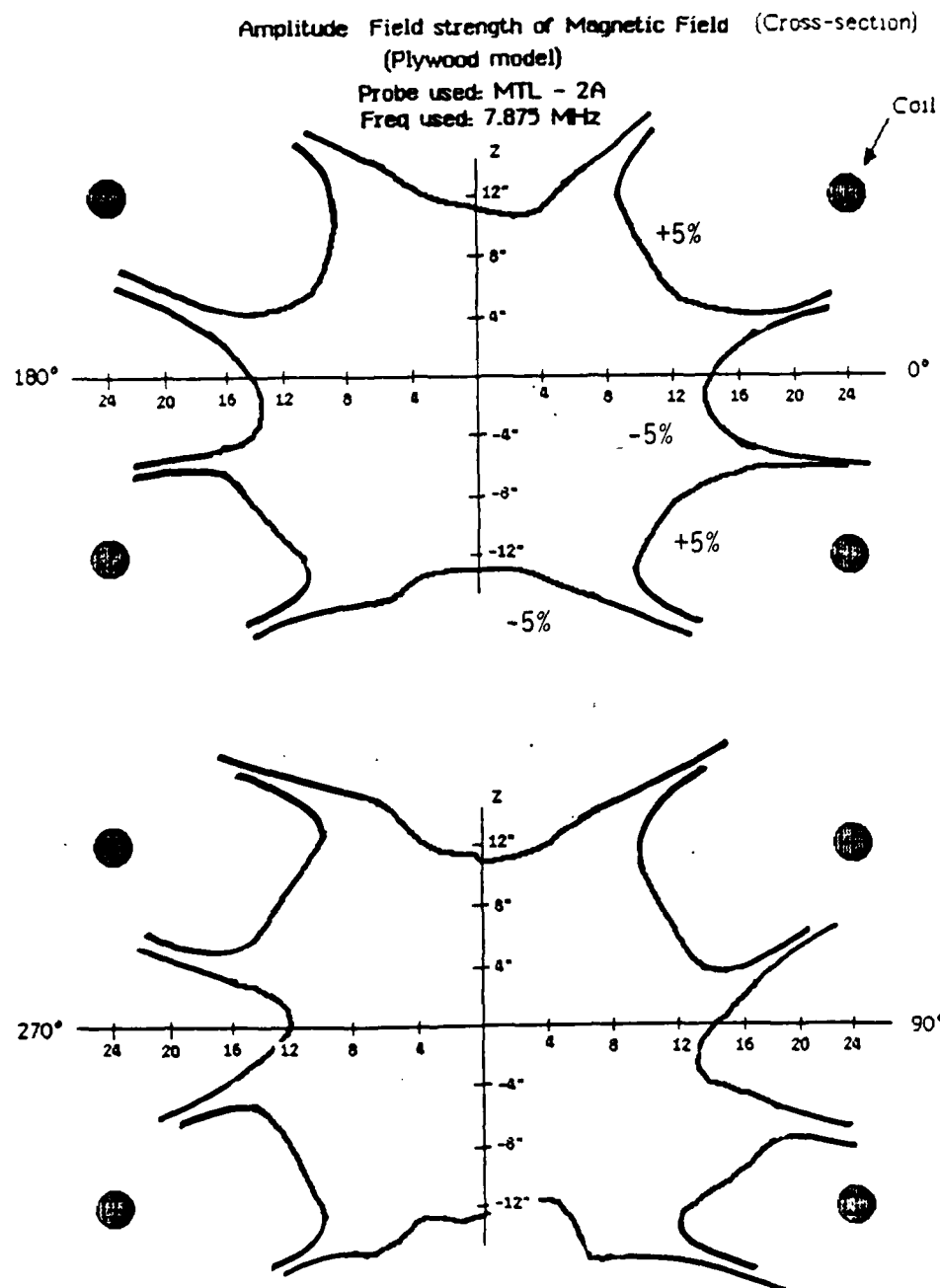


Fig. 4.4: Vertical plane results at  $\theta=0$  and  $\theta=90$  degrees (Plywood Facility).

conductors. As expected from the circular plots obtained in the horizontal planes (Figs. 4.2 and 4.3), there is little difference between the results in the 0-degree and 90-degree planes.

Overall, it was found that the Plywood Facility provides a uniform field with a maximum of  $\pm 5$  percent variations within a spherical volume of radius 12 inches and this is consistent with the theoretical predictions of Table 2.1.

#### 4.2 Aluminum Facility Field Plots

Whereas the Plywood Facility was probed at the single frequency of 7.875 MHz, the field measurements with the Aluminum Facility were carried out at 7.875, 10.000, and 15.000 MHz. As was pointed out in the previous sections, the horizontal plane results provide very little information other than the deviations from the (ideal) circular contours; hence, we show the data for only 10.000 MHz. Figures 4.5 and 4.6 show the results obtained at the horizontal planes  $z = 0$  and  $\pm 4$ ,  $z = \pm 7$  inches respectively. The results of Fig. 4.6 show the maximum of such deviations, and again, this can be attributed to the rapid variations of the fields at this height.

Figures 4.7, 4.8, and 4.9 show the vertical ( $\phi = 90^\circ$ ) plane results obtained at 7.875, 10.000, and 15.000 MHz, respectively. These results indicate that the contour lines are essentially invariant with frequency, although a closer inspection does show that the  $\pm 5$  percent contour tends to move slightly towards the center with increasing frequency. Therefore, we conclude that for the frequencies considered the facility provides a uniform field with a maximum of  $\pm 5$  percent deviation over a spherical volume of radius 12 inches. Again, this is consistent with the design values (Table 2.1).

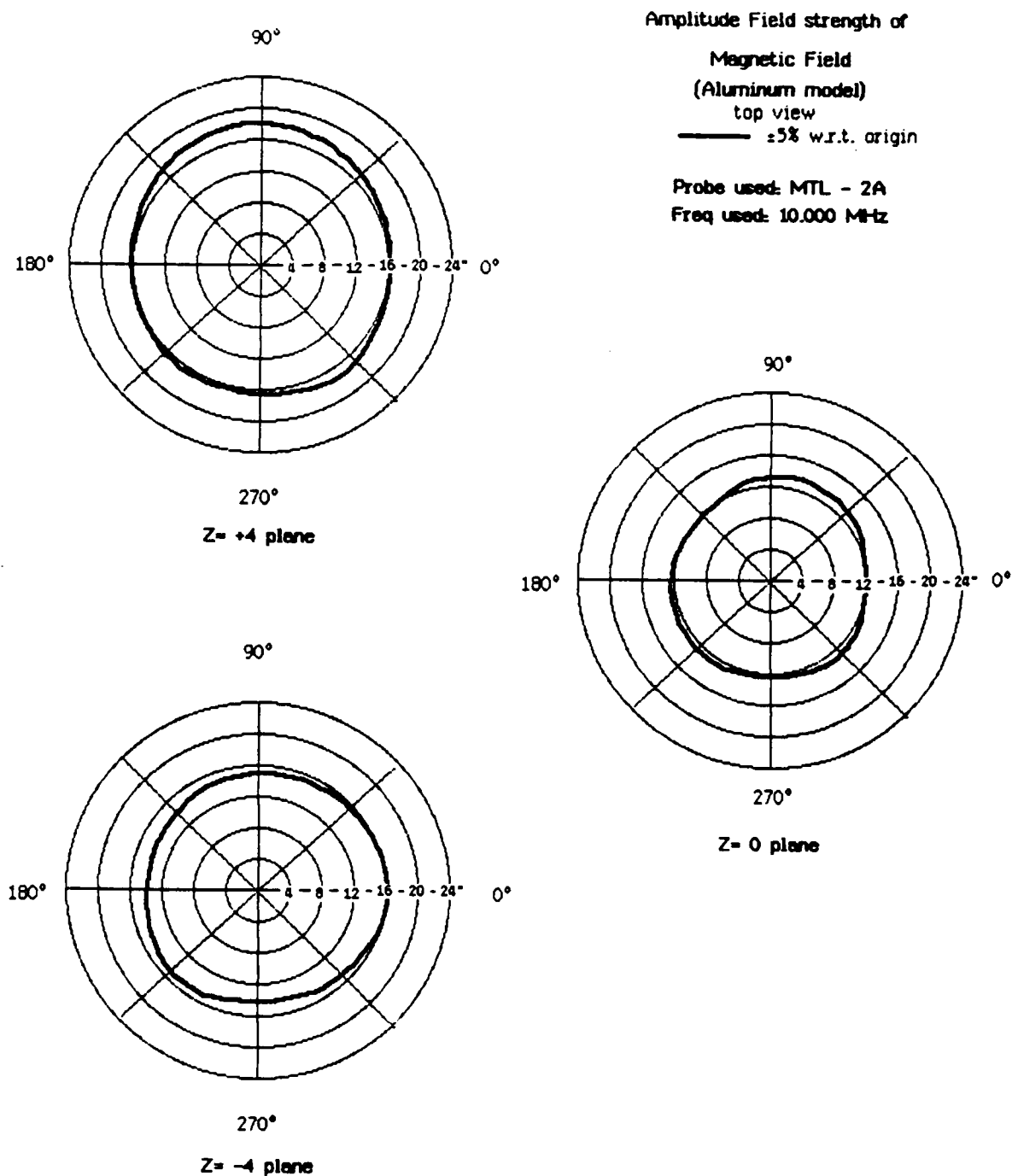


Fig. 4.5: Horizontal plane results at  $z=0, \pm 4$  inches (Aluminum Facility).

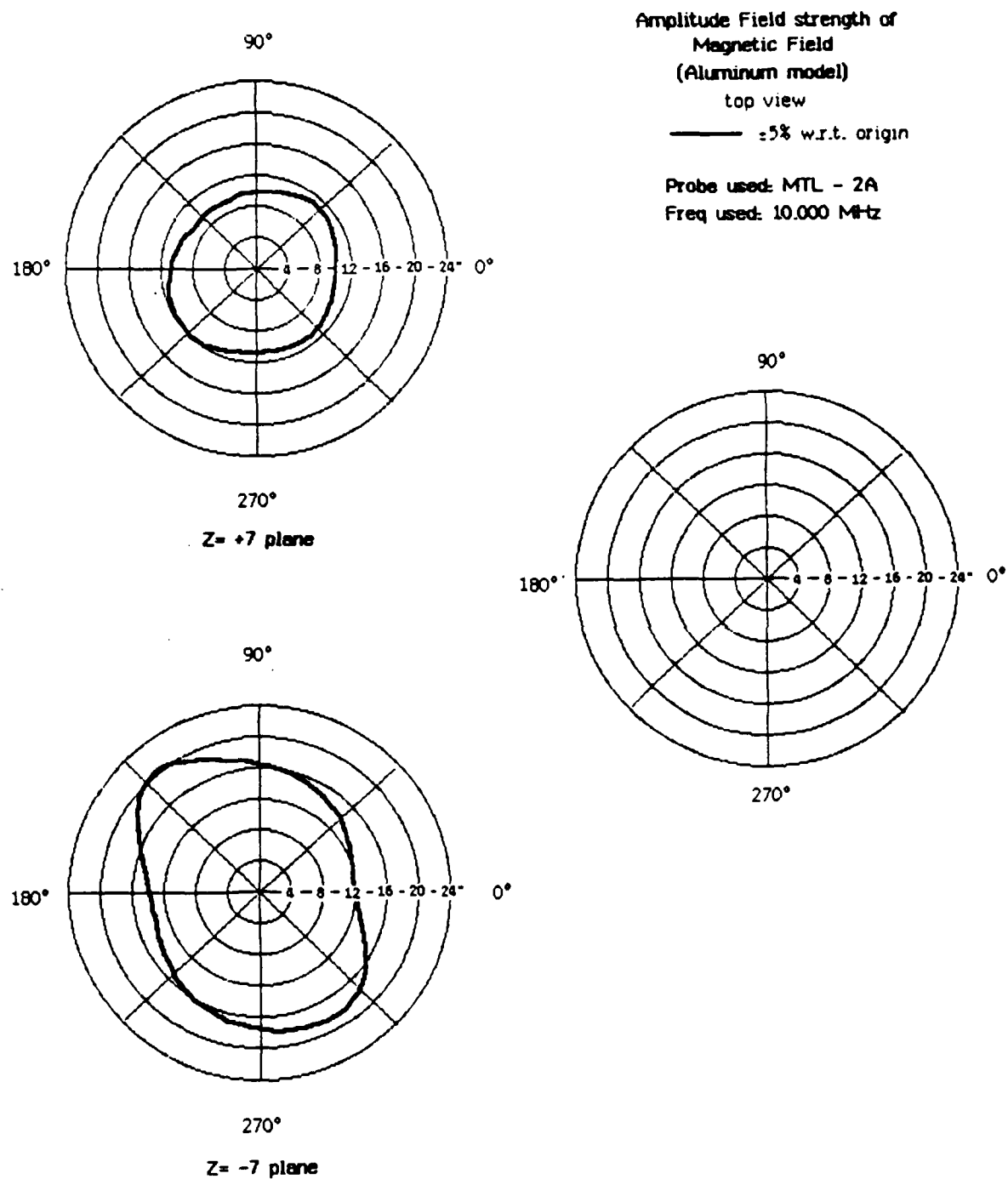


Fig. 4.6: Horizontal plane results at  $z=\pm 7$  inches (Aluminum Facility).

Aluminum Facility  
FREQ = 7.875 MHz  
Plot  $\pm 5\%$  field profile  
w.r.t. origin  
Probe used: MTL - 2A (A)

$\theta = 90^\circ$  quadrant

Interpolated Data

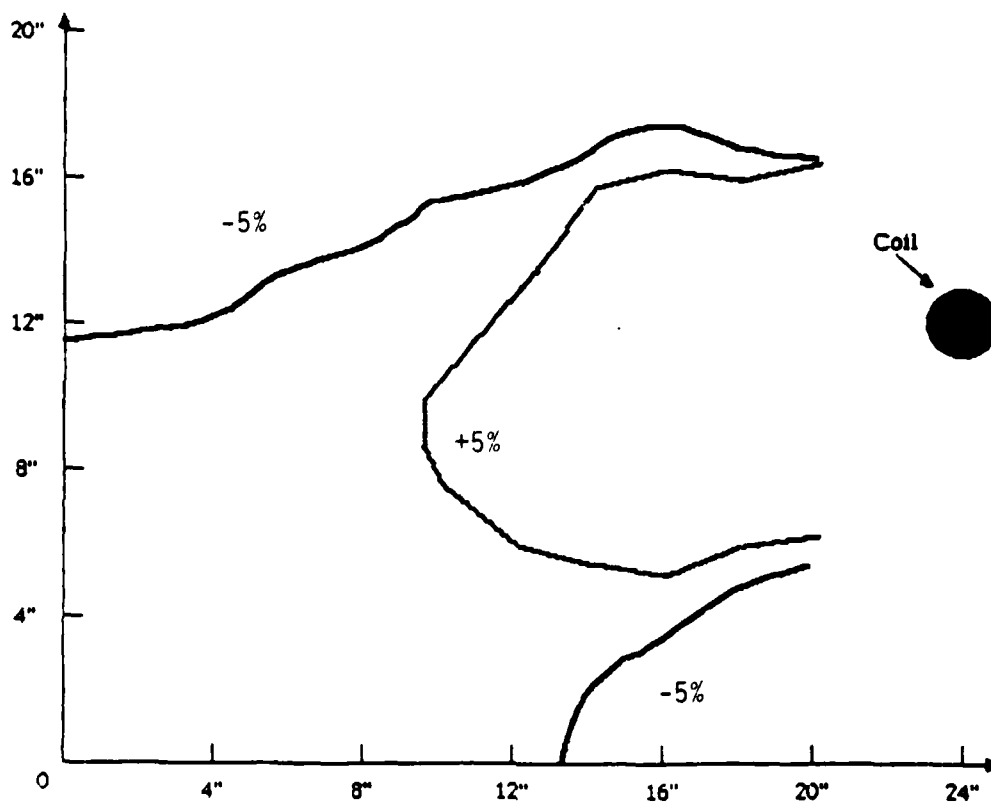


Fig. 4.7: Vertical plane results at  $\theta = 90$  degrees,  $f = 7.875$  MHz (Aluminum Facility).

Aluminum Facility  
FREQ = 10.000 MHz  
Plot  $\pm 5\%$  field profile  
w.r.t. origin  
Probe used: MTL - 2A (A)

$\theta = 90^\circ$  quadrant

Interpolated Data

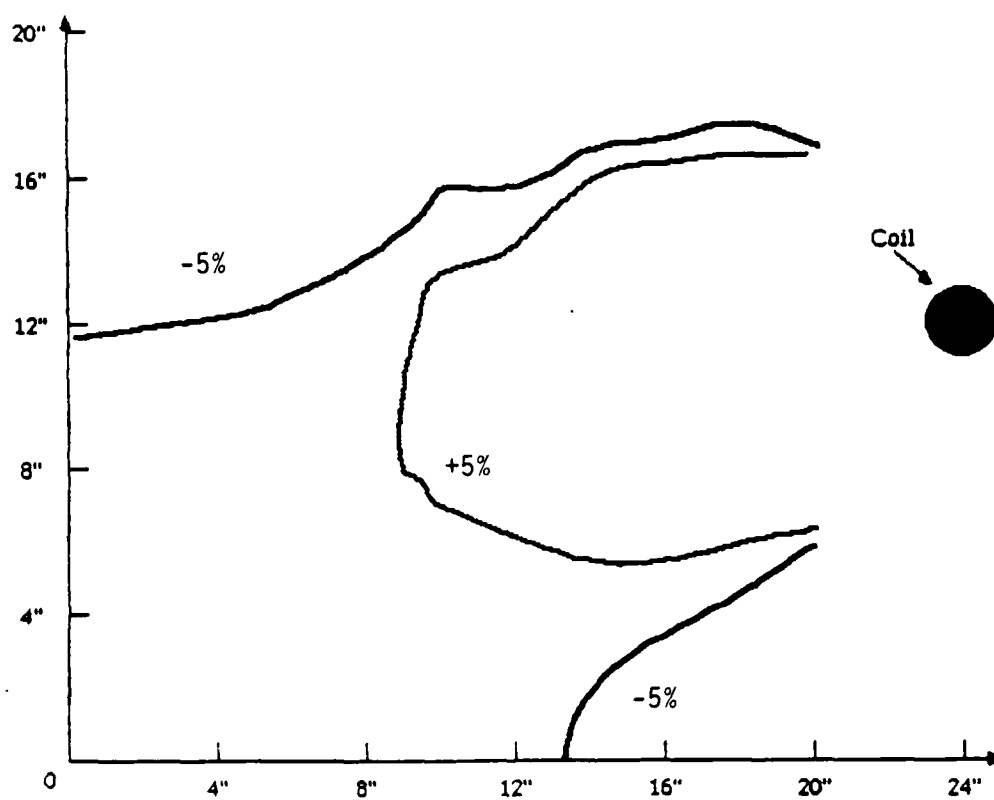


Fig. 4.8: Vertical plane results at  $\theta=90$  degrees,  $f=10.0$  MHz (Aluminum Facility).



Aluminum Facility  
FREQ = 15.000 MHz  
Plot  $\pm 5\%$  field profile  
w.r.t. origin  
Probe used: MTL - 2A (A)

$\theta = 90^\circ$  quadrant

Interpolated Data

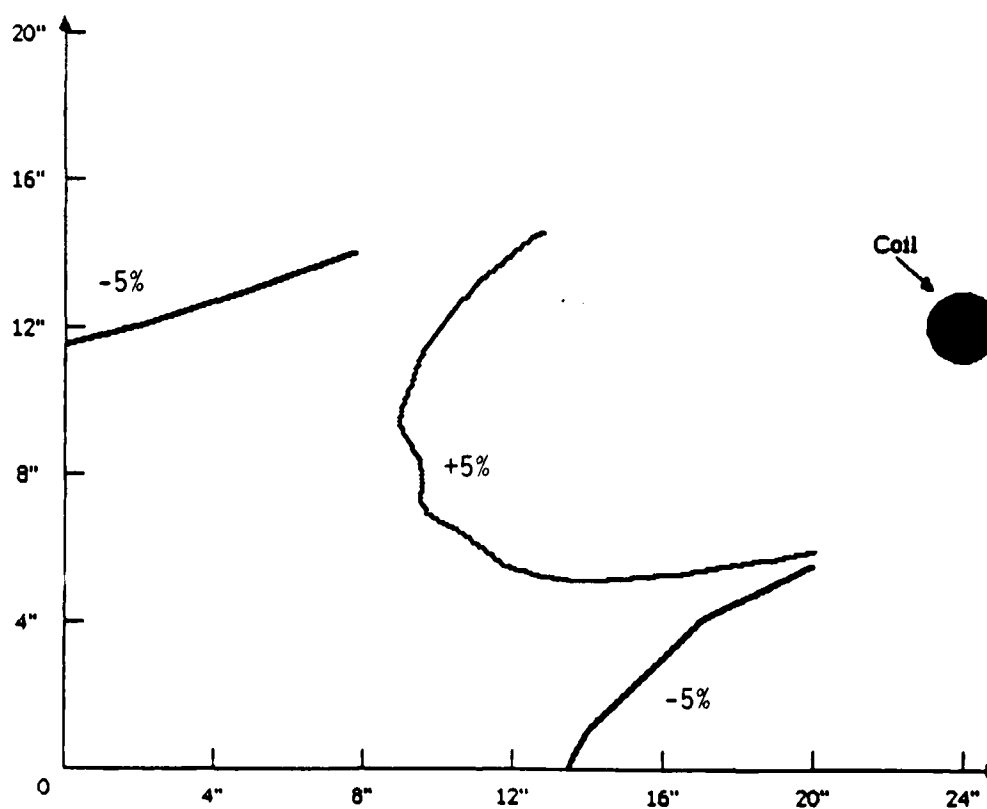


Fig. 4.9: Vertical plane results at  $\theta=90$  degrees,  $f=15.0$  MHz  
(Aluminum Facility).

### 4.3 Comparison of the Two Facilities

On comparing the field plots obtained at 7.875 MHz with the Plywood and Aluminum Facilities it is found that the field responses of the two are similar and, in fact, the plywood facility produces a slightly larger working volume. However, this should not be the only criterion for making a choice between the two. A more important criterion is the frequency range over which the facility can be operated effectively.

To determine the frequency range of operation, we used the set-up shown in Fig. 4.1 with the sensor positioned at the center of the working volume, and recorded its output voltage  $V_b$  and drive voltage  $V_a$  over 1-30 MHz. Measurements were carried out with the Plywood and Aluminum Facilities. The frequency responses of the two facilities obtained from the above measurements are shown in Fig. 4.10 which indicates that the aluminum facility is superior. The field in the Plywood Facility is in general smaller and shows a resonance at 12 MHz. This frequency is a function of the coil and transformer inductances and feed-line lengths, and by varying the feed-line lengths this resonant frequency can be changed (see Appendix D). Above 12 MHz the Aluminum Facility produces much higher fields for the same input drive and shows a strong resonance at 18 MHz. Since at 18 MHz  $ka \approx 0.23$  ( $k$  is the wave number and  $a$  is the radius of the coil), the peak response is not due to the loop resonance for which  $ka \approx 1$  would be appropriate. However, the feed line lengths from the transformers to the driver gaps in the coils (see Fig. 3.6) are about 0.25 wavelengths, and these could be the cause of the resonance. In the measurements we have performed so far the resonances have not been a problem. But if the resonance effects do become critical in the future measurements, these can be reduced considerably by changing the matching

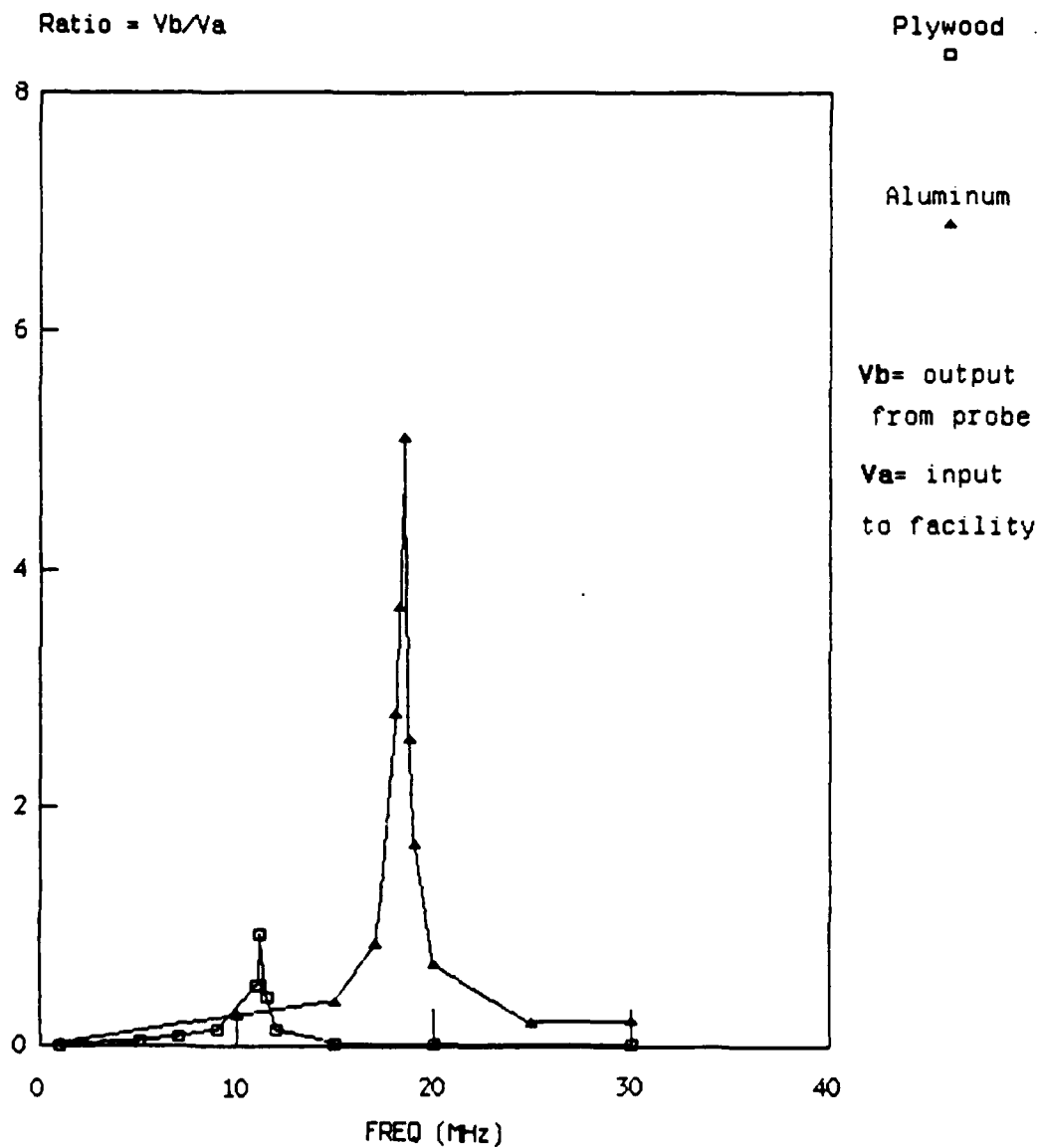


Fig. 4.10: Comparison of frequency response of the two facilities.

resistors at the distribution transformer and/or by resistively loading the coils at the feed gaps.

## 5. SAMPLE MEASUREMENTS

The evaluation study of the Plywood and Aluminum Facilities indicated that the latter is superior, and consequently, the plywood facility was dismantled. The measurements presented in this section were all made in the Aluminum Facility.

To make the measurements of the surface currents on a given body a sensor (or probe) much smaller than the MTL-2A(A) must be used. Designs for miniature MTL constructions were also considered but not used. Then we tried to use our own 2-3 mm diameter loops that we generally use in the broadband (100-4700 MHz) chamber measurements and found that these can indeed be used in the present magnetostatic measurements. The measurements that we made were exploratory in nature, and as our measurement techniques improved, so did the accuracy of measurements. The models used for measurement were aluminum spheres, brass cylinders, and a silver painted F-106 plastic model.

### 5.1 Spheres and Cylinders

The experimental set-up used was as shown in Fig. 4.1 except that the MTL-2A(A) was replaced by a miniature (2-3 mm diameter) shielded loop. At a given frequency the sequence of measurements was to record the probe voltage with the sphere present (measuring total magnetic field  $H$ ) and without the sphere present (measuring incident magnetic field  $H_0$ ). The ratio of the two measurements, i.e.,  $H/H_0$ , yielded the surface field normalized to the incident field. Measurements were performed at 8 MHz

using loop probes in sizes from 2.7 to 7.5 mm diameter on 3-inch and 6-inch diameter aluminum spheres. The measured value of  $H/H_0$  ranged from 1.35 to 1.88 (from Mie theory the exact value is 1.5). At the beginning, the measurements were noisy and unrepeatable, mostly due to signal leakage into the signal cables. By carefully aligning and taping down the leads in outward radial directions from the magnetostatic facility, we were able to reduce most of the coupling effects; under these conditions surface field ratios of 1.45 - 1.47 were obtained with a 3 mm diameter loop on the 6-inch sphere.

We then proceeded to perform measurements at 7.1 MHz using a set of brass cylinders. A total of 11 hollow cylindrical shells (with open ends) ranging in diameter from 0.125 to 2.125 inches were cut 12.0 inches in length from thin-walled brass tubing. For a measurement a given cylinder was placed on its end in the facility and appropriate readings were taken with and without the model. The diameter of the loop probe used was 2.6 mm.

The results of the above measurements are shown in Fig. 5.1. It should be noted that in the case of an infinitely long cylinder the surface field ratio should be 2.0. Our measurement results in Fig. 5.1 show that the ratio is 1.2 for the smallest diameter and it approaches 1.7 as the diameter increases. The 1.2 value obtained for small diameter cylinders is due to the probe integration or averaging effects over the area of the probe. The fact that the upper value of 1.7 is different from 2.0 may be due to the finite length of the cylinders.

## 5.2 Measurements on NASA F-106B Model

To demonstrate the usefulness of the facility for system analysis studies, sample measurements were carried out with a NASA F-106B scale

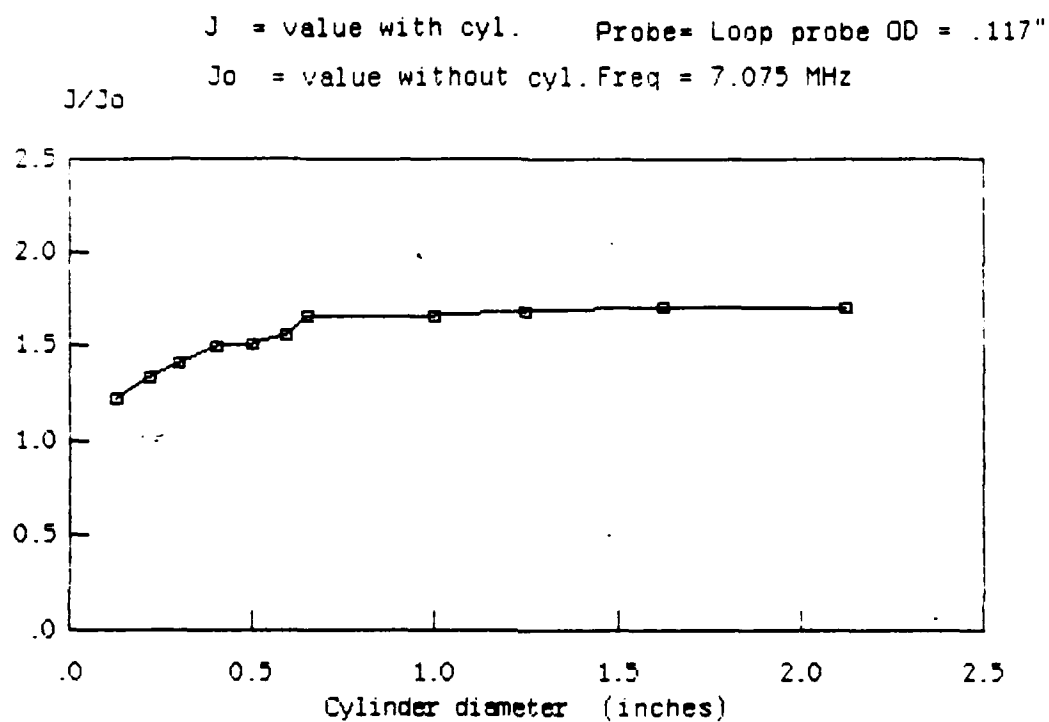
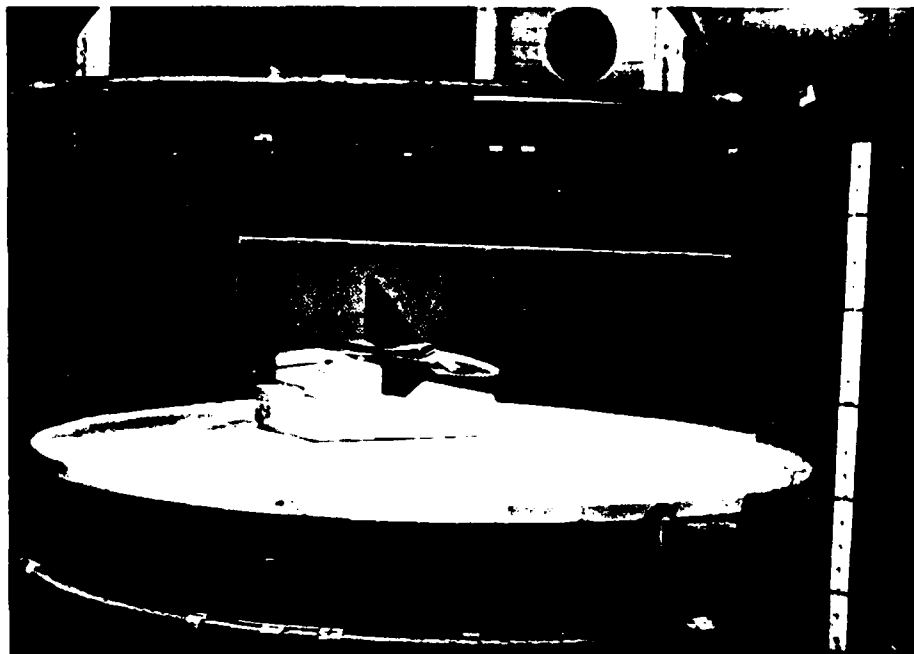


Fig. 5.1: Measured currents on 12 inch long cylinders.

model aircraft. This was the same 1/48 scale model used in 2-100 MHz (full scale) response measurements. With the present facility we are able to provide data in the 20 KHz to 0.52 MHz range using 1 to 25 MHz measurement range.

These measurements were performed with a 25 watt (1-500 MHz) power amplifier added on the (coil) driver side and a 25 dB low noise amplifier (1-500 MHz) introduced between the probe and vector voltmeter. Also, the signal generator was replaced by a synthesized source to assure accurate repeatability of the drive signal frequency and the power level. Measurements were performed by manually punching in the desired frequencies and reading the probe voltages off the meter. This modified set-up did not alleviate the problem of signal coupling through the cables and connectors but, in fact, made it worse due to the added amplifiers and cables. We then observed that the signal that couples through the cables remains essentially invariant as long as the cables are undisturbed. The polarity of the probe signal, however, depends on the orientation of the loop. Thus, if two measurements are made, one with the loop oriented in a certain way and the other with the loop rotated 180 degrees, then the difference between the two recordings yields mainly the signal picked up by the loop and most of the undesired signals are cancelled out. This was then the procedure used during the measurements with F-106B model. Figure 5.2 shows photographs of the model in the facility set up to measure axial fuselage current on top of the fuselage. The top photograph shows the model, the two coils supported on plywood rings, and the aluminum plates. The probe lead comes radially outward, which then is taped to one of the plates (not shown). The lower photograph in the figure shows a close-up of the model.





(a) Facility and the model.



(b) Close-up of the model.

Fig. 5.2: F-106 model set up for measurement.

Figures 5.3 to 5.8 show the data obtained for the following three cases that were also used in previous anechoic chamber measurements [9]:

- (i) Top Inc., E-parl fus, STA:F481R,  $J_a$ ; Figs. 5.3 and 5.4
- (ii) Top Inc., E-perp fus, STA:WL104B,  $J_a$ ; Figs. 5.5 and 5.6
- (iii) Top Inc., E-perp fus, STA:F4816,  $J_c$ ; Figs. 5.7 and 5.8

In each of the above three cases, the data are at first presented for the entire frequency range 0-100 MHz and there the magnetostatic result appears as a dot at zero frequency. In the following plot the data are then shown in the frequency range 0 to 3 MHz where the magnetostatic measurements are clearly seen. On looking at the measurements presented it is found that the magnetostatic results still have as much as 1 dB ripple in amplitude and  $15^\circ$  ripple in phase. By developing better measurement procedures, for example, improving the shielding in cables and connectors, and in particular, placing the voltmeter and signal amplifier in a shielded enclosure, these ripples could be reduced to about 0.25 dB and 3 degrees, respectively.

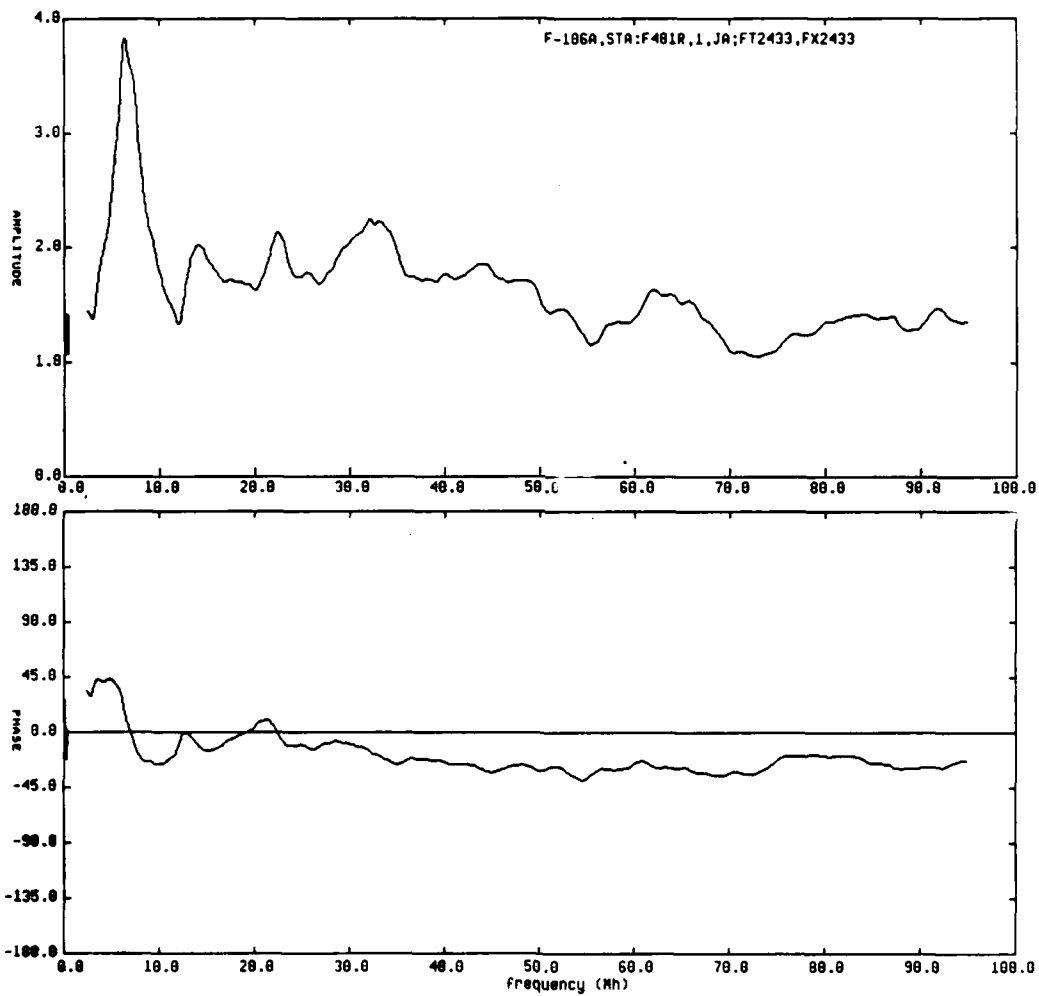


Fig. 5.3: Axial surface field on F-106, top incidence, E-parallel to fuselage, STA: F481R.

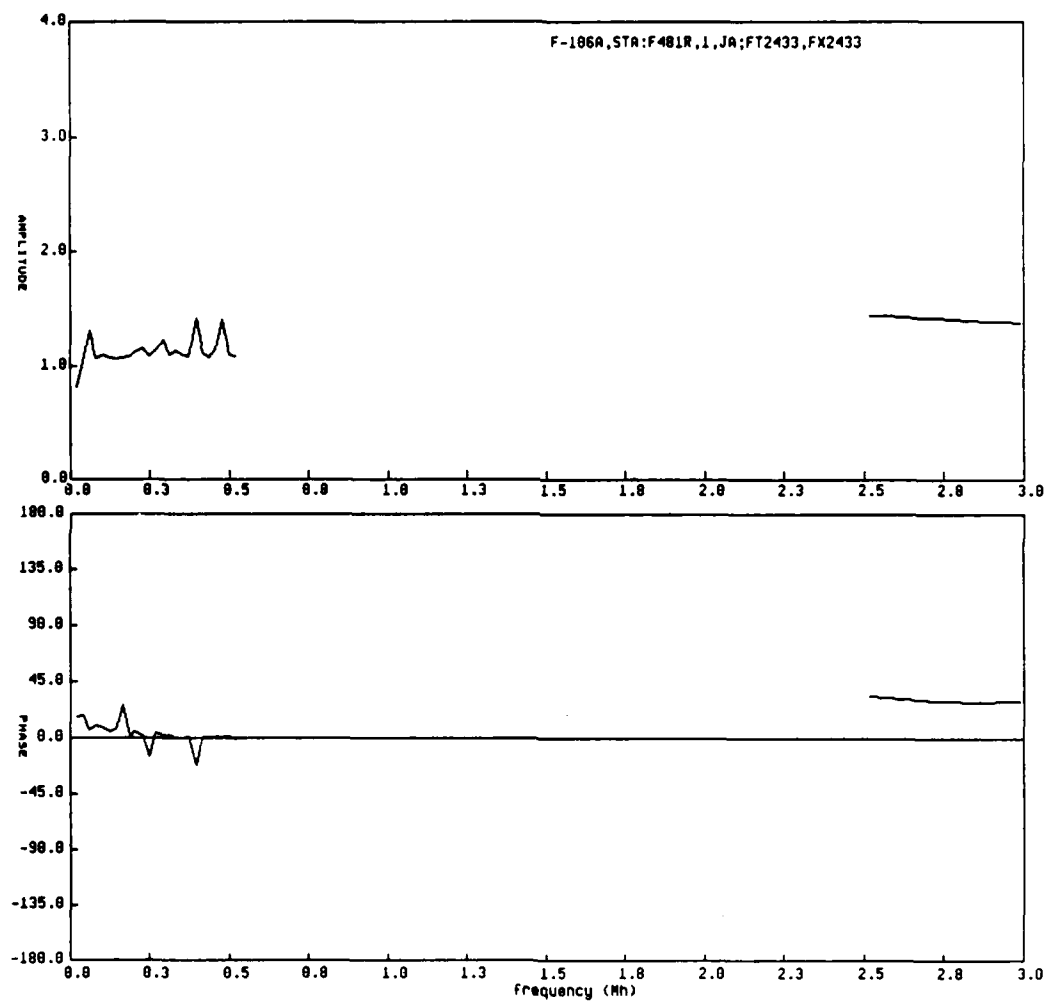


Fig. 5.4: Figure 5.3 expanded to show magnetostatic data.

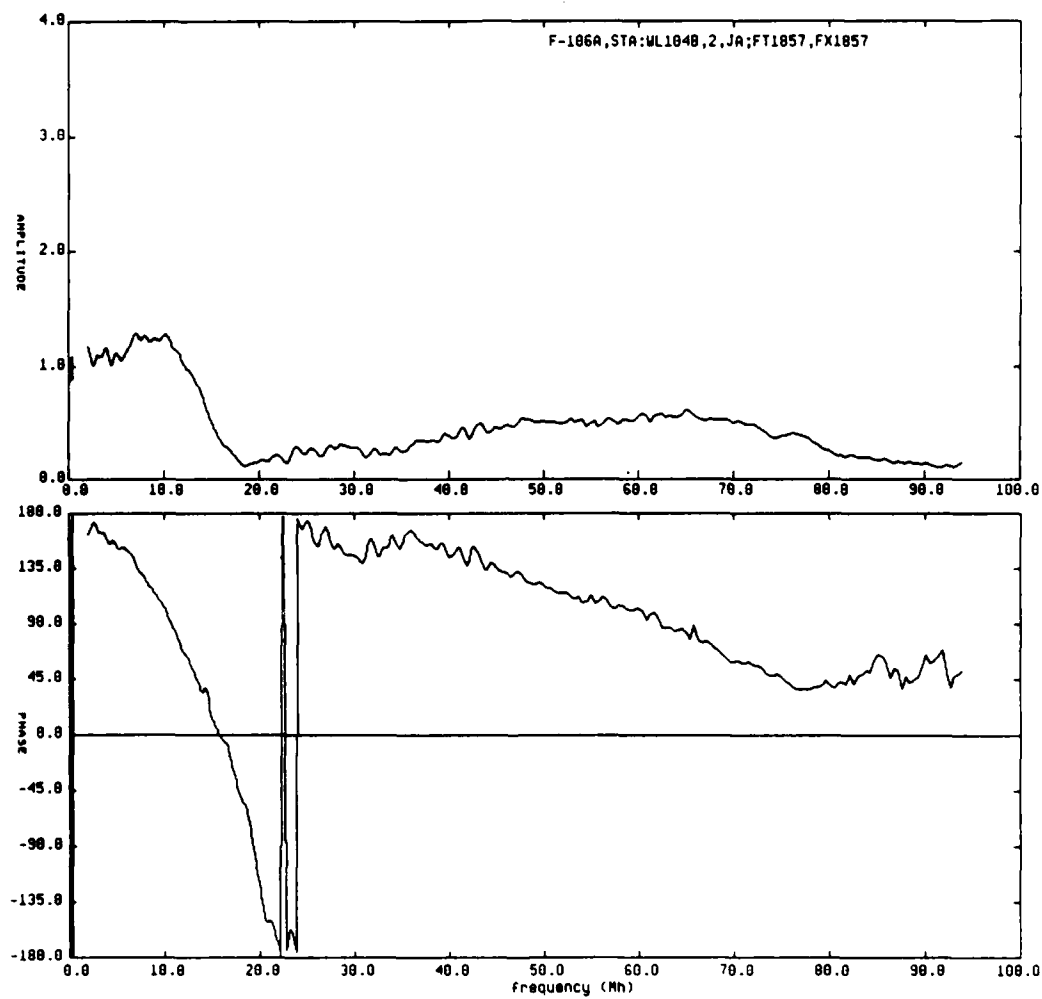


Fig. 5.5: Axial surface field on F-106, top incidence, E- perpendicular to fuselage, STA: WL104B.

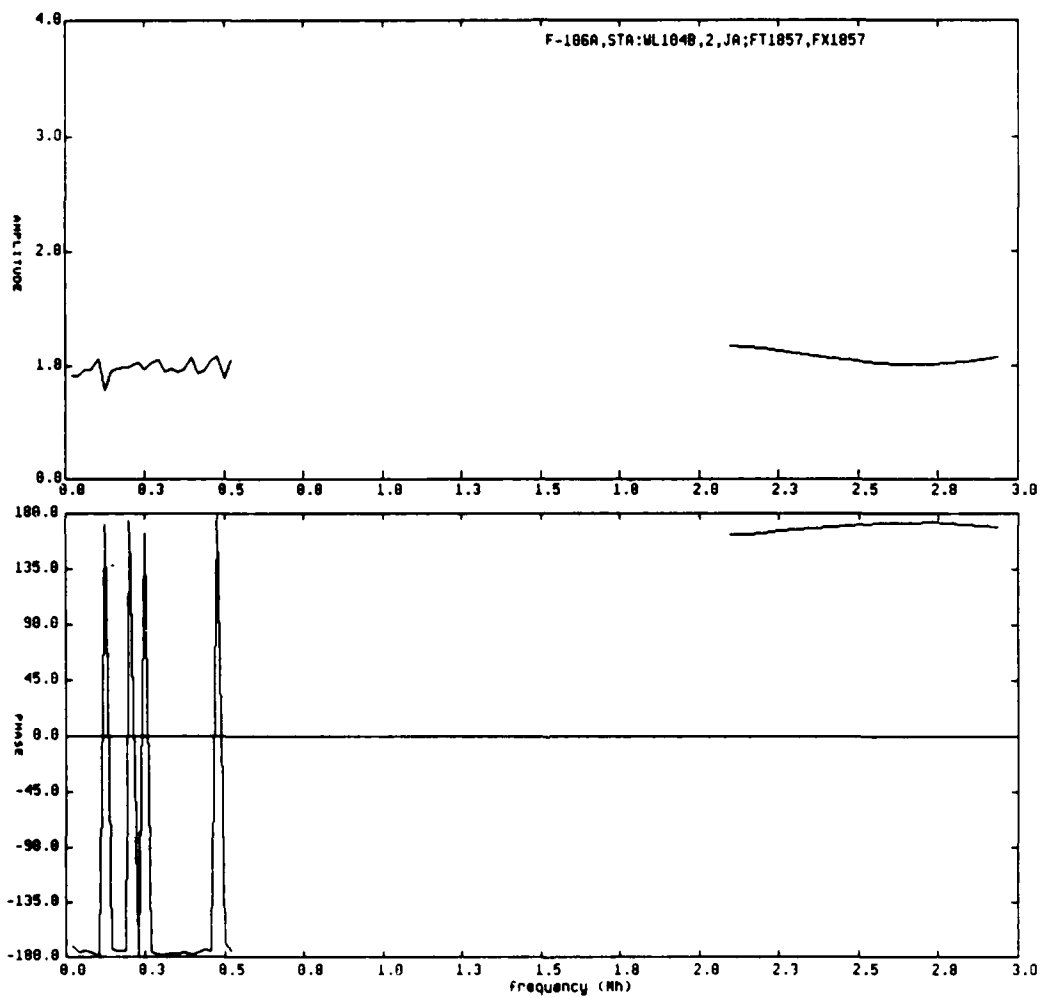


Fig. 5.6: Figure 5.5 expanded to show magnetostatic data.

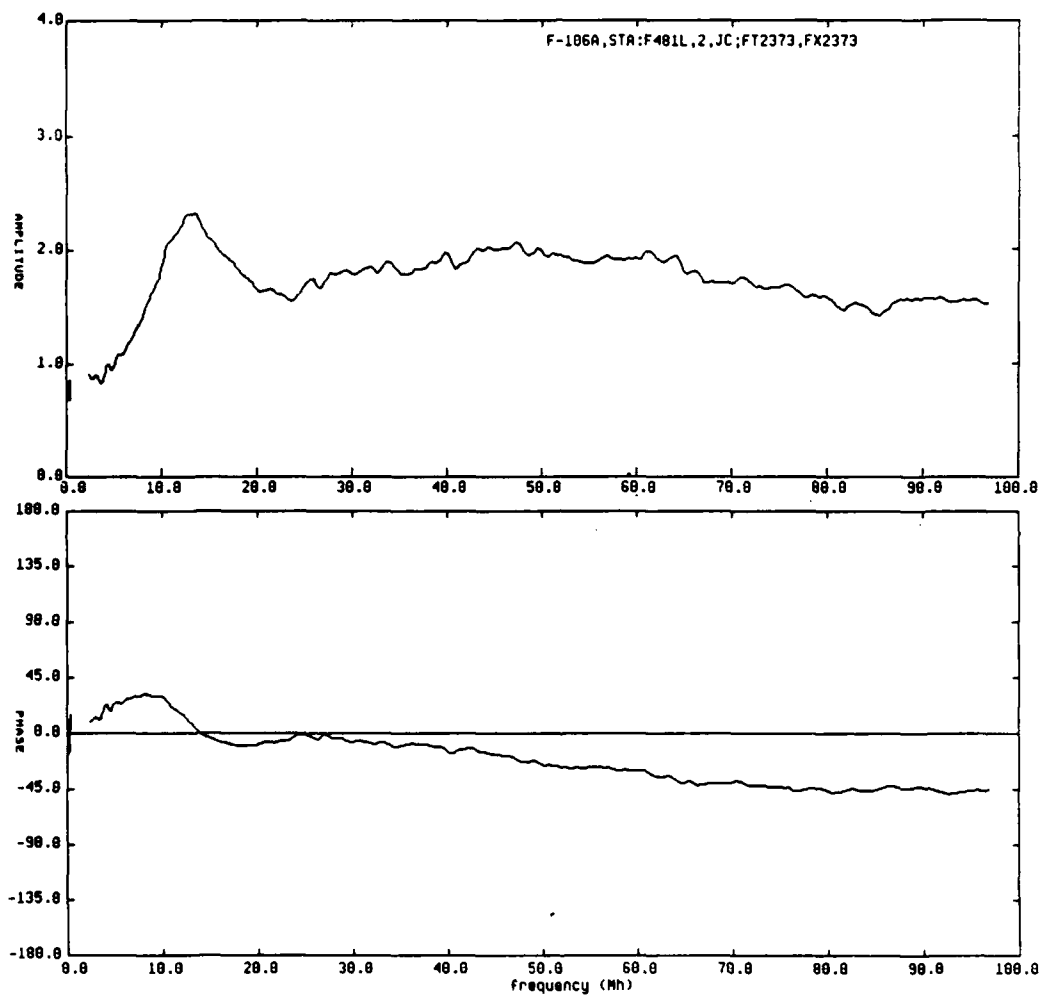


Fig. 5.7: Circumferential current on F-106, top incidence, E-perpendicular to the fuselage, STA: F481L.

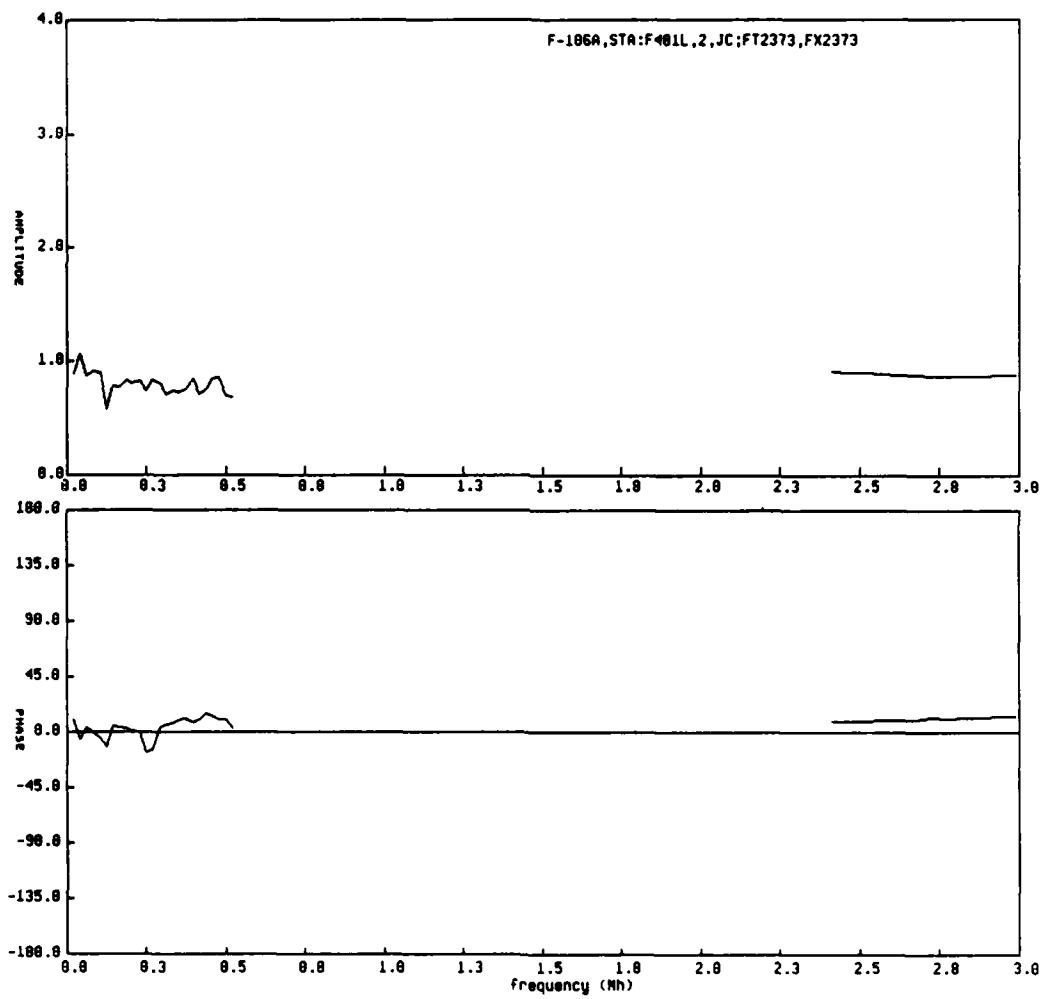


Fig. 5.8: Figure 5.7 expanded to show magnetostatic data.



## 6. CONCLUSIONS

The purpose of the present program was to develop an experimental facility to measure the induced surface fields on relatively small models or objects at frequencies below the lowest frequency limits of anechoic chambers. At these low frequencies the magnetic fields (surface currents) and electric fields (surface charges) are independent, and, hence, in practice these can be measured independently in two different types of facilities, e.g., magnetostatic and (quasi) electrostatic.

The present program was concerned with the development of a magnetostatic facility. To this end, we conducted theoretical studies relating to the design of the facility, and analyzed the responses of perfectly and imperfectly conducting canonical models placed in the facility.

The design, construction and testing of two configurations, the Plywood Facility and the Aluminum Facility, were carried out. The one that was selected and implemented was the Aluminum Facility, which met or exceeded most of the design goals. The final dimensions of the required Helmholtz coils were based on theoretical computations to obtain a cylindrical working volume of two feet in diameter and two feet in height having  $\pm 5$  percent maximum deviation from the field at the center. For the Aluminum Facility, field mapping measurements were performed at 7.875, 10.000 and 15.000 MHz to demonstrate the performance of the facility. Although working volume obtained from these measurements met the design goal, the data indicate that the

volume is more like spherical (two feet diameter) rather than cylindrical.

No evaluation tests were performed above 15 MHz, but it is believed that the facility can be used at frequencies up to 30 MHz, perhaps 50 MHz. In the original guidelines of the program the intent was to operate the facility at 10 MHz, but by using broadband components we have demonstrated its capability through the range of frequencies of at least 1-25 MHz by making sample measurements on F-106B model aircraft.

To provide a complete set of low frequency electromagnetic response data for a given model, it is suggested that the magnetostatic facility be complemented by a (quasi) electrostatic facility capable of measuring induced surface charges on the model. Theoretical, yet practical, designs have been considered for such a facility which would be similar in size to the magnetostatic one, but with the Helmholtz coils replaced by conductive spherical shells of comparable dimension.

## 7. REFERENCES

- [1] Lee, K.S.H. (ed.), (1980), "EMP Interaction: Principles, Techniques and Reference Data," AFWL-TR-80-402, pp. 267-276.
- [2] Stratton, J.A.(1941), "Electromagnetic Theory," McGraw-Hill Book Co., Inc., New York, p. 263.
- [3] Scott, W.T.(1960), "The Physics of Electricity and Magnitism," John Wiley & Sons, Inc., New York, p. 281.
- [4] Smythe, W.R.(1950), "Static and Dynamic Electricity," McGraw-Hill Book Co., Inc., New York, pp. 270-271.
- [5] Van Bladel, J.(1964), "Electromagnetic Fields," McGraw-Hill Book Co., Inc., New York, pp. 155-156.
- [6] Dwight, H.B.(1961), "Tables of Integrals and Other Mathematical Data," The Macmillan Company, New York, pp. 180-186.
- [7] Jahnke E, and F. Emde(1945), "Tables of Functions," Dover Publication.
- [8] Baum, C.E.(1985), Private Communications, AFWL.
- [9] Liepa, V.V., and S.T. Pennock(1984), "Exterior Response of NASA F-106 Aircraft," AFWL Interaction Application Memo 41.

APPENDIX A  
ADDITIONAL DETAILS FOR SECTION 2.1

A.1 Derivation of Eqs. (2.9) and (2.10)

In this Appendix we show the derivation of the approximate expressions (2.9) and (2.10) for  $H_r$  and  $H_z$  from the corresponding exact expressions (2.7) and (2.8) which are rewritten as follows:

$$H_r = \frac{I}{2\pi} \frac{z}{r[(a+r)^2 + z^2]^{1/2}} \left[ -K + \frac{a^2 + r^2 + z^2}{(a-r)^2 + z^2} E \right] \quad (A.1)$$

$$H_z = \frac{I}{2\pi} \frac{1}{[(a+r)^2 + z^2]^{1/2}} \left[ K + \frac{a^2 - r^2 - z^2}{(a-r)^2 + z^2} E \right] , \quad (A.2)$$

where

$$k^2 = \frac{4ar}{(a+r)^2 + z^2} , \quad (A.3)$$

and  $K$  and  $E$  are defined in (2.4) and (2.5). Note that (A.3) indicates  $k \rightarrow 0$  as  $r \rightarrow 0$ , for all  $z$  since  $a \neq 0$ , and  $k^2 < 1$  for  $r \neq 0$  and for all  $z$ .

We shall make use of the following known expansions of  $K$  and  $E$  (see [6]):

$$K = \frac{\pi}{2} \left[ 1 + \frac{k^2}{4} + \frac{9}{64} k^4 + \frac{25}{256} k^6 \right] , \quad k^2 < 1 \quad (A.4)$$

$$E = \frac{\pi}{2} \left[ 1 - \frac{k^2}{4} - \frac{3}{64} k^4 - \frac{5}{256} k^6 \right] , \quad k^2 < 1 . \quad (A.5)$$

## A.2 Derivation of Eq. (2.9)

To obtain an expression for  $H_r$  near  $r \rightarrow 0$  we rewrite (A.1) as:

$$H_r = \frac{I}{2\pi} \frac{z}{r[(a+r)^2 + z^2]^{1/2}} \left[ -K + \frac{1 - \frac{1}{2} k^2}{1 - k^2} E \right]. \quad (A.6)$$

Expanding  $(1 - k^2/2)/(1 - k^2)$  as a power series in  $k^2$ , and using (A.4) and (A.5) it can be shown that

$$-K + \frac{1 - \frac{1}{2} k^2}{1 - k^2} E = \frac{\pi}{2} \cdot \frac{3}{16} k^4 + O(k^6).$$

Now substituting (A.7) in (A.6) we obtain

$$H_r \approx \frac{3Ia^2}{4} \frac{zr}{[(a+r)^2 + z^2]^{5/2}} + O(r^2)$$

## A.3 Derivation of Eq. (2.10)

The expression for  $H_z$  near  $r \rightarrow 0$  is obtained from the Taylor's series expansion (A.2) expressed as:

$$H_z \approx H_z \Big|_{r=0} + r \frac{\partial H_z}{\partial r} \Big|_{r=0} + \frac{r^2}{2} \frac{\partial^2 H_z}{\partial r^2} \Big|_{r=0} + O(r^3), \quad (A.9)$$

where  $H_z$  and its derivatives on the right-hand side are obtained from (A.2) as discussed below.

Using (A.4) and (A.5) it is simple to show from (A.2) that

$$H_z|_{r=0} = \frac{Ia^2}{2} \frac{1}{(a^2 + z^2)^{3/2}} \quad (A.10)$$

To obtain the remaining terms on the right-hand side of (A.9) we need the following relationship obtained from (A.3):

$$\frac{\partial k}{\partial r} = \frac{k}{2r} - \frac{k^3}{4r} - \frac{k^3}{4a} \quad (A.11)$$

and the following derivatives of K and E functions at  $r = 0$  obtained from (A.4) and (A.5) in conjunction with (A.11):

$$\frac{\partial K}{\partial r} = \frac{\pi}{2} \frac{a}{a^2 + z^2}$$

$$\frac{\partial E}{\partial r} = -\frac{\pi}{2} \frac{a}{a^2 + z^2}$$

(A.12)

$$\frac{\partial^2 K}{\partial r^2} = \frac{\pi}{2} \frac{1}{2} \frac{a^2}{(a^2 + z^2)^2}$$

$$\frac{\partial^2 E}{\partial r^2} = \frac{\pi}{2} \frac{5}{2} \frac{a^2}{(a^2 + z^2)^2}$$

After differentiation of (A.3) and using the appropriate relations in (A.12) it can be shown after considerable algebraic manipulation that:

$$\left. \frac{\partial H_z}{\partial r} \right|_{r=0} = 0$$

$$\left. \frac{\partial^2 H_z}{\partial r^2} \right|_{r=0} = \frac{I a^2}{2} \frac{1}{(a^2 + z^2)^{3/2}} - \frac{3}{2} \frac{a^2 - 4z^2}{(a^2 + z^2)^2}$$

(A.13)

Now, introducing (A.13) into (A.9), we obtain

$$H_z = \frac{I a^2}{2} \frac{1}{(a^2 + z^2)^{3/2}} \left[ 1 + \frac{3}{4} \frac{a^2 - 4z^2}{(a^2 + z^2)^2} r^2 + O(r^4) \right] \quad (A.14)$$

which is the required equation (2.10).

#### A.4 The Computer Program

The following is a listing of a program (entitled SQ81: HELMITER) for computing the fields within the Helmholtz coil geometry and based on Eqs. (2.26) and (2.27).

```

1      IMPLICIT REAL*8 (A-H,J-Z)
2      INTEGER*4 I,M,N
3      FZ(I)=Z+I-1.5
4      K(I)=DSQRT(4*R/((R+1)**2+FZ(I)**2))
5      PREF(I)=5.*DSQRT(5.00)/16./PI/DSQRT((R+1)**2+FZ(I)**2)
6      ELINTE(I)=(I-1)*ELIPE2+(2-I)*ELIPE1
7      ELINTK(I)=(I-1)*ELIPK2+(2-I)*ELIPK1
8      HR(I)=PREF(I)*FZ(I)/R*(-ELINTK(I)+(1+R*R+FZ(I)**2)/
9      2      ((R-1)**2+FZ(I)**2)*ELINTE(I))
10     HZ(I)=PREF(I)*(ELINTK(I)+(1-R*R-FZ(I)**2)/
11     2      ((R-1)**2+FZ(I)**2)*ELINTE(I))
12     FI=3.141592653589793238D0
13     1  WRITE(6,11)
14     11  FORMAT(' ENTER: R1,Z1,R2,Z2,N,RI1,ZI1,RI2,ZI2,M.')
15     READ(5,12)R1,Z1,R2,Z2,N,RI1,ZI1,RI2,ZI2,M
16     12  FORMAT(2(4F10.5,I5))
17     WRITE(6,13)
18     13  FORMAT('-',9X,'R/A',12X,'Z/A',15X,'HR/H0',16X,'HZ/H0'/)
19     IF(N.LE.1)N=1
20     IF(M.LE.1)M=1
21     ZINC=0
22     ZIINC=0
23     RINC=0
24     RIINC=0
25     IF(N.EQ.1)GOTO21
26     ZINC=(Z2-Z1)/(N-1)
27     RINC=(R2-R1)/(N-1)
28     21  IF(M.EQ.1)GOTO22
29     ZIINC=(ZI2-ZI1)/(M-1)
30     RIINC=(RI2-RI1)/(M-1)
31     22  Z1=Z1+ZI1
32     R1=R1+RI1
33     DO 102 I2=1,M
34     Z=Z1
35     R=R1
36     DO 101 I1=1,N
37     IF (R.LE.1.D-20)R=1.D-20
38     ELIPE1=DELIE1(K(1))
39     ELIPE2=DELIE1(K(2))
40     ELIPK1=DELIK1(K(1))
41     ELIPK2=DELIK1(K(2))
42     HRTOT=HR(1)+HR(2)
43     HZTOT=HZ(1)+HZ(2)
44     WRITE(6,14)R,Z,HRTOT,HZTOT
45     14  FORMAT(2F15.6,2F21.10)
46     Z=Z+ZINC
47     101  R=R+RINC
48     Z1=Z1+ZIINC
49     102  R1=R1+RIINC
50     WRITE(6,15)
51     15  FORMAT('////')
52     STOP
53     END

```



## APPEXDIX B

### MAGNETOSTATIC FIELDS NEAR A CONDUCTING BODY

The formulation and sample computations of the magnetostatic fields on and near a perfectly conducting sphere and a prolate spheroid are presented. In the static and quasi-static regimes a prolate spheroid could be used to approximate, for example, an aircraft fuselage. Giri and Sands [B.1] have used somewhat simplified expressions to predict the interaction errors for the frontal region of the NASA F-106. Because the errors they predict depend on the particular model chosen to represent the aircraft, plus the fact that the scale model measurements show that most of the interaction errors occur in aircraft resonance regions where quasi-static representations are invalid, we have chosen not to pursue the generation of data that would have questionable relevance to the problem. Instead, we present here rather general magnetostatic analyses for the sphere and the prolate spheroid.

#### B.1 Sphere

For a sphere of radius  $a$  illuminated by the plane wave

$$\vec{E}^i = \hat{x} e^{-ikz}, \quad \vec{H}^i = -\hat{y} e^{-ikz}$$

the exact (dynamic) solution is available in the form of a Mie series. From Bowman et al [B.2], the total (incident plus scattered) magnetic field components are

$$\begin{aligned}
H_r^t &= -i \frac{Y \sin \phi}{(kr)^2} \sum_{n=1}^{\infty} (-i)^n (2n+1) [\psi_n(kr) - a_n \xi_n^{(1)}(kr)] P_n^1(\cos \theta) , \\
H_{\theta}^t &= -\frac{Y \sin \phi}{kr} \sum_{n=1}^{\infty} (-i)^n \frac{2n+1}{n(n+1)} \left[ \{\psi_n(kr) - b_n \xi_n^{(1)}(kr)\} \frac{P_n^1(\cos \theta)}{\sin \theta} \right. \\
&\quad \left. + i\{\psi_n'(kr) - a_n \xi_n^{(1)'}(kr)\} \frac{\partial P_n^1(\cos \theta)}{\partial \theta} \right] , \\
H_{\phi}^t &= -\frac{Y \cos \phi}{kr} \sum_{n=1}^{\infty} (-i)^n \frac{2n+1}{n(n+1)} \left[ \{\psi_n(kr) - b_n \xi_n^{(1)}(kr)\} \frac{\partial P_n^1(\cos \theta)}{\partial \theta} \right. \\
&\quad \left. + i\{\psi_n'(kr) - a_n \xi_n^{(1)'}(kr)\} \frac{P_n^1(\cos \theta)}{\sin \theta} \right]
\end{aligned}$$

where a time factor  $e^{-i\omega t}$  has been assumed and suppressed. The notation is defined in the above reference.

To the leading order in  $k$  only the terms corresponding to  $n = 1$  contribute. Since

$$a_1 = \frac{i}{3} (ka)^3 \{1 + O[(ka)^2]\} , \quad b_1 = -\frac{2i}{3} (ka)^3 \{1 + O[(ka)^2]\} ,$$

$$\psi_1(kr) = \frac{1}{3} (kr)^2 \{1 + O[(kr)^2]\} , \quad \psi_1'(kr) = \frac{2}{3} kr \{1 + O[(kr)^2]\} ,$$

$$\xi_1^{(1)}(kr) = -\frac{i}{kr} \{1 + O[(kr)^2]\} , \quad \xi_1^{(1)'}(kr) = \frac{i}{(kr)^2} \{1 + O[(kr)^2]\}$$

the magnetostatic field components are

$$H_r^t = -Y \sin \theta \sin : \left\{ 1 - \left( \frac{a}{r} \right)^3 \right\}$$

$$H_{\theta}^t = -Y \cos \theta \sin : \left\{ 1 + \frac{1}{2} \left( \frac{a}{r} \right)^3 \right\}$$

$$H_z^t = -Y \cos : \left\{ 1 + \frac{1}{2} \left( \frac{a}{r} \right)^3 \right\} ,$$

and thus

$$\frac{H_r^t}{H_{\theta}^t} = 1 - \left( \frac{a}{r} \right)^3 \quad (B.1)$$

$$\frac{H_{\theta}^t}{H_z^t} = \frac{H_{\theta}^t}{H_{\theta}^t} = 1 + \frac{1}{2} \left( \frac{a}{r} \right)^3 . \quad (B.2)$$

These are, of course, independent of the direction of incidence of the original plane wave, and the normalized tangential components are equal to 3/2 on the surface whereas the radial component is zero there.

## B.2 Prolate Spheroid

It is now simpler to obtain the magnetostatic fields directly rather than as the limit of a dynamic solution.

In terms of the prolate spheroidal coordinates  $\xi, \eta, \psi$  where

$$x = d[(\xi^2 - 1)(1 - \eta^2)]^{1/2} \cos \psi, \quad y = d[(\xi^2 - 1)(1 - \eta^2)]^{1/2} \sin \psi, \\ z = d\xi\eta$$

with  $1 \leq \xi < \infty$ ,  $-1 \leq \eta \leq 1$  and  $0 \leq \psi < 2\pi$ , the spheroid is defined as the surface  $\xi = \xi_0$ . As evident from these relations, the  $z$  axis is the axis of rotation and  $d$  is the semi-interfocal distance. The length to width ratio of the spheroid is

$$\frac{z}{w} = \left\{ 1 - \xi_0^{-2} \right\}^{-1/2}$$

and ranges from  $\infty$  for a long thin spheroid or needle to 1 for a sphere. The corresponding values of  $\xi_0$  are 1 and  $\infty$  respectively.

(i) If

$$\bar{H}^i = \hat{x} = -\nabla \psi^i,$$

the incident magnetostatic potential is

$$\psi^i = -x = -dP_1^1(\xi)P_1^1(\eta)\cos\phi.$$

We seek a scattered magnetostatic field  $\bar{H}^s = -\nabla \psi^s$  where  $\psi^s$  is an exterior potential satisfying the boundary condition

$$\frac{\partial}{\partial n} (\psi^i + \psi^s) = 0$$

on the surface. Since

$$\frac{\partial}{\partial n} = \frac{1}{d} \left( \frac{\xi^2 - 1}{1 - \eta^2} \right)^{1/2} \frac{\partial}{\partial \xi}$$

we are led to choose

$$\psi^s = dAQ_1^1(\xi)P_1^1(\eta)\cos\phi$$

and application of the boundary condition then gives

$$A = \frac{P_1^{1'}(\xi_0)}{Q_1^{1'}(\xi_0)}.$$

Hence

$$\bar{H}^t = \bar{H}^i + \bar{H}^S = -d\gamma \left\{ \left[ p_1^1(\xi) - \frac{p_1^{1'}(\xi_0)}{Q_1^{1'}(\xi_0)} Q_1^1(\xi) \right] p_1^1(\eta) \cos \phi \right\},$$

and in particular

$$H_{\xi}^t = - \left( \frac{\xi^2 - 1}{\xi^2 - \eta^2} \right)^{1/2} \left\{ p_1^1(\xi) - \frac{p_1^{1'}(\xi_0)}{Q_1^{1'}(\xi_0)} Q_1^1(\xi) \right\} p_1^1(\eta) \cos \phi$$

$$H_{\eta}^t = - \left( \frac{1 - \eta^2}{\xi^2 - \eta^2} \right)^{1/2} \left\{ p_1^1(\xi) - \frac{p_1^{1'}(\xi_0)}{Q_1^{1'}(\xi_0)} Q_1^1(\xi) \right\} p_1^1(\eta) \cos \phi$$

$$H_{\phi}^t = \{(\xi^2 - 1)(1 - \eta^2)\}^{-1/2} \left\{ p_1^1(\xi) - \frac{p_1^{1'}(\xi_0)}{Q_1^{1'}(\xi_0)} Q_1^1(\xi) \right\} p_1^1(\eta) \sin \phi$$

implying

$$\frac{H_{\xi}^t}{H_{\xi}^i} = 1 - \frac{p_1^{1'}(\xi_0)}{Q_1^{1'}(\xi_0)} \frac{Q_1^1(\xi)}{p_1^1(\xi)}$$

$$\frac{H_{\eta}^t}{H_{\eta}^i} = \frac{H_{\phi}^t}{H_{\phi}^i} = 1 - \frac{p_1^{1'}(\xi_0)}{Q_1^{1'}(\xi_0)} \frac{Q_1^1(\xi)}{p_1^1(\xi)}.$$

In terms of the shape factor  $q$  [B.3] where  $q$  varies monotonically from 2/3 for a sphere to 1 for a needle,

$$\frac{Q_1^1(\xi)}{P_1^1(\xi)} = \frac{1}{\xi(\xi^2 - 1)} \left\{ \frac{1}{2} \xi(\xi^2 - 1) \ln \frac{\xi + 1}{\xi - 1} - \xi^2 \right\} = - \frac{q(\xi)}{\xi(\xi^2 - 1)} ,$$

$$\frac{Q_1^{1'}(\xi)}{P_1^{1'}(\xi)} = \frac{1}{\xi(\xi^2 - 1)} \left\{ \frac{1}{2} \xi(\xi^2 - 1) \ln \frac{\xi + 1}{\xi - 1} - \xi^2 + 2 \right\} = - \frac{q(\xi) - 2}{\xi(\xi^2 - 1)} ,$$

so that

$$\frac{H_\xi^t}{H_\xi^i} = 1 - \frac{\xi_0(\xi_0^2 - 1)}{q(\xi_0) - 2} \cdot \frac{q(\xi) - 2}{\xi(\xi^2 - 1)} , \quad (B.3)$$

$$\frac{H_\eta^t}{H_\eta^i} = \frac{H_\phi^t}{H_\phi^i} = 1 - \frac{\xi_0(\xi_0^2 - 1)}{q(\xi_0) - 2} \cdot \frac{q(\xi)}{\xi(\xi^2 - 1)} . \quad (B.4)$$

The same results are obtained if  $\bar{H}^i = \hat{y}$ .

(ii) If

$$\bar{H}^i = \hat{z} = -\nabla \psi^i$$

with

$$\psi^i = -z = -dP_1(\xi)P_1(\eta) ,$$

the form assumed for the scattered magnetostatic potential is

$$\psi^S = dA Q_1(\xi) P_1(\eta) ,$$

and application of the boundary condition then gives

$$A = \frac{P_1'(\xi_0)}{Q_1'(\xi_0)} .$$

Hence,

$$H_\phi^t = 0$$

and

$$\frac{H_\xi^t}{H_1^t} = 1 - \frac{P_1'(\xi_0)}{Q_1'(\xi_0)} \frac{Q_1'(\xi)}{P_1'(\xi)} ,$$

$$\frac{H_\eta^t}{H_1^t} = 1 - \frac{P_1'(\xi_0)}{Q_1'(\xi_0)} \frac{Q_1(\xi)}{P_1(\xi)} .$$

In terms of the same shape factor  $q$

$$\frac{Q_1(\xi)}{P_1(\xi)} = \frac{1}{\xi(\xi^2 - 1)} \left\{ \frac{1}{2} \xi(\xi^2 - 1) \ln \frac{\xi + 1}{\xi - 1} - \xi^2 + 1 \right\} = -\frac{q(\xi) - 1}{\xi(\xi^2 - 1)} ,$$

$$\frac{Q_1'(\xi)}{P_1'(\xi)} = \frac{1}{\xi(\xi^2 - 1)} \left\{ \frac{1}{2} \xi(\xi^2 - 1) \ln \frac{\xi + 1}{\xi - 1} - \xi^2 \right\} = -\frac{q(\xi)}{\xi(\xi^2 - 1)} ,$$

so that

$$\frac{H_\xi^t}{H_1^t} = 1 - \frac{\xi_0(\xi_0^2 - 1)}{q(\xi_0)} \cdot \frac{q(\xi)}{\xi(\xi^2 - 1)} , \quad (B.5)$$

$$\frac{H_z^t}{H_z^i} = 1 - \frac{\epsilon_0(\epsilon_0^2 - 1)}{q(\epsilon_0)} \cdot \frac{q(\xi) - 1}{\xi(\xi^2 - 1)}, \quad (\text{B.6})$$

with

$$H_\phi^t = 0.$$

### B.3 Numerical Results

For a sphere any tangential component of the total magnetostatic field when normalized to the corresponding component of the incident field decreases from a value 1.5 at the surface to 1 at large distances, whereas the radial component when similarly normalized increases from 0 at the surface to 1 at large distances. If

$$r = a(1 + \gamma)$$

so that  $\gamma$  is the distance from the surface expressed as a fraction of the radius, (B.1) and (B.2) give

$$\begin{aligned} \Gamma_{\text{nor}} &= \frac{H_z^t}{H_z^i} = 1 - (1 + \gamma)^{-3} \\ \Gamma_{\text{tan}} &= \frac{H_\theta^t}{H_\theta^i} = 1 + \frac{1}{2} (1 + \gamma)^{-3} \end{aligned}$$

and these are illustrated in Fig. B.1. We observed that the percentage reduction in a tangential component below its surface value of 1.5 is approximately the same as  $\gamma$ , i.e. the distance  $r - a$  expressed as a percentage of the radius.

The results for a spheroid are more difficult to express compactly, and since the normalized field components depend on the orientation of



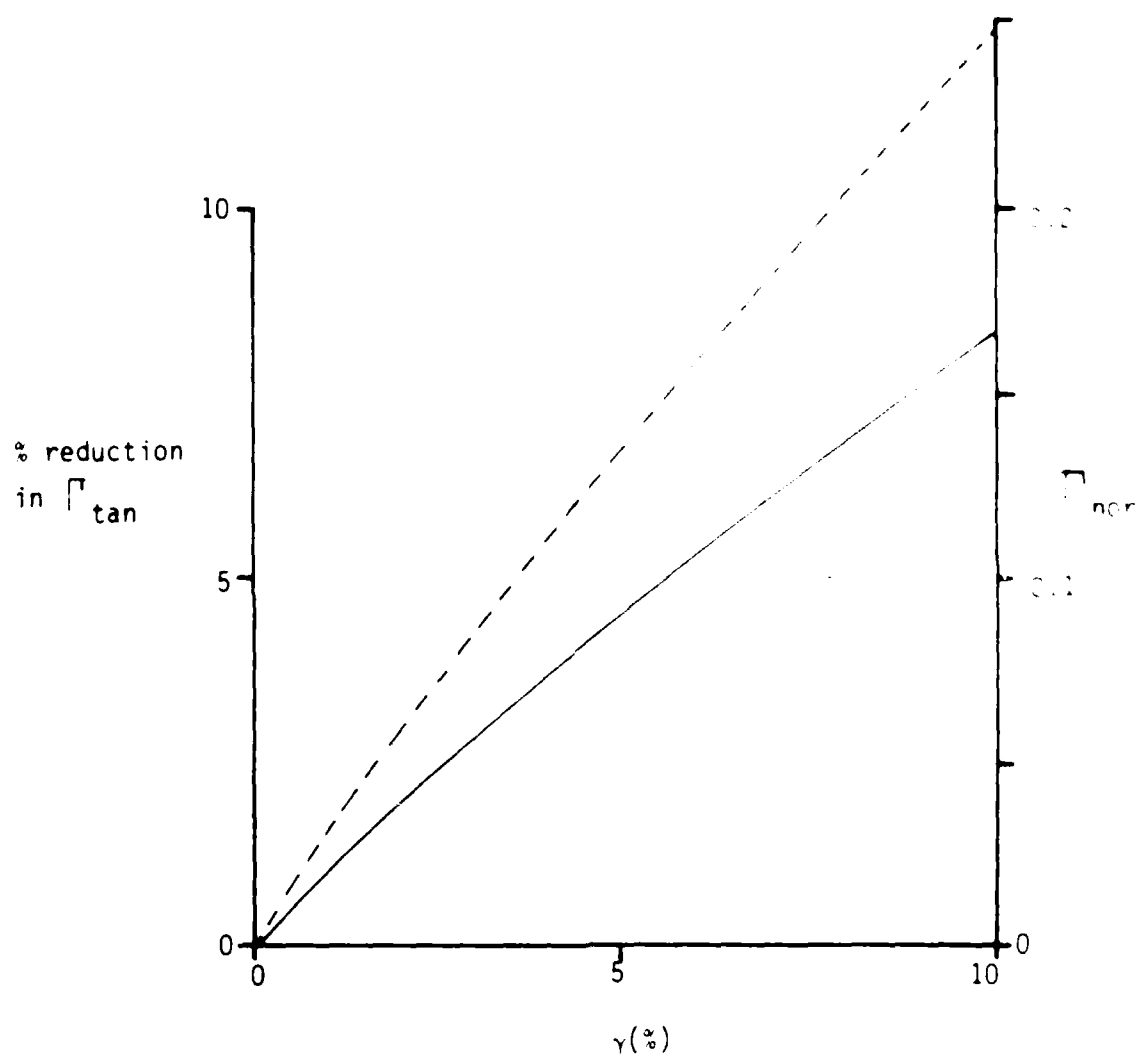


Fig. B.1:  $\Gamma_{nor}$ (---) and percent reduction in  $\Gamma_{tan}$ (—) for a sphere away from the surface.

the spheroid relative to the incident magnetic field, it is convenient to consider separately the cases when  $\vec{H}^i \cdot \hat{z} = 0$  and  $\vec{H}^i \cdot \hat{z} = 1$ . These will be referred to as the perpendicular (or transverse) and parallel orientations respectively. From (B.3) - (B.6) we then have

perpendicular:

$$r_{\text{nor}} = \frac{H_{\xi}^t}{H_{\xi}^i} = 1 - \frac{\xi_0(\xi_0^2 - 1)}{q(\xi_0) - 2} \cdot \frac{q(\xi) - 2}{\xi(\xi^2 - 1)}$$

$$r_{\text{tan}} = \frac{H_{\eta}^t}{H_{\eta}^i} = 1 - \frac{\xi_0(\xi_0^2 - 1)}{q(\xi_0) - 2} \cdot \frac{q(\xi)}{\xi(\xi^2 - 1)}$$

parallel:

$$r_{\text{nor}} = \frac{H_{\xi}^t}{H_{\xi}^i} = 1 - \frac{\xi_0(\xi_0^2 - 1)}{q(\xi_0)} \cdot \frac{q(\xi)}{\xi(\xi^2 - 1)}$$

$$r_{\text{tan}} = \frac{H_{\eta}^t}{H_{\eta}^i} = 1 - \frac{\xi_0(\xi_0^2 - 1)}{q(\xi_0)} \cdot \frac{q(\xi) - 1}{\xi(\xi^2 - 1)}$$

On the surface,  $\xi = \xi_0$  and

$$r_{\text{tan}} = \begin{cases} (1 - q/2)^{-1} & (I) \\ q^{-1} & (II) \end{cases}$$

and these are plotted as functions of the length to width ratio of the spheroid,  $1 \leq \ell/w \leq 10$ , in Fig. B.2.

To show the variation of the normalized fields as a function of the distance away from the surface, we have examined  $r_{\text{nor}}$  and  $r_{\text{tan}}$

NO-A178 258

MAGNETOSTATIC SURFACE FIELD MEASUREMENT FACILITY(U)  
MICHIGAN UNIV ANN ARBOR RADIATION LAB V V LIEPA ET AL.  
DEC 86 AFML-TN-86-29 F29601-82-K-0024

2/2

**UNCLASSIFIED**

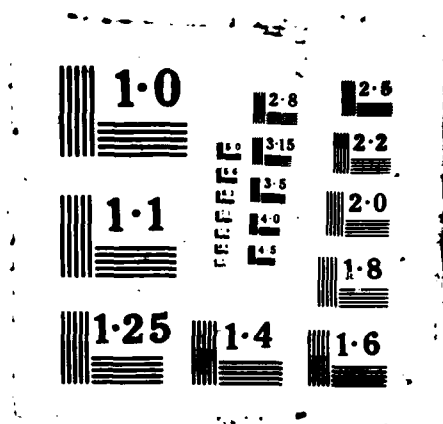
**F/G 14/2**

ML

LND

11. 5.

D11C



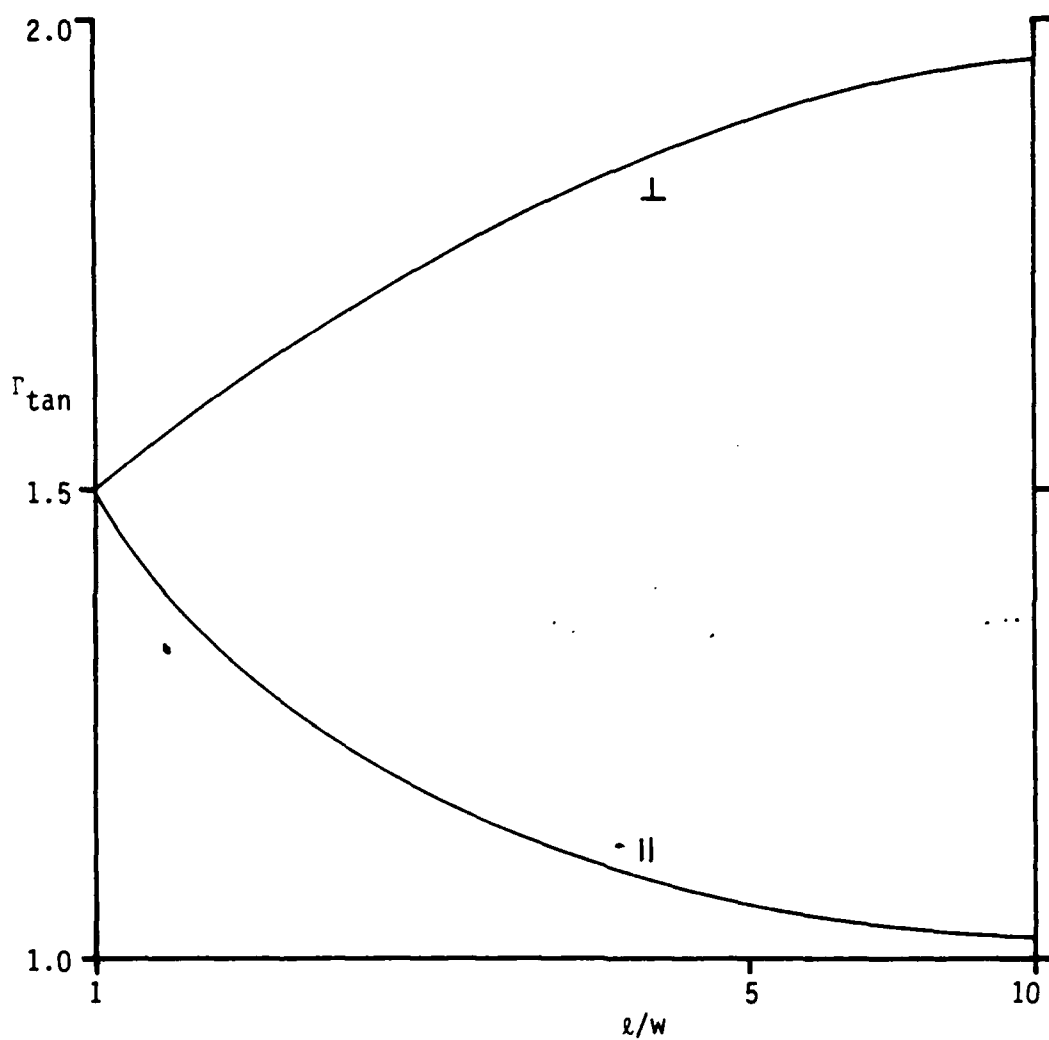


Fig. B.2:  $\Gamma_{\text{tan}}$  on the surface of a prolate spheroid as a function of  $l/w$ .

spheroids having  $\ell/w = 2$  and 5, for which  $\xi_0 = 1.15470$  and 1.02062 respectively. In the plane  $z = 0$  the distance from the surface expressed as a fraction of the semi minor axis is

$$\gamma = \left( \frac{\xi^2 - 1}{\xi_0^2 - 1} \right)^{1/2} - 1$$

and for both spheroids we have computed  $\Gamma_{\text{nor}}$  and  $\Gamma_{\text{tan}}$  as functions of  $\gamma$ ,  $0 \leq \gamma \leq 0.1$ . The results are shown in Figs. B.3 and B.4, and as in the case of the sphere, the results for the tangential components are given as percentage reductions below the surface values. We observe that the increase in  $\Gamma_{\text{nor}}$  away from the surface is almost the same for both orientations of the spheroid, and the rate decreases slightly with increasing  $\ell/w$ . For the tangential components, the percent reduction is almost independent of  $\ell/w$  for the perpendicular orientation, whereas for the parallel orientation the reduction decreases rapidly as  $\ell/w$  increases. Indeed, the decrease is roughly proportional to  $(\ell/w)^2$ . Finally we remark that  $\gamma$  is only a measure of the fractional distance from the surface in the meridional plane  $z = 0$ . As we move round the spheroid towards the tips,  $\gamma$  translates into a smaller physical distance from the surface, and at a tip, the distance is smaller by a factor  $\ell/w$  (approx.) and by a factor  $(\ell/w)^2$  when expressed as a fraction of the same major axis.

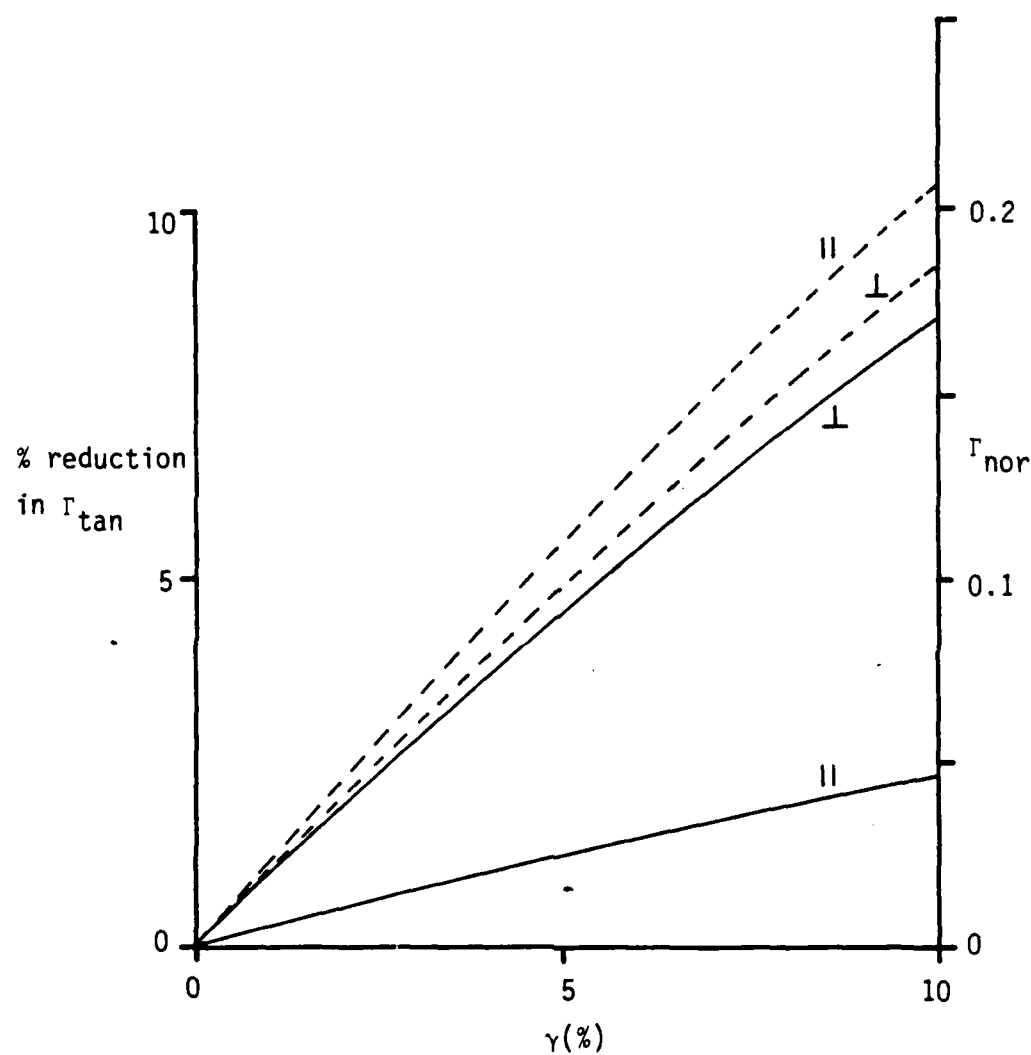


Fig. B.3:  $r_{nor}$  (---) and percent reduction in  $r_{tan}$  (—) for a 2:1 prolate spheroid as functions of distance away from the surface.

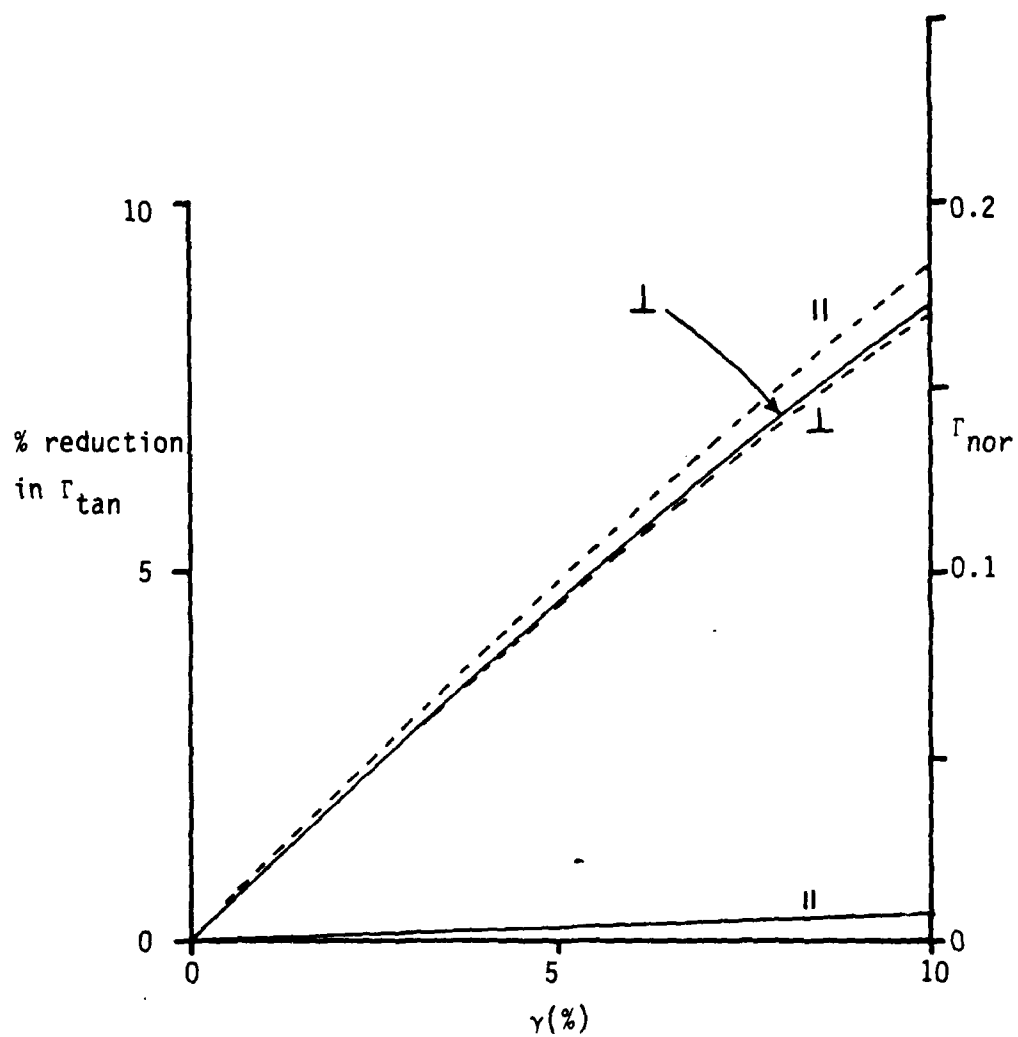


Fig. B.4:  $r_{nor}$  (---) and percent reduction in  $r_{tan}$  (—) for a 5:1 prolate spheroid as functions of distance away from the surface.



#### B.4 References

- [B.1] Giri, D. V. and S. H. Sands (1983), "Design of B-Dot Sensor for the Nose Boom of F-106B Aircraft," AFWL EM Platform Memo 1 and AFWL-TR-83-141.
- [B.2] Bowman, J. J., T.B.A. Senior and P.L.E. Uslenghi (1969), "Electromagnetic and Acoustic Scattering by Simple Shapes," North Holland Pub. Co., Amsterdam, p. 396.
- [B.3] Senior, T.B.A. (1980), "Effect of particle shape on low frequency absorption," Appl. Opt. 19, 2483-2485.

APPENDIX C  
LOW FREQUENCY SURFACE FIELD BEHAVIOR

The main reason for developing a quasi-static measurement facility is to better define the transfer functions at frequencies below those for which the present surface field measurement facility is effective. As the model frequency is decreased below (about) 150 MHz the performance of the anechoic chamber deteriorates to such an extent that, in combination with the approaching cut-off of the illuminating antenna, the measured data for the surface fields (currents and charges) can be significantly in error; and to achieve the same full scale frequencies by using a smaller model would require working with a model that was too small to be conveniently handled, and with a probe that was no longer small compared to the dimensions of the structure on which the fields were measured.

At frequencies for which the model is small compared to the incident wavelength, any surface field quantity  $V$  can be expanded in the form

$$V = A + i\omega B + \omega^2 C + O(\omega^3) \quad (C.1)$$

where  $\omega$  is the circular frequency corresponding to a time convention  $e^{i\omega t}$ , and  $A, B, C$  are real functions of position on the model. If  $A \neq 0$ , then

$$|V| \approx \left| A + \omega^2 \left( C + \frac{1}{2} \frac{B^2}{A} \right) \right| \quad (C.2)$$

for  $\omega$  sufficiently small, and in a neighborhood of  $\omega = 0$  the resulting curve is parabolic: concave up if  $A$  and  $C + 0.5B^2/A$  have the same sign, and concave down if the signs are opposite. If  $A = 0$ ,

$$|V| = |B| \quad (C.3)$$

and the curve is linear, starting from zero. These conclusions are independent of the choice of phase origin.

There are a few simple bodies for which  $A$ ,  $B$ , and  $C$  can be obtained from a knowledge of the exact solution, and others for which they can be found by application of low frequency techniques. It is of interest to examine the results for some examples of the former class.

#### C.1 Acoustically Hard Sphere

For the plane wave

$$v^{inc} = e^{ikz} \quad (C.4)$$

incident on an acoustically hard sphere of radius  $a$ , center at the origin of coordinates, the total field at the surface is [C.1, p. 374]

$$V(\rho) = -\frac{i}{\rho^2} \sum_{n=0}^{\infty} i^n (2n+1) \frac{P_n(\cos \theta)}{h_n^{(2)'}(\rho)} \quad (C.5)$$

where  $\rho = ka$ . Since [C.3]

$$\frac{1}{h_0^{(2)'}(\rho)} = i\rho^2 \left\{ 1 - \frac{1}{2} \rho^2 + o(\rho^3) \right\}$$

$$\frac{1}{h_1^{(2)'}(\rho)} = \frac{i\rho^3}{2} \left\{ 1 + o(\rho^3) \right\}$$

$$\frac{1}{h_2^{(2)'}(\rho)} = \frac{i\rho^4}{9} \left\{ 1 + o(\rho^2) \right\} ,$$

we have

$$\begin{aligned} V(\rho) &= \left[ 1 - \frac{1}{2} \rho^2 \right] P_0(\cos \theta) + \frac{3}{2} i\rho P_1(\cos \theta) - \frac{5}{9} \rho^2 P_2(\cos \theta) + o(\rho^3) \\ &= 1 + \frac{3}{2} i\rho \eta - \frac{2}{9} \rho^2 \left[ 1 + \frac{15}{4} \eta^2 \right] + o(\rho^3) \end{aligned} \quad (C.6)$$

where  $\eta = \cos \theta$ , varying from 1 at the front of the sphere to -1 at the back. Thus

$$C + \frac{1}{2} \frac{B^2}{A} = -\frac{2}{9} + \frac{7}{24} \eta^2 ,$$

and the amplitude curve is concave down for  $29^\circ \leq \theta \leq 151^\circ$ , but concave up otherwise. For a vanishingly small sphere the incident field alone satisfies the boundary condition, and it is therefore logical that  $V(0) = 1$ .

## C.2 Acoustically Hard Prolate

To obtain some feeling for the effect of the body's shape, consider now a prolate spheroid illuminated by the plane wave (C.4) at nose-on incidence. From [C.4] the total field at the surface is

$$V = 2 \sum_{n=0}^{\infty} \frac{(-i)^n}{N_{on}} S_{on}(c, -1) \left\{ R_{on}^{(1)}(c, \xi) - \frac{R_{on}^{(1)'}(c, \xi)}{R_{on}^{(4)'}(c, \xi)} R_{on}^{(4)}(c, \xi) \right\} S_{on}(c, \eta) \quad (C.6)$$

and since [C.2, p. 32]

$$R_{on}^{(1)} R_{on}^{(4)'} - R_{on}^{(1)'} R_{on}^{(4)} = - \frac{i}{c(\xi^2 - 1)},$$

we have

$$V = - \frac{2i}{c(\xi^2 - 1)} \sum_{n=0}^{\infty} \frac{(-i)^n}{N_{on}} S_{on}(c, -1) \frac{S_{on}(c, \eta)}{R_{on}^{(4)'}(c, \xi)} \quad (C.7)$$

where  $c = ka$ ,  $a$  being half the interfocal distance.

Using the expansions in the Appendix of [C.4] it can be shown that

$$R_{00}^{(4)}(c, \xi) = \frac{i}{c} \left\{ \left( 1 + \frac{c^2}{6} \right) Q_0(\xi) - icP_0(\xi) - \frac{c^2}{2} P_1(\xi) - \frac{c^2}{9} Q_2(\xi) + O(c^3) \right\},$$

$$R_{01}^{(4)}(c, \xi) = \frac{3i}{c^2} \left\{ Q_1(\xi) + O(c^2) \right\},$$

$$R_{02}^{(4)}(c, \xi) = -\frac{45}{2c^3} \left\{ Q_2(\xi) + O(c^3) \right\} ,$$

$$S_{00}(c, n) = \left( 1 - \frac{c^2}{18} \right) P_0(n) - \frac{c^2}{9} P_2(n) + O(c^4) ,$$

$$S_{01}(c, n) = \left( 1 - \frac{3}{50} c^2 \right) P_1(n) - \frac{c^2}{25} P_3(n) + O(c^4) ,$$

$$S_{02}(c, n) = P_2(n) + O(c^2) ,$$

and hence

$$V = \frac{1}{(\xi^2 - 1)Q'_0(\xi)} \left\{ \left[ 1 - \frac{5}{18} c^2 + \frac{c^2}{9} \frac{Q'_2(\xi)}{Q'_0(\xi)} + \frac{c^2}{2} \frac{P'_1(\xi)}{Q'_0(\xi)} \right] P_0(n) \right. \\ \left. + ic \frac{Q'_0(\xi)}{Q'_1(\xi)} P_1(n) - \frac{c^2}{9} \left[ 1 + 2 \frac{Q'_0(\xi)}{Q'_2(\xi)} \right] P_2(n) + O(c^3) \right\} .$$

By inserting the expressions for the angular Legendre polynomials in terms of  $n = \cos \theta$  (see, for example, [C.5, p. 608]) and using the facts that

$$P'_1(\xi) = 1 , \quad Q'_0(\xi) = -\frac{1}{\xi^2 - 1} ,$$

we finally obtain

$$V = 1 + icn \frac{Q'_0(\xi)}{Q'_1(\xi)} + \frac{c^2}{18} \left\{ 2 \left[ \frac{Q'_0(\xi)}{Q'_1(\xi)} - 2 + \frac{Q'_0(\xi)}{Q'_2(\xi)} \right] - 9(\xi^2 - 1) \right. \\ \left. - 3n^2 \left[ 1 + 2 \frac{Q'_0(\xi)}{Q'_2(\xi)} \right] \right\} + O(c^3) \quad (C.8)$$

As expected,  $V = 1$  when  $c = 0$ , and the expression reduces to (C.6) when  $\xi \rightarrow \infty$ ,  $c \rightarrow 0$  in such a way that  $c\xi$  tends to the finite value  $ka$ .

Near to the ends of the spheroid when  $n = \pm 1$ , the amplitude curve is always concave up, but as in the case of the sphere there is a range of  $n$  (and hence  $\theta$ ) where the curve changes to concave down, and such a range exists for any spheroid. Thus, for  $\xi = 2$  corresponding to a 1.15:1 spheroid, the curve is concave down for  $26.5^\circ \leq \theta \leq 153.5^\circ$ .

### C.3 Perfectly Conducting Sphere

With a perfectly conducting body the surface field quantities that are measured are the normal component of the electric field (or charge) and the tangential components of the magnetic field (or current). It would be desirable to generate the low frequency expansions of these quantities for a perfectly conducting spheroid and, possibly, for other simple shapes as well, but since this is a non-trivial task, we shall, for the moment at least, confine attention to a sphere.

For a sphere of radius  $a$  illuminated by the incident plane wave

$$\vec{E}^{\text{inc}} = \hat{x} e^{ikz}, \quad Z_0 \vec{H}^{\text{inc}} = -\hat{y} e^{ikz}, \quad (C.9)$$

the non-zero components of the (total) surface field are:

$$E_r = -\cos \vartheta : \frac{1}{\rho} \sum_{n=1}^{\infty} i^n (2n+1) \frac{P_n^1(\cos \vartheta)}{\xi_n^{(2)}(\rho)} \quad (C.10)$$

$$Z_0 H_{\vartheta} = \sin \vartheta : \frac{1}{\rho} \sum_{n=1}^{\infty} i^{n+1} \frac{2n+1}{n(n+1)} \left\{ \frac{1}{\xi_n^{(2)}(\rho)} \frac{P_n^1(\cos \vartheta)}{\sin \vartheta} + \frac{i}{\xi_n^{(2)}(\rho)} \frac{\partial P_n^1(\cos \vartheta)}{\partial \vartheta} \right\} \quad (C.11)$$

$$Z_0 H_{\varphi} = \cos \vartheta : \frac{1}{\rho} \sum_{n=1}^{\infty} i^{n+1} \frac{2n+1}{n(n+1)} \left\{ \frac{1}{\xi_n^{(2)}(\rho)} \frac{\partial P_n^1(\cos \vartheta)}{\partial \vartheta} + \frac{i}{\xi_n^{(2)}(\rho)} \frac{P_n^1(\cos \vartheta)}{\sin \vartheta} \right\} \quad (C.12)$$

where [C.1, pp. 396-397]

$$\xi_n^{(2)}(\rho) = \rho h_n^{(2)}(\rho).$$

Since

$$\xi_1^{(2)}(\rho) = \frac{i}{\rho} \left\{ 1 + \frac{\rho^2}{2} + O(\rho^3) \right\},$$

$$\xi_2^{(2)}(\rho) = \frac{3i}{\rho^2} \left\{ 1 + O(\rho^2) \right\},$$

and

$$\xi_3^{(2)}(\rho) = \frac{15i}{\rho^3} \left\{ 1 + O(\rho^2) \right\},$$



we have

$$\begin{aligned}
 E_r &= -\cos \phi \frac{1}{\rho^2} \left\{ 3i \frac{P_1^1(\cos \theta)}{\xi_1^{(2)'}(\rho)} - 5 \frac{P_1^1(\cos \theta)}{\xi_2^{(2)'}(\rho)} - 7i \frac{P_3^1(\cos \theta)}{\xi_3^{(2)'}(\rho)} + O(\rho^5) \right\} \\
 &= 3 \cos \phi \sin \theta \left\{ 1 + \frac{5}{6} i \rho n + \frac{\rho^2}{90} (52 - 35n^2) + O(\rho^3) \right\}, \quad (C.13)
 \end{aligned}$$

$$\begin{aligned}
 Z_0 H_\theta &= \sin \phi \frac{1}{\rho} \left\{ -\frac{3}{2} \frac{1}{\xi_1^{(2)'}(\rho)} \frac{P_1^1(\cos \theta)}{\sin \theta} - \frac{3i}{2} \frac{1}{\xi_1^{(2)'}(\rho)} \frac{\partial P_1^1(\cos \theta)}{\partial \theta} \right. \\
 &\quad - \frac{5}{6} i \frac{1}{\xi_2^{(2)'}(\rho)} \frac{\partial P_2^1(\cos \theta)}{\sin \theta} + \frac{5}{6} \frac{1}{\xi_2^{(2)'}(\rho)} \frac{\partial P_2^1(\cos \theta)}{\partial \theta} \\
 &\quad \left. + \frac{7}{12} i \frac{1}{\xi_3^{(2)'}(\rho)} \frac{P_3^1(\cos \theta)}{\partial \theta} + O(\rho^4) \right\}, \\
 &= -\frac{3}{2} \sin \phi \left\{ n + \frac{2}{9} i \rho (2 + 5n^2) - \frac{7}{60} \rho^2 n (3 + 5n^2) + O(\rho^3) \right\}, \quad (C.14)
 \end{aligned}$$

and similarly

$$Z_0 H_\phi = -\frac{3}{2} \cos \phi \left\{ 1 + \frac{14}{9} i \rho n - \frac{\rho^2}{60} (11 + 45n^2) + O(\rho^3) \right\}. \quad (C.15)$$

The amplitude curve for  $E_r$  is always concave up. That for  $H_\theta$  is concave up throughout the illuminated region, i.e.,  $0 \leq \theta < 90^\circ$ , and the curve for  $H_\phi$  is concave up except for  $51^\circ \leq \theta \leq 129^\circ$ .

#### C.4 Some Implications

It is anticipated that the quasi-static facility will provide data over a frequency range comparable to or exceeding that for which the above low frequency expansions are valid, and will, in effect, extend the frequency coverage of our present data down to zero. When that facility is in operation, it will be of interest to see if the low frequency data can be adequately approximated using the theoretical values for a simplified structure modeling the surface where the measurement is made.

The main purpose for the facility is to expand the frequency coverage of the measured transfer function data used for EMP extrapolation, but it is possible that low frequency information could also help to determine the lowest (zeroth order) SEM pole. To explore this, consider some transfer function  $F(s)$  where  $s = i\omega$ . At low frequencies,  $F(s)$  can be expanded as

$$F(s) = F(0) + sF'(0) + \frac{s^2}{2} F''(0) + \dots, \quad (C.16)$$

where the coefficients in the series are real functions of position, orientation, etc., as well as of the body itself. The SEM representation of  $F(s)$  is

$$F(s) = \sum_{n=0}^{\infty} \left[ \frac{A_n}{s - s_n} + \frac{A_n^*}{s - s_n^*} \right] \quad (C.17)$$

where the asterisk denotes the complex conjugate and if the poles  $s_n$  are ordered in increasing magnitude, we have, for  $|s| \ll |s_0|$ ,

$$F(s) = \sum_{n=0}^{\infty} \left\{ - \left[ \frac{A_n}{s_n} + \frac{A_n^*}{s_n^*} \right] - s \left[ \frac{A_n}{s_n^2} + \frac{A_n^*}{s_n^{*2}} \right] - s^2 \left[ \frac{A_n}{s_n^3} + \frac{A_n^*}{s_n^{*3}} \right] + \dots \right\}.$$

Thus

$$F(0) = - \frac{A_0}{s_0} \sum_{n=0}^{\infty} \frac{A_n}{A_0} \frac{s_0}{s_n} - \frac{A_0^*}{s_0^*} \sum_{n=0}^{\infty} \frac{A_n^*}{A_0^*} \frac{s_0^*}{s_n^*}$$

$$F'(0) = - \frac{A_0}{s_0^2} \sum_{n=0}^{\infty} \frac{A_n}{A_0} \left( \frac{s_0}{s_n} \right)^2 - \frac{A_0^*}{s_0^{*2}} \sum_{n=0}^{\infty} \frac{A_n^*}{A_0^*} \left( \frac{s_0^*}{s_n^*} \right)^2$$

$$F''(0) = -2 \frac{A_0}{s_0^3} \sum_{n=0}^{\infty} \frac{A_n}{A_0} \left( \frac{s_0}{s_n} \right)^3 - 2 \frac{A_0^*}{s_0^{*3}} \sum_{n=0}^{\infty} \frac{A_n^*}{A_0^*} \left( \frac{s_0^*}{s_n^*} \right)^3$$

and because of the manner in which the poles are ordered, the lowest order one dominates  $F''(0)$  to a greater degree than it does  $F'(0)$  and  $F(0)$ . It is not yet evident that we can make use of this fact in locating the pole.

### C.5 References

- [C.1] Bowman, J. J., T.B.A. Senior and P.L.E. Uslenghi (1969), "Electromagnetic and Acoustic Scattering by Simple Shapes," North-Holland Pub. Co., Amsterdam.
- [C.2] Flammer, C. (1957), "Spheroidal Wave Functions," Stanford University Press, Stanford, CA.
- [C.3] Senior, T.B.A. (1959), "Derivation of the complete Rayleigh series for a sphere," University of Michigan Radiation Laboratory Memorandum 2500-158-M.
- [C.4] Senior, T.B.A. (1960), "Scalar diffraction by a prolate spheroid at low frequencies," Can J. Phys. 38, 1632-1641.
- [C.5] Stratton, J. A. (1941), "Electromagnetic Theory," McGraw-Hill Book Co., Inc., New York.

APPENDIX D  
ANALYSES OF EIGHT-PORT NETWORK

These analyses were performed to predict and optimize the performance of the Plywood Facility (Section 3.1).

D.1 Theoretical Analysis

The analysis of the network is based upon the following assumptions about the driver and coil circuit (see Fig. D.1):

A) Currents  $I$ ,  $I'$  are the same in all eight secondary distribution loops.

B) The mutual inductance on the primary distribution transformer depends only on the relative positioning of each winding on the toroid.

Thus  $M = M_1 + M_2 + \dots + M_7 = M_2 + M_3 + \dots + M_8$ , etc.

C) All real resistances are assumed very small and neglected.

Definition of Symbols:

$M_A$  = mutual inductance between primary and secondary windings on primary distribution transformer.

$M_B$  = mutual inductance between  $L_A$  and  $L_B$

$M_\ell$  = mutual inductance between helmholtz coils

$M$  = mutual inductance between secondary windings on primary distribution transformer

$L_T$  = self inductance of primary

$L_A$  = inductance of secondary

$L_B$  = inductance of primary feed transformer

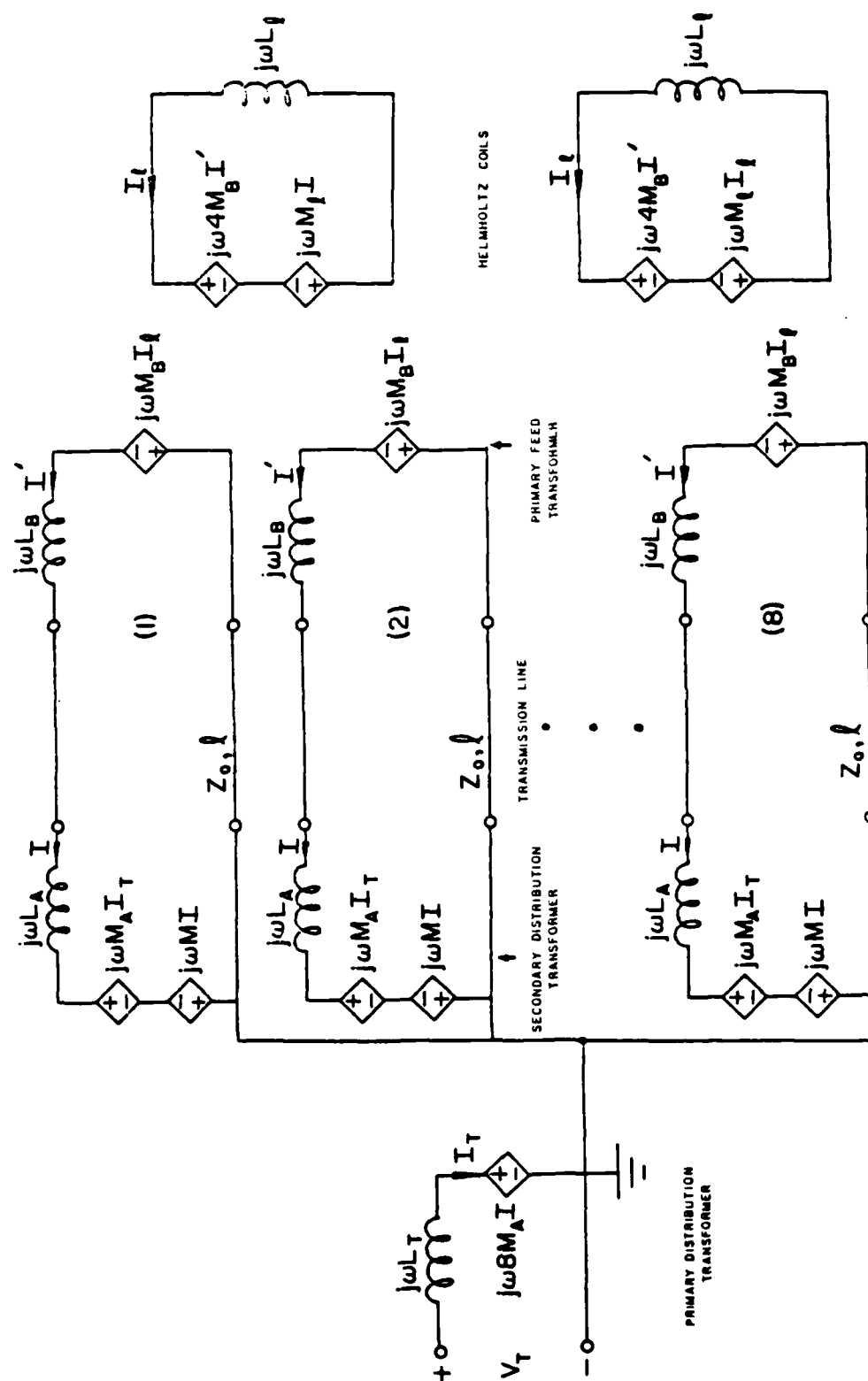


Fig. D.1: Helmholtz coil and driver equivalent circuit.

$L_\ell$  = inductance of Helmholtz coil

$M_\ell$  = mutual inductance of Helmholtz coil

$V_T$  = input voltage

$I_\ell$  = current in one Helmholtz coil

We wish to derive a transfer function which relates the input voltage  $V_T$  to the output current  $I_\ell$ . The dependent variables are the coaxial cable length and the frequency of operation. The analysis is done in the frequency domain with assumed  $\exp(j\omega t)$  time convention.

We begin by analyzing one of our eight secondary distribution subsystems, as shown in Fig. D.2.

$$V_1(x) = \frac{V_G \frac{Z_0}{Z_0 + Z_g}}{1 - \Gamma_g \Gamma_\ell e^{-j2\beta\ell}} \left[ e^{-j\beta x} + \Gamma_\ell e^{-j2\beta\ell} e^{j\beta x} \right] \quad (D.1)$$

where

$$\Gamma_\ell = \frac{Z_L - Z_0}{Z_L + Z_0}, \quad \Gamma_g = \frac{Z_g - Z_0}{Z_g + Z_0}$$

The other case we have is that of Figure D.3, essentially the mirror image.

Replacing  $x$  with  $(\ell - x)$  we then have

$$V_2(x) = \frac{V_L \frac{Z_0}{Z_0 + Z_L}}{1 - \Gamma_g \Gamma_\ell e^{-j2\beta\ell}} e^{-j\beta\ell} \left[ e^{j\beta x} + \Gamma_g e^{-j\beta x} \right] \quad (D.2)$$

The resultant superposition of these two solutions (Fig. D4) is our desired result:

$$V(x) = \frac{V_g \frac{Z_0 e^{-j\beta\ell}}{Z_0 + Z_L} \left[ e^{j\beta x} + \Gamma_0 e^{-j\beta x} \right] + V_L \frac{Z_0}{Z_0 + Z_L} \left[ e^{-j\beta x} + \Gamma_g e^{-j2\beta\ell} e^{j\beta x} \right]}{1 - \Gamma_g \Gamma_0 e^{-j2\beta\ell}} \quad (D.3)$$

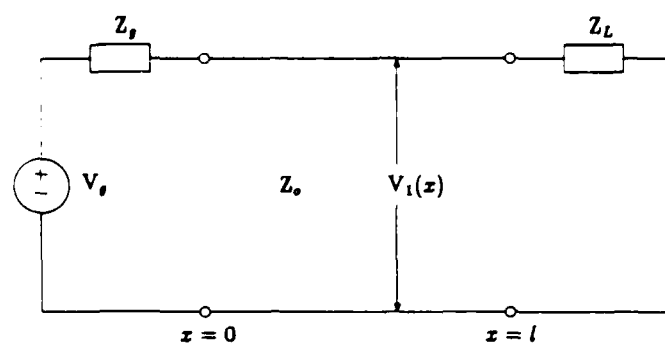


Fig. D.2: Secondary distribution circuit (source left).

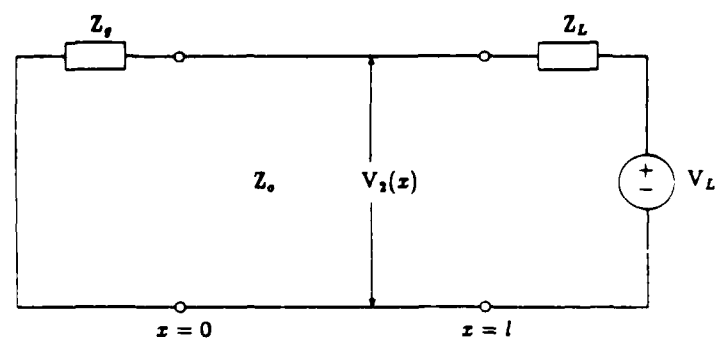


Fig. D.3: Secondary distribution circuit (source right).

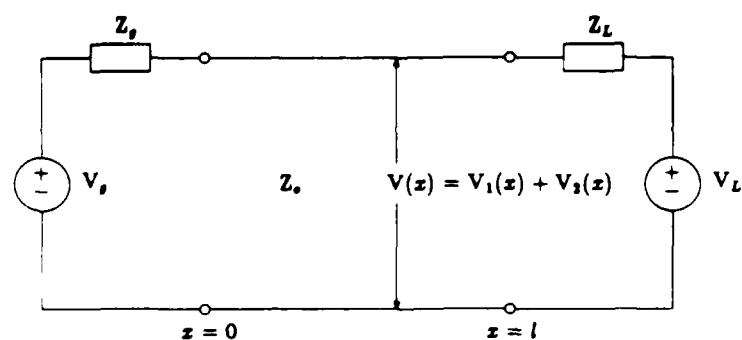


Fig. D.4: Resultant circuit.



where

$$V_g = j\omega M_A I_T - j\omega M I$$

$$V_L = -j\omega M_B I_\lambda$$

$$Z_g = j\omega L_A$$

$$Z_L = j\omega L_B$$

The system of equations describing our whole circuit is then:

$$\begin{aligned} 1) \quad & V_g - V(\lambda) + sL_A I = 0 \\ 2) \quad & V(0) + V_L + sL_B I' = 0 \\ 3) \quad & s4M_B I' - sM_\lambda I_\lambda + sL_\lambda I_\lambda = 0 \\ 4) \quad & sL_T I_T + s8M_A I - V_T = 0 \end{aligned} \quad (D.4)$$

The voltages, which are a function of the coaxial cable length, can be conveniently written as:

$$V(0) = AI_T + BI + CI_\lambda \quad (D.5)$$

where

$$A = \frac{sM_A Z_0 e^{-j\beta\lambda} (1 + \Gamma_0)}{(Z_0 + Z_g) (1 - \Gamma_g \Gamma_0 e^{-j2\beta\lambda})}$$

$$B = \frac{-sMZ_0 e^{-j\beta\lambda} (1 + \Gamma_0)}{(Z_0 + Z_g) (1 - \Gamma_g \Gamma_0 e^{-j2\beta\lambda})}$$

$$C = \frac{sM_B Z_0 (1 + \Gamma_g e^{-j2\beta\lambda})}{(Z_0 + Z_L) (1 - \Gamma_g \Gamma_0 e^{-j2\beta\lambda})} ,$$

and

$$V(\ell) = DI_T + EI + FI_2 \quad (D.6)$$

where

$$D = \frac{sM_A Z_0 (1 + \Gamma_0 e^{-j2\beta\ell})}{(Z_0 + Z_g) (1 - \Gamma_g \Gamma_0 e^{-j2\beta\ell})}$$

$$E = \frac{-sMZ_0 (1 + \Gamma_0 e^{-j2\beta\ell})}{(Z_0 + Z_g) (1 - \Gamma_g \Gamma_0 e^{-j2\beta\ell})}$$

$$F = \frac{sM_B Z_0 e^{-j\beta\ell} (1 + \Gamma_g)}{(Z_0 + Z_L) (1 - \Gamma_g \Gamma_0 e^{-j2\beta\ell})}$$

The simultaneous solution of these equations yields our desired transfer function:

$$I_2 = \frac{\frac{V_T}{sL_T} \{sBM_A - BD - sAL_A + sAM + AE\}}{\left[ \frac{8M_A D}{L_T} - \frac{s8M_A^2}{L_T} + sL_A - sM - E \right] \left[ \frac{sL_B (M_\ell - L_\ell)}{4M_B} + sM_B + C \right] + F(B - \frac{A8M_A}{L_T})} \quad (D.7)$$

## D.2 Results

This transfer function was programmed and plots were made for given frequencies and coaxial cable lengths. Values for the assorted self and mutual inductances were either measured or calculated (where measurements were deemed impractical). They are:

$$L_A = 4.5 \times 10^{-7} \text{ H}$$

$$M_A = 7 \times 10^{-7} \text{ H}$$

$$M = 4.2 \times 10^{-7} \text{ H}$$

$$L_B = 43 \times 10^{-6} \text{ H}$$

$$M_z = 2.8 \times 10^{-7} \text{ H (calculated)}$$

$$L_z = 4.6 \times 10^{-6} \text{ H (calculated)}$$

$$L_T = 6.6 \times 10^{-6} \text{ H}$$

$$M_B = 5.8 \times 10^{-6} \text{ H}$$

The computer program listing follows, along with a computed response (Fig. D.5) for a 14-foot long feed cable. The measured data are given in Figs. D.6 and D.7 for 18 ft. and 14.3 ft. feed cables, respectively. For unexplained reasons the 18-foot cable length data matches the theory better than the 14-foot cable length data, and at this time we do not have an explanation for the discrepancy.

### D.3 Listing of the Program

```

1      REAL MIL,LEN,LB,LL,LA,LT,L
2      REAL MA,M,ML,MB
3      COMPLEX GAMG,GAMGO,X,DEN,OMEG,A,B,C,U,E,F
4      COMPLEX T1,T2,T3,T4,T5,IL
5      COMPLEX Z,ZZ,CMLX
6      COMPLEX NUM,DENOM
7      LA=4.5E-7
8      MA=7.0E-7
9      M=4.2E-7
10     LB=43.E-6
11     ML=2.8E-7
12     LL=4.6E-6
13     LT=6.6E-6
14     MB=5.8E-6
15     PI=3.14159
16     WRITE(6,50)
17     READ(5,20) FREQ,LEN,VT
18     Y=2*PI*FREQ
19     OMEG=CMPLX(0.0,Y)
20     BETA=2*PI*FREQ/(0.666*3.0E8)
21     L=LEN*0.304
22     X=OMEG*LA
23     GAMG=(X-50.)/(X+50.)
24     X=OMEG*LB
25     GAMO=(X-50.)/(X+50.)
26     U=COS(BETA*L)
27     V=SIN(-BETA*L)
28     UU=COS(2*BETA*L)
29     VV=SIN(-2*BETA*L)
30     Z=CMPLX(U,V)
31     ZZ=CMPLX(UU,VV)
32     DEN=1.0-GAMG*GAMO*ZZ
33     X=50.*(1.0+GAMO)*Z/(50.+OMEG*LA)
34     A=OMEG*MA*X/DEN
35     B=OMEG*M*X/DEN
36     X=50.*(1.0+GAMG*ZZ)/(50.+OMEG*LB)
37     C=OMEG*MB*X/DEN
38     X=50.*(1.0+ZZ*GAMO)/(50.+OMEG*LA)
39     D=OMEG*MA*X/DEN
40     E=OMEG*M*X/DEN
41     X=50.*Z*(1.0+GAMG)/(50.+OMEG*LB)
42     F=OMEG*MB*X/DEN
43     T1=OMEG*B*MA
44     T2=B*D
45     T3=OMEG*A*LA
46     T4=OMEG*A*M
47     T5=A*E
48     NUM=VT*(T1-T2-T3+T4+T5)/(OMEG*LT)
49     T1=OMEG*LB*(ML-LL)/(4.0*MB)+OMEG*MB+C
50     T2=(-OMEG*B.*MA*MA/LT+B.*MA*D/LT-OMEG*M+OMEG*LA-E)
51     T3=(B-B.0*A*MA/LT)*F
52     DENOM=T1*T2+T3
53
54     IL=NUM/DENOM
55     MIL=CABS(IL)*1000
56     ANGIL=ATAN2(AIMAG(IL),REAL(IL))*180/PI
57     PRINT 100,MIL
58     PRINT 200,ANGIL
59     PRINT 300,LEN
60     PRINT 400,FREQ
61     PRINT 500,VT
62     20    FORMAT(3G9.1)
63     50    FORMAT(' ENTER FREQUENCY IN HZ,LENGTH IN FT,VOLTAGE')
64     100   FORMAT(' COIL CURRENT=',F7.2,' MILLIAMPS')
65     200   FORMAT(' PHASE=',F6.1,' DEGREES')
66     300   FORMAT(' COAXIAL CABLE LENGTH=',F7.2,' FT')
67     400   FORMAT(' FREQUENCY=',F11.1,' Z')
68     500   FORMAT(' INPUT VOLTAGE=',F6.1,' VOLTS')
69     STOP
70     END

```

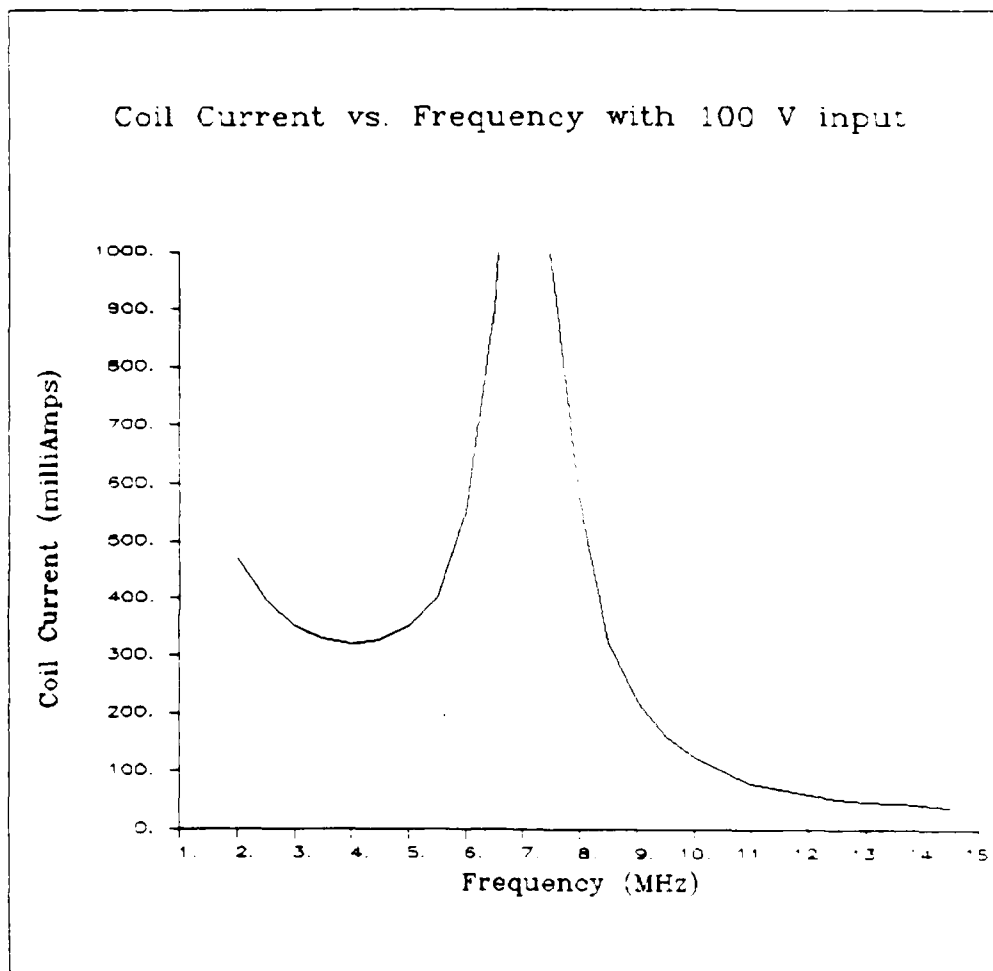


Fig. D.5: Computed coil current for a 14-foot cable length.

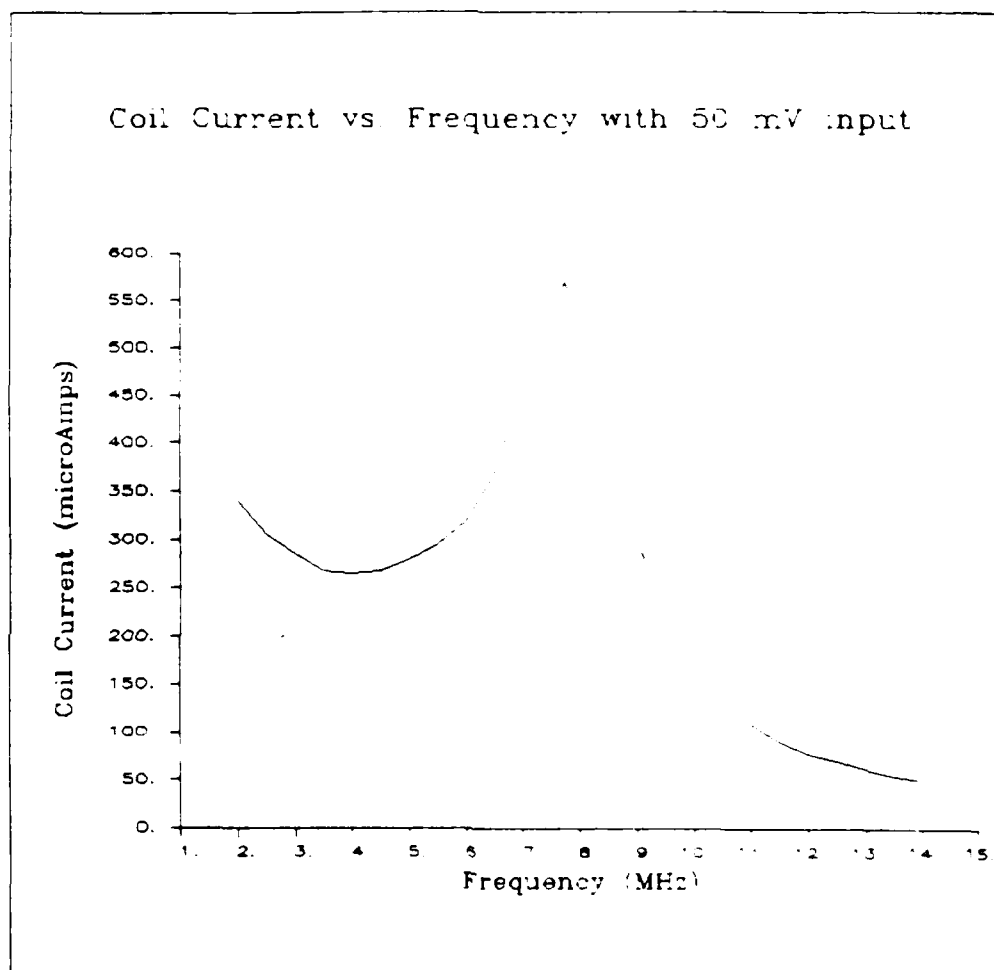


Fig. D.6: Measured coil current for the 18-foot long cable.

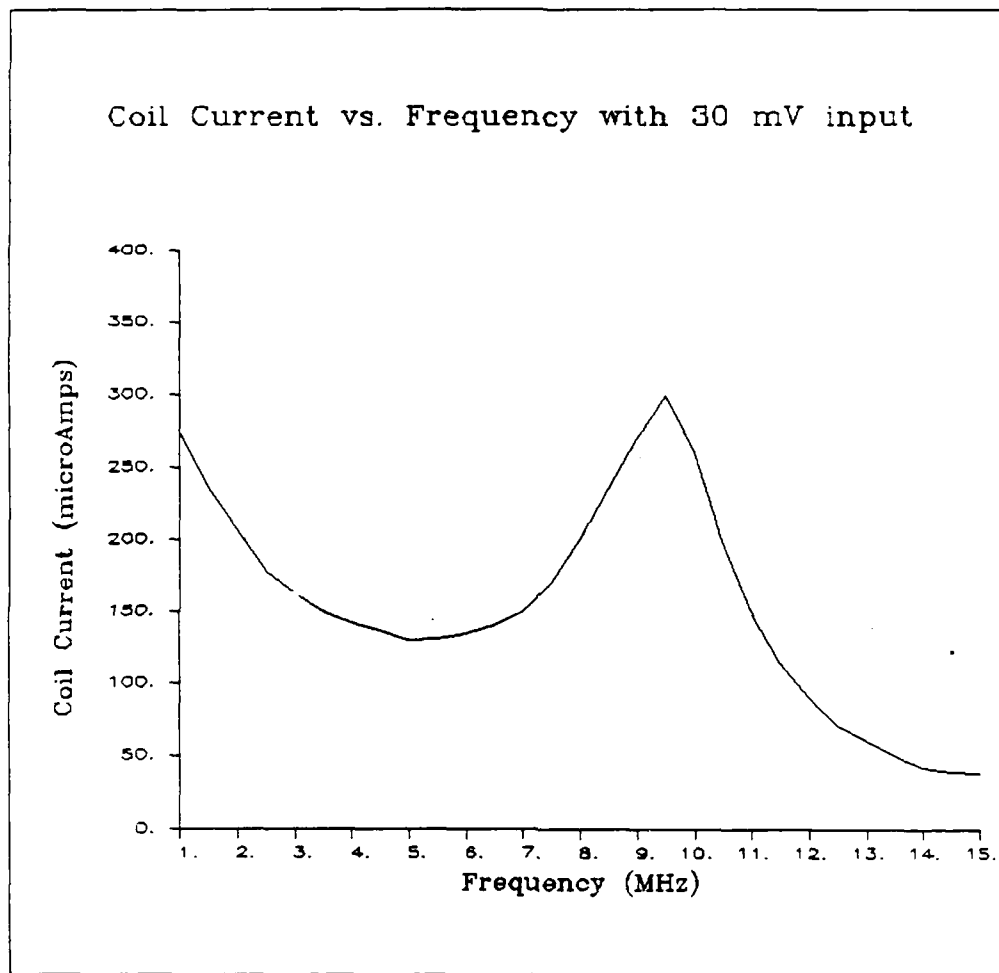


Fig. D.7: Measured coil current for the 14.3-foot long cable.

APPENDIX E  
INDUCTANCE OF A LOOP

A single turn loop was constructed to confirm the theoretical value of inductance calculated from the formula [E.1]

$$L = \frac{a}{100} [7.353 \log_{10} (\frac{16a}{d}) - 6.386] \quad (E.1)$$

where  $a$  is the loop radius and  $d$  is the wire diameter. With the values  $a = 24$  in. and  $d = 0.125$  in. we have  $L = 4.62 \mu\text{H}$ .

To test this result, a four-foot diameter loop was constructed using RG-58/U coax mounted on a styrofoam sheet as shown below.

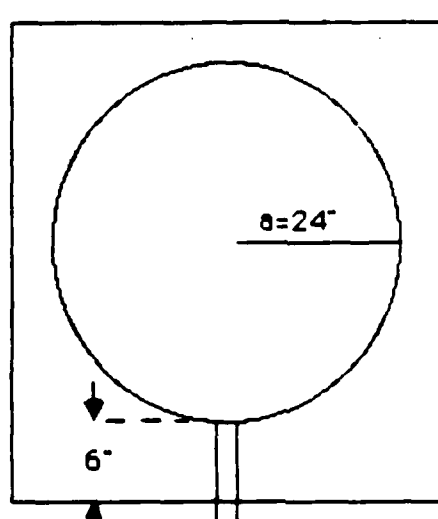


Fig. E.1: Loop geometry.

Measurements were made using a Boonton Radio Corp. Q-meter, Type 260-A, and from the readings we determined the  $Q$  and the resonant capacitance  $C$  in the frequency range 3.5 to 10.0 MHz. Inductance was found from the



equation  $\omega = 1/\sqrt{LC}$ , and the series and parallel resistances were calculated for the equivalent parallel and series circuits shown in Fig. E2.

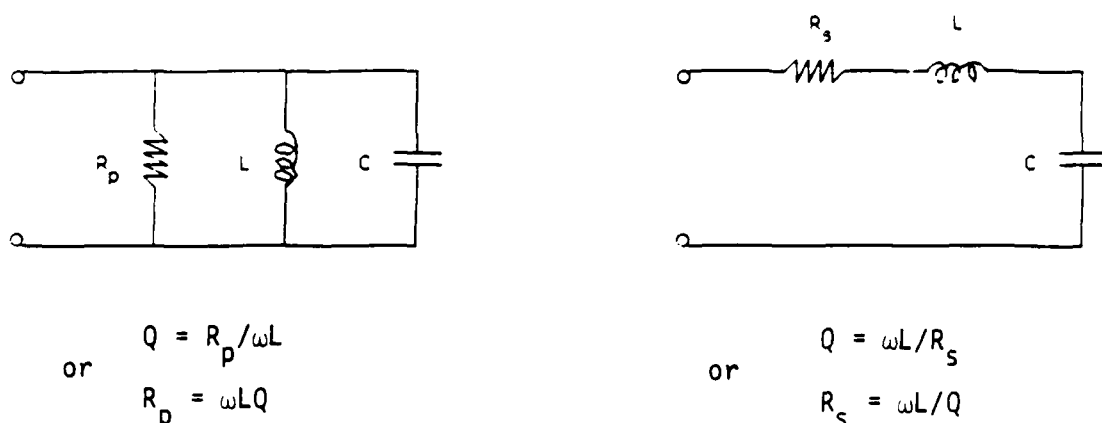


Fig. E.2: Equivalent circuits.

Table E1 below lists the computed equivalent components.

Table E1. Measured Loop Parameters.

$f(\text{MHz})$	$Q$	$C \text{ (pF)}$	$L \text{ (}\mu\text{H)}$	$R_s \text{ (}\Omega\text{)}$	$R_p \text{ (k}\Omega\text{)}$
3.5	140	424	4.88	0.767	15.0
5.0	108	198	5.12	1.49	17.4
6.5	98	110	5.45	2.27	21.8
7.9	60	68	5.97	4.94	17.8
10.0	18	33	7.68	26.8	8.69

Note that as the frequency decreases,  $L$  approaches the  $4.62 \mu\text{H}$  value computed from (E.1).

#### Reference

[E.1] Reference Data for Radio Engineers, International Telephone and Telegraph Corporation (4th Ed.), 1956; p. 133.

END

4-87

DTIC